2015-09

Proton irradiation-induced metal voids in gallium nitride high electron mobility transistors

Wade, Michael G.

Monterey, California: Naval Postgraduate School

NAVAL POSTGRADUATE SCHOOL

MONTEREY, CALIFORNIA

THESIS

PROTON IRRADIATION-INDUCED METAL VOIDS IN GALLIUM NITRIDE HIGH ELECTRON MOBILITY TRANSISTORS

by

Michael G. Wade

September 2015

Thesis Advisor: Todd Weatherford
Co-Advisor: Petra Specht

Approved for public release; distribution is unlimited

THIS PAGE INTENTIONALLY LEFT BLANK

REPORT DOCUMENTATION PAGE

Form Approved OMB No. 0704-0188

1. AGENCY USE ONLY *(Leave blank)*	**2. REPORT DATE** September 2015	**3. REPORT TYPE AND DATES COVERED** Master's Thesis

4. TITLE AND SUBTITLE
PROTON IRRADIATION-INDUCED METAL VOIDS IN GALLIUM NITRIDE HIGH ELECTRON MOBILITY TRANSISTORS

5. FUNDING NUMBERS
HDTRA1412411

6. AUTHOR(S) Wade, Michael G.

7. PERFORMING ORGANIZATION NAME(S) AND ADDRESS(ES)
Naval Postgraduate School
Monterey, CA 93943-5000

8. PERFORMING ORGANIZATION REPORT NUMBER

9. SPONSORING /MONITORING AGENCY NAME(S) AND ADDRESS(ES)
Defense Threat Reduction Agency (DTRA)
Fort Belvoir, Virginia 22060

10. SPONSORING/MONITORING AGENCY REPORT NUMBER
N/A

11. SUPPLEMENTARY NOTES The views expressed in this thesis are those of the author and do not reflect the official policy or position of the Department of Defense or the U.S. Government. IRB Protocol number ____N/A____.

12a. DISTRIBUTION/AVAILABILITY STATEMENT
Approved for public release; distribution is unlimited

12b. DISTRIBUTION CODE
A

13. ABSTRACT (maximum 200 words)

Gallium nitride/aluminum gallium nitride high electron mobility transistors with nickel/gold (Ni/Au) and platinum/gold (Pt/Au) gating are irradiated with 2 MeV protons. Destructive physical analysis revealed material voids underneath the gate finger of the device. These voids, which are not found in fresh devices, cause a decrease in effective gate contact area, ultimately degrading the device performance and reliability. Scanning transmission electron microscopy images and respective line scans of the gate-foot area-of-concern confirm that voids were present. The gate-finger's silicon nitride passivation layer and Au metallization layer were removed via focused ion beam stripping in order to analyze the gate electrode Ni or Pt layers for defects. Scanning electron microscopy images revealed voids along the gate finger edge and circular voids in the gate finger's length that contribute to the device's reduction in parameter performance. The current hypothesis is that the Ni or Pt voiding is a result of the Kirkendall effect. The effect is seen in the energy dispersive spectroscopy analysis, where Ni has migrated into the Au layer. A model was developed to predict void sizes versus dose and validated using data on dislocation density.

14. SUBJECT TERMS
radiation, Kirkendall effect, high electron mobility transistor, electron microscopy

15. NUMBER OF PAGES
109

16. PRICE CODE

17. SECURITY CLASSIFICATION OF REPORT	**18. SECURITY CLASSIFICATION OF THIS PAGE**	**19. SECURITY CLASSIFICATION OF ABSTRACT**	**20. LIMITATION OF ABSTRACT**
Unclassified	Unclassified	Unclassified	UU

NSN 7540-01-280-5500

Standard Form 298 (Rev. 2-89)
Prescribed by ANSI Std. 239-18

THIS PAGE INTENTIONALLY LEFT BLANK

Approved for public release; distribution is unlimited

PROTON IRRADIATION-INDUCED METAL VOIDS IN GALLIUM NITRIDE HIGH ELECTRON MOBILITY TRANSISTORS

Michael G. Wade
Captain, United States Marine Corps
B.S.E., Miami University, 2007
M.S.M.E., University of South Carolina, 2009

Submitted in partial fulfillment of the
requirements for the degree of

MASTER OF SCIENCE IN ELECTRICAL ENGINEERING

from the

NAVAL POSTGRADUATE SCHOOL
September 2015

Author: Michael G. Wade

Approved by: Dr. Todd Weatherford
Thesis Advisor

Dr. Petra Specht
Co-Advisor

Dr. Clark Robertson
Chair, Department of Electrical Engineering

THIS PAGE INTENTIONALLY LEFT BLANK

ABSTRACT

Gallium nitride/aluminum gallium nitride high electron mobility transistors with nickel/gold (Ni/Au) and platinum/gold (Pt/Au) gating are irradiated with 2 MeV protons. Destructive physical analysis revealed material voids underneath the gate finger of the device. These voids, which are not found in fresh devices, cause a decrease in effective gate contact area, ultimately degrading the device performance and reliability. Scanning transmission electron microscopy images and respective line scans of the gate-foot area-of-concern confirm that voids were present. The gate-finger's silicon nitride passivation layer and Au metallization layer were removed via focused ion beam stripping in order to analyze the gate electrode Ni or Pt layers for defects. Scanning electron microscopy images revealed voids along the gate finger edge and circular voids in the gate finger's length that contribute to the device's reduction in parameter performance. The current hypothesis is that the Ni or Pt voiding is a result of the Kirkendall effect. The effect is seen in the energy dispersive spectroscopy analysis, where Ni has migrated into the Au layer. A model was developed to predict void sizes versus dose and validated using data on dislocation density.

THIS PAGE INTENTIONALLY LEFT BLANK

TABLE OF CONTENTS

I. INTRODUCTION 1
A. RELEVANCE TO THE DEPARTMENT OF DEFENSE 1
B. RESEARCH OBJECTIVE 2
C. RELATED WORK 3
D. THESIS ORGANIZATION 3

II. BACKGROUND 5
A. FUNDAMENTALS OF GALLIUM NITRIDE HEMT PHYSICS 5
1. GaN 5
2. III-Nitride Growth and Device Fabrication 6
3. GaN HEMT Physics 8
4. Proton Radiation Effects 11
B. NAVAL RESEARCH LABORATORY GALLIUM NITRIDE HEMT RETICLE 13
1. Unstressed Device Characteristics 15
2. Electrically Stressed Device Parameters 16
3. Proton Irradiated Testing 17
C. MICROSCOPY 20
1. SEM 20
2. FIB 22
3. TEM 23
4. STEM 24
5. EDS 24

III. SAMPLE PREPARATION 27
A. LOCATIONS AND MACHINES UTILIZED 27
B. FOCUSED ION BEAM MILLING AND LIFT OUT 27
1. Initial Setup 27
2. Sample Protection 30
3. Ion Cutting 31
4. Lift Out 32
5. Mounting 33
C. NANO ION MILL 34
D. PLASMA CLEANER 35
E. SAMPLE AND COMPARISON TO PREVIOUS WORK 35
F. GATE FINGER STRIPPING 35
1. LBNL Strip Depth 35
2. NPS SEM Trials 36

IV. RESULTS 41
A. VOID DISCOVERY 41
B. ANALYSIS OF THE 2DEG INTERFACE 42
C. SEM INVESTIGATION OF NICKEL DEVICES 44
1. Fresh Devices 44

2. Proton Irradiated 47
D. PLATINUM DEVICES 50
1. Characteristics 50
2. Fresh Devices 51
3. Irradiated Devices 53
E. VARYING RADIATION FLUENCE DEVICES 56
F. COMPARISON AND VOID RELEVANCE 59
1. Fresh versus Irradiated Ni/Au 59
2. Ni versus Pt Comparison and Gate Length Assessment 64
3. Radiation-fluence Effects 65
G. DISLOCATION ANALYSIS 66
H. VACANCY AND DIFFUSION MODEL 68
1. Theory 68
2. Model Assumptions 69
3. Threading-Dislocation Radius of Vacancy Interaction 69
4. Geometric Volume Comparison 71
I. MATERIAL CALCULATIONS FOR DIFFUSION MODEL IMPROVING THE EPILAYER 73
J. SUMMARY OF DEFECTS IDENTIFIED, CAUSES, SOLUTIONS 74
V. CONCLUSIONS AND FUTURE WORK 75
A. CONCLUSIONS 75
B. FUTURE WORK 76
APPENDIX. MATLAB CODE 79
LIST OF REFERENCES 85
INITIAL DISTRIBUTION LIST 89

LIST OF FIGURES

Figure 1. Burgers vector *b* and line axis *t* characterize two types of dislocations from MIT OpenCourseWare, from [19]. 8
Figure 2. Polarizations caused by spontaneous and piezoelectric strain at the 2DEG interface, after [20]. 9
Figure 3. GaN HEMT structure with band diagram explaining formation of 2DEG, from [22]. 11
Figure 4. Displacement-damage due to radiation results in a Frenkel pair, vacancy and interstitial atom. 12
Figure 5. GaN HEMT structure, after [28]. 14
Figure 6. Step drain voltage stress testing of drain and gate current before and after irradiation where current collapse occurs, from [4]. 16
Figure 7. NRL parameter changes with increased proton irradiation dose, from [4]. 18
Figure 8. Proton irradiation decreases the drain current versus V_{gs} at two different drain to source voltages, after [4]. 19
Figure 9. Proton irradiation decreases drain current versus at three different voltages of 1,0, and –1 V, from [4]. 19
Figure 10. Increased proton irradiation increases $R_{on,dyn}$, from [4]. 20
Figure 11. SEM illustration of internal components, from [31]. 21
Figure 12. SEM and FIB orientation inside microscope, from [32]. 22
Figure 13. TEM illustration showing physical location of sample, imaging plane, EDS, and EELS, from [33]. 23
Figure 14. STEM image using EDS for elemental mapping, after [5]. 25
Figure 15. Example of an EDS line scan, from [5]. 26
Figure 16. SEM Specimen Stub Pedestal on Holder. 28
Figure 17. NRL chip mounted to SEM pedestal with carbon fiber tape along with STEM copper port. 28
Figure 18. NRL chip SEM overview consists of various devices with HEMTs located in the first quadrant. 29
Figure 19. GaN HEMT device depicting the drain, source, and gate. 29
Figure 20. GaN HEMT gate finger with protective Pt deposition, from [5]. 30
Figure 21. GaN HEMT device with gate finger stripped of Si_3N_4 and Au via FIB. 31
Figure 22. FIB trenches cut into gate finger with "L" undercut to remove lamella for TEM. 32
Figure 23. Lamella Pt welded to Omni Probe for lift out. 32
Figure 24. Lamella welded to TEM copper port. 33
Figure 25. Ion NanoMill used for thinning lamella for STEM, from [5]. 34
Figure 26. Lamella prepared for STEM analysis showing staircase FIB stripping. 36
Figure 27. Tip of Ni/Au gate finger stripped to identify depth of Ni measured 360 nm. 37
Figure 28. STEM analysis showing Ni layer at approximately 360.0 nm. 38
Figure 29. EDS depth trials of Au removed (blue) and Ni remaining (red). 39

Figure 30. STEM images and EDS line scans of fresh device (a, b) compared to proton irradiated device (c, d) with Ni voiding, from [27]. 41
Figure 31. STEM images of AlGaN/GaN interfaces taken at ERC, Juelich, Germany, courtesy of M. Luysberg, P.Specht. 42
Figure 32. AlGaN/GaN interface with HRTEM from ERC, Germany, courtesy of M. Luysberg, P. Specht. 43
Figure 33. HR EDS line scans at 2DEG interface, data taken at ERC, Germany, courtesy of M. Luysberg, P. Specht. 43
Figure 34. A Ni/Au gated GaN HEMT stripped in two locations of the gate finger reveals that Ni is present and without void degradation. 45
Figure 35. Fresh sample near the root of the gate finger displays no voiding. 45
Figure 36. The first fresh Ni/Au gated device to display edge voiding. 46
Figure 37. Types of Ni voiding found below the Si_3N_4 and Au layers. 47
Figure 38. FIB stripped gate finger reveals edge and circular Ni voiding. 48
Figure 39. HEMT gate finger root is FIB stripped revealing Ni void issue at the boundary where AlGaN/GaN does not cover left side. 49
Figure 40. FIB stripping reveals a Ni void at the boundary of Si_3N_4 layering. 49
Figure 41. Pt/Au gated HEMT before and after proton irradiation decreases drain current versus drain voltage. 50
Figure 42. Pt/Au gated HEMT before and after proton irradiation decreases drain current versus gate voltage. 51
Figure 43. E-beam image of fresh Pt/Au HEMT displays no voiding. 52
Figure 44. Pt/Au gated device with closer drain-to-gate finger layout is FIB stripped to reveal no voiding near the root. 52
Figure 45. FIB stripped Pt/Au gated sample. 53
Figure 46. I-beam image of FIB stripped Pt/Au gated HEMT reveals large circular mid-finger voids. 54
Figure 47. FIB stripped Pt/Au gated HEMT displays a line of circular voids. 54
Figure 48. FIB stripped Pt/Au gated HEMT with 3.0 nm gate finger length reveals mid-finger circular voids. 55
Figure 49. Pt/Au gated HEMT has unusual, residual Au. 56
Figure 50. Ten seconds into I-mode, the charge builds up and prevents accurately using FIB due to visibility. 57
Figure 51. E-mode view of sample after I-mode charge build up confirms that this was a charge build-up and that no ion damage occurred. 57
Figure 52. Lower fluence of edge and one small mid-finger void starting. 58
Figure 53. Fresh versus irradiated gate of electrode with Ni void, from [27]. 59
Figure 54. ImageJ software utilized to convert an SEM image to 8-bit-black-and-white and then calculate area of voiding. 60
Figure 55. C-V characteristics of multiple NRL Ni/Au Schottky gated HEMTs before and after irradiation, from [4]. 61
Figure 56. C-V characteristics for the average of 20 GaN HEMT devices before and after proton irradiation. 62
Figure 57. Additional surface material seen before stripping turns out to be the center of the largest Ni void. 63

Figure 58. Proton radiation fluence versus void volume. 65
Figure 59. Conventional TEM performed at different tilt angles (excitation), courtesy of P. Specht. 66
Figure 60. Conventional TEM image of same location at two different tilt angles: left - [0002] excitation / right - [1100] excitation, courtesy of P. Specht. 68
Figure 61. Proton NIEL curves for HEMT materials. 71
Figure 62. Schematic of a threading dislocation attracting vacancies forming a highway for Ni atom diffusion uniformly into Au layer causing void. 72
Figure 63. NRL's new epilayer sample. 73

THIS PAGE INTENTIONALLY LEFT BLANK

LIST OF TABLES

Table 1. Semiconductor material properties, after [9]. 5
Table 2. Material lattice mismatch comparison to GaN, after [15]. 7
Table 3. NRL epilayer materials and thickness ascending from bottom to top of wafer. 15
Table 4. Device characterization for NRL GaN HEMTs, from [4]. 15
Table 5. NRL electrical stressed device identification and levels, from [5] 16
Table 6. NRL proton testing parameters, from [4]. 17
Table 7. Pt/Au gated NRL device parameters. 50
Table 8. Void area comparison. 64
Table 9. Summary of Defects 74

THIS PAGE INTENTIONALLY LEFT BLANK

LIST OF ACRONYMS AND ABBREVIATIONS

2DEG	two-dimensional electron gas
AlGaN	aluminum gallium nitride
AlOx	aluminum oxide
CCD	charged coupled device
CTE	coefficient of thermal expansion
DOD	Department of Defense
DTRA	Defense Threat Reduction Agency
E-beam	electronic beam
EDS	energy-dispersive x-ray spectroscopy
EL	electroluminescence
Epi	epitaxial layers
ERC	Ernst Ruska Center
FET	field effect transistor
FIB	focused ion beam
GaN	gallium nitride
HAADF	high-angle annular dark-field
HEMT	high electron mobility transistor
I-beam	ion beam
IC	integrated circuit
LBNL	Lawrence Berkeley National Laboratory
MeV	mega electron-volt
NCEM	National Center for Electron Microscopy
NIEL	non-ionizing energy loss
NPS	Naval Postgraduate School
NRL	Naval Research Laboratory
PKA	primary knock-on atom
Si_3N_4	silicon nitride
UCB	University of California, Berkeley
WBDF	weak beam dark-field

THIS PAGE INTENTIONALLY LEFT BLANK

ACKNOWLEDGMENTS

I would like to thank Petra Specht for her invaluable time and knowledge on the subjects of microscopy and material science that were shared over the past two years at Lawrence Berkeley National Laboratory. The training and education that I received on the equipment at Berkeley was instrumental to the successes of this research. Her mentorship and impromptu topic lectures continually enhanced my motivation and understanding throughout the research process while ultimately enriching my overall thesis experience.

I would also like to thank Todd Weatherford for the superior project management of this research and for his contributions toward my overall knowledge of electrical engineering. His expert teachings on electronic devices, their internal composition and functionality, and device reliability have given me a very specific area of concentration to pursue after my military career.

Lastly, I would like to thank Matthew Porter for his continuous drive and passion for research, which is contagious in nature. His knowledge and ability to explain electronic device physics is beyond compare, and I truly value his contributions toward my education and this thesis.

THIS PAGE INTENTIONALLY LEFT BLANK

I. INTRODUCTION

Heteroepitaxial gallium nitride (GaN) high-electron mobility transistors (HEMTs) are proving to be one of the top wide bandgap technologies for the future of microwave and solid state electronics. This is due to the III-Nitride material family's high thermal conductance and critical electric field avalanche breakdown, which leads to devices with high-power density and high efficiency. These qualities make such devices prime candidates for use as high-power amplifiers in navigation and communication applications [1].

While the attributes of GaN HEMTs are promising, they are grown on Si or SiC substrates in heteroepitaxial layers, which results in misfit and threading dislocations due to strain from lattice mismatch between the epitaxial layer and the substrate. These phenomena can lead to carrier trapping due to trap states introduced by dislocations and impurities that diffuse along the line defects. Trapping reduces the performance of GaN devices, raising reliability concerns for GaN HEMT devices grown in this way [2], thus, it is necessary to research the underlying causes of these degrading mechanisms in order to fully understand and remedy them.

Another significant quality of GaN is the ability to withstand radiation damage, which greatly increases the importance of GaN devices to the electronics industry and Department of Defense (DoD). The effects of radiation upon the device degradation and performance must also be studied in order to appropriately understand and utilize these transistors.

A. RELEVANCE TO THE DEPARTMENT OF DEFENSE

Military applications of GaN devices include pulsed radars, counter-IED jammers, community antenna television (CATV) modules, which distribute incoming RF signals to multiple locations on coaxial cable, and fourth-generation wireless infrastructure base-stations [1]. Military use of GaN devices can improve the efficiency and reduce the size and weight in protection, location, and command, control, communications, computers, and intelligence (C4I) applications. The promising qualities

of GaN devices in applications such as microwave transmitters for communications and RADAR as described in [3] are important to the DOD. Such applications can be utilized on naval vessels to replace vacuum tubes, which are used for high-power RF requirements.

This thesis research was funded by the Defense Threat Reduction Agency (DTRA) due to the radiation-hard quality of GaN and its ability to function in military applications, which may be exposed to high radiation environments. A contribution to the radiation effects of the GaN HEMT being researched by the Naval Research Laboratory (NRL) under the DTRA funding is provided by this thesis.

B. RESEARCH OBJECTIVE

The focus of this work is to study the physical processes underlying damage induced by high-energy proton irradiation of GaN-on-Si HEMTs. Scanning electron microscopy (SEM) and focused ion beam (FIB) milling, along with scanning transmission electron microscopy (STEM) and x-ray energy dispersive spectroscopy (EDS), are used for a destructive physical analysis of irradiated devices. Past work [4] identified a significant type of defect, which appears as voiding found in Ni metallization irradiated devices' gate fingers. In this thesis work, fresh Ni/Au gated devices are compared to devices irradiated at varying dose levels. Devices on a different epilayer sample are also explored. An accumulation and compilation of defect size and location data is conducted in order to create a statistical model of device damage. For this analysis, defect geometries are quantified within the underlying gate material via SEM/EDS imaging using post processing tools. Transmission electron microscopy (TEM) weak beam analysis is conducted for some areas under the gate to determine the type of dislocations that are present. Analysis of dislocations gives insight into the nature of these dislocations and may lead to a better understanding of which line defects may be detrimental to the stability of the HEMT due to enhanced diffusion along the dislocation line, an effect known as pipe diffusion [4]. A model is developed to predict the void size versus radiation dose. Proposals of defect remedies are provided in order to minimize, and in the optimal case eliminate, the voids to increase the reliability of these devices.

C. RELATED WORK

Preparation techniques of the NRL fabricated GaN HEMTs used in this thesis were explored in [5] by NPS student A. Wessel at Lawrence Berkeley National Laboratory (LBNL). In that work, lamellas were removed via FIB trenching and then platinum welded to copper ports for further thinning in an ion NanoMill for analysis via STEM. Wessel's work provided a streamlined process for the sample preparation procedure that optimized the yield of successful samples available for analysis. In this thesis, those methods are expanded and a novel approach for the use of the FIB to strip Ni/Au gates for analysis is introduced.

GaN point defects have been investigated directly where the buffer layers and GaN layer under the gate were explored after a chemical etching process was utilized to remove the metallization of Au and Ni [6]. Many others have researched the effects of defects in the GaN layer by exploring trapping defects in the buffer and GaN layers, as shown in [7]. Previous work carried out at NRL investigated the changes in electrical performance of the devices after varying forms of stress, including electrical, gamma radiation and proton irradiation [4]. The devices exposed to proton irradiation are examined in this work.

D. THESIS ORGANIZATION

This thesis is laid out as follows. The basic physics of operation and the fabrication process of GaN HEMTs are examined in Chapter II. In Chapter III, microscopy and the equipment associated with this study (such as SEM, STEM, TEM, EDS) are explained in depth. The results of experimental procedures are discussed in Chapter IV, and conclusions are presented, along with future work, in Chapter V.

THIS PAGE INTENTIONALLY LEFT BLANK

II. BACKGROUND

A. FUNDAMENTALS OF GALLIUM NITRIDE HEMT PHYSICS

In order to understand the work presented in this thesis better, a foundation is provided that covers topics in material science and physics. It is important to appreciate the different materials utilized in electronic devices and their respective characteristics. This knowledge, coupled with the operational physics of the HEMT, provides more insight regarding the analysis of radiation effects on this device.

1. GaN

GaN is a III-Nitride semiconductor material that has a Wurtzite crystal structure and is classified as a direct wide bandgap (3.4 eV at room temperature) material. Direct bandgap materials have the ability to emit light, which makes them applicable to optoelectronics in devices such as a light-emitting diode. Unique to the III-Nitride family is spontaneous and piezoelectric polarization that occurs due to an intrinsic asymmetry in the crystal structure. Piezoelectric polarization is important in the case of III-Nitride heterostructures such as alloy-AlGaN grown pseudo-morphically on GaN because of the inbuilt nature of the mechanical stress between the two layers [8]. These properties of III-Nitrides, as compared to other materials shown in Table 1, are reflected in the piezoelectric coupling constants of these materials, resulting in an increased strength of the interaction force to mechanical strain. Spontaneous and piezoelectric polarization can be used to form quantum wells of carriers with mobility approaching intrinsic levels.

Table 1. Semiconductor material properties, after [9].

Material	Bandgap (eV)	Breakdown Voltage (V/m)	Coupling Constant	Ionicity
Si	1.12	3.0×10^5	0	0
GaAs	1.43	4.0×10^5	0.068	0.310
InP	1.34	4.5×10^5	0.15	0.421
GaN	3.4	5.0×10^6	0.48	0.5
AlN	6.1	1.5×10^6	0.65	0.449

Alloying of some semiconductor materials enables tunable parameters in terms of bandgap and lattice constant to achieve advantages such as maximum sheet carrier density and barrier height enhancement due to polarization in an AlGaN alloy with 25 percent aluminum content [10]. In the case of GaN and AlGaN, used in this thesis, the bandgaps are 3.4 eV and 4.1 eV, respectively. The alloyed $Al_xGa_{(1-x)}N$ band gap,

$$E_{G,AlGaN} = x_{\%Al}(E_{G,AlN}) + (1-x)(E_{G,\mathrm{GaN}}), \quad (1)$$

is calculated dependent on the mole fraction x of aluminum (in this case, 27 percent), which is adapted from Vegard's Law [11].

2. III-Nitride Growth and Device Fabrication

Due to the high cost of bulk GaN, fabrication of GaN is typically undertaken heteroepitaxially. GaN is grown on a foreign substrate, such as Si, with multiple material buffer layers in between. The integration of III-V semiconductor devices on a cheap substrate such as Si benefits from the combination of unique optical and electronic abilities delivered by the GaN while also having the processing capabilities and low cost production of Si [12]; however, such devices typically display carrier trapping issues stemming from the lattice mismatch of the materials [12]. A key parameter affecting device operation is the dislocation density in the layer being grown. Reducing this density minimizes the line defects in the active area of the HEMT, which leads to better reliability and heterostructures that support high breakdown voltage and transconductance [13]. Semiconductors of the crystalline nature generally have four types of defects: point, line, planar, and volume [14]. While Mishra states that these defects are detrimental to the performance of electronic devices and should be avoided, it should be noted that not all defects are unfavorable. Some defects such as doping, which can be defined as a collection of point defects used in a region, are incorporated into semiconductors in order to make them function while other defects may be inert to device functionality.

In this thesis, the effect of localized volume defects and line defects or dislocations on HEMT performance is discussed. Each dislocation has a strain field associated with it that can reduce the polarization effect and, thus, the sheet carrier

density. High dislocation density compounds this strain and can appear in the epitaxial layering process, which degrades the effectiveness of the 2DEG., Dislocations also induce more electron scattering and adversely affect transport. These dislocations occur due to a lattice constant mismatch between materials such as GaN (hexagonal lattice constant, 3.19 Å) and Si (cubic lattice constant, 5.43 Å) or due to a difference in thermal expansion coefficients, which is important during the cooling process after growth. A comparison of these values can be seen in Table 2, after [15].

Table 2. Material lattice mismatch comparison to GaN, after [15].

Material	Lattice constant (Å)	Lattice mismatch to GaN (%)	Thermal expansion coefficient (10^{-6} K^{-1})	Thermal mismatch to GaN (%)
GaN	3.19		5.6	
Si (111)	3.84	16.9	2.6	54
AlN	3.11	2.5	4.2	25

These material differences cause a strain during epilayer growth and are relaxed by the formation of dislocations. The number and direction of crystal planes shifted by the dislocation has a magnitude and direction equal to what is called the Burgers vector *b* that is perpendicular to the line axis *t* as portrayed in Figure 1. Together, *b* and dislocation line direction *t* characterize a dislocation and as shown, slip occurs in the plane defined by these two directions. Analysis of Burgers vectors is useful in determining the effect of strain reduction and potential of accumulation of defects [16, 17].

In GaN, threading dislocations are dominant and remain in the epilayers. They consist of three types: screw, edge, and mixed [16, 17]. An important difference in these types are that screw dislocations have no hydrostatic strain that is required in order to relax the lattice mismatch strain in the crystal [18]. Edge dislocations, or at least mixed partials, are required to relax this strain and attract vacancies or other point defects [16]. These misfit dislocations in the interface initially correlate to the density of threading dislocations. As threading dislocations are mobile, in contrast to their misfit counterparts in the interface, the buffer layers can be utilized in device manufacturing are used to bend these dislocations out of the crystal and to reduce the overall threading dislocation density [18].

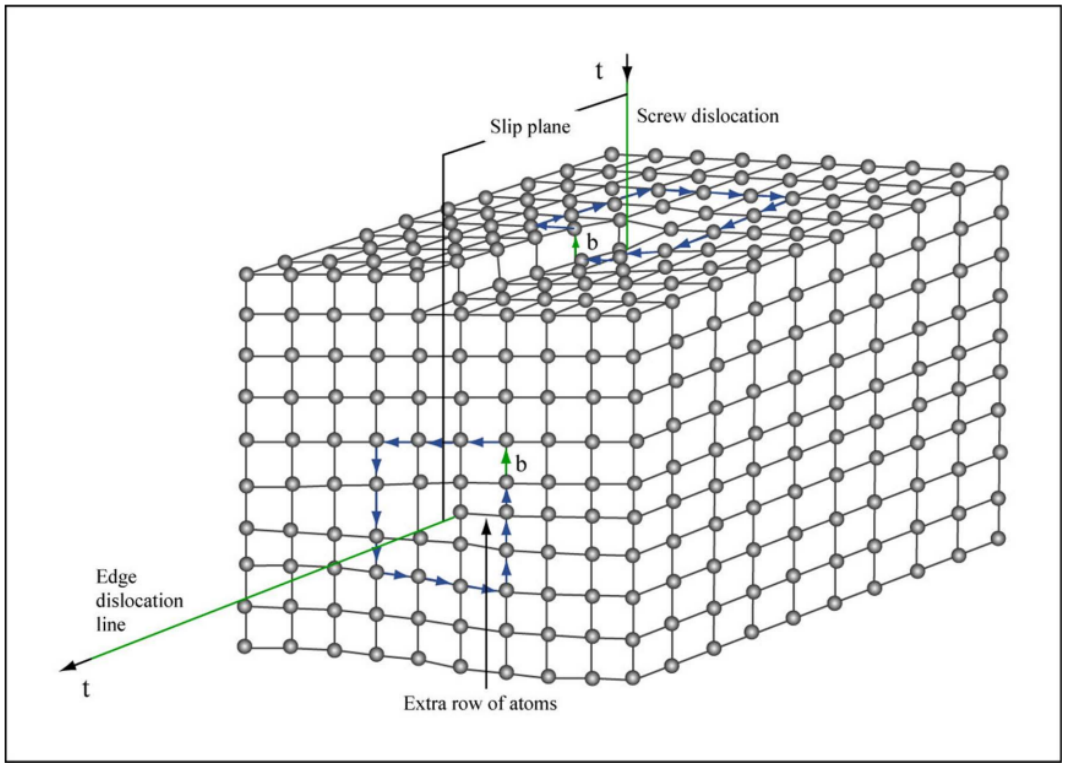

Figure 1. Burgers vector *b* and line axis *t* characterize two types of dislocations from MIT OpenCourseWare, from [19].

3. GaN HEMT Physics

A HEMT is a field-effect transistor (FET) that utilizes a spontaneously formed two-dimensional electron gas (2DEG) as a channel. This confines the wave function of electrons in the well, ideally eliminating dopant scattering in the vertical direction; thus, an increase in the electron mobility of the channel is observed, leading to improved performance for high frequency power applications due to the direct relation between channel mobility and the cutoff frequency of FETs. Such a device may also be known as a heterojunction field-effect transistor (HFET), modulation-doped field-effect transistor (MODFET), or a two-dimensional gate field-effect transistor (TEGFET) depending on the author. Due to the small channel width requirement for electron transport, HEMTs can utilize heteroepitaxially grown materials such as GaN that have relatively high defect densities.

GaN devices do not require doping due to the free charge that can be created by intrinsic piezoelectric and spontaneous polarization as seen in Figure 2. The positive sigma representing the effective sheet charge density induced by the net polarization at the interface of the heterostructure indicates that the carrier type is electrons. This charge attracts electrons to the interface, forming the 2DEG channel. The HEMT includes a heterojunction of two semiconducting materials with different bandgaps in which the difference ΔE_c leads to a quantum well where the conduction bands meet below the Fermi level as depicted in the band diagram of Figure 3. The channel of the HEMT can conduct at very low temperatures by avoiding the carrier freeze-out effect seen in doped semiconductors. Using GaN and other III-Nitrides, we can use HEMTs to achieve breakdown voltages an order of magnitude larger than breakdown voltages in III-Arsenides due to the high critical electric field level of the III-Nitride family, which stems from the higher band gaps [14].

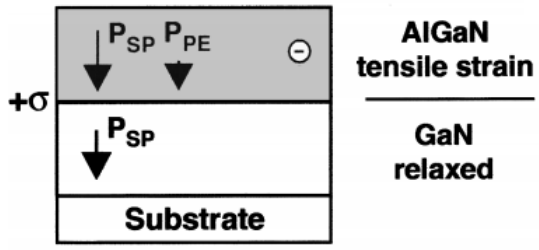

Figure 2. Polarizations caused by spontaneous and piezoelectric strain at the 2DEG interface, after [20].

While the lattice structures of both materials in a III-Nitride heterostructure are Wurtzite, the lattice constants are different. For example, in a GaN-AlGaN heterostructure, the interatomic spacing in the GaN is 3.19 Å and in the AlGaN is 3.49 Å, dependent upon the Al mole fraction in AlN (3.11 Å) and calculated using Vegard's Law. When processing HEMTs of this nature, the buffer layer growth on the substrate endures a strain, which is relaxed by the formation of dislocations. The strain of importance for the device functionality is modified when growing heterolayers on top of each other and during cooling of those layers, which changes strain due to differences in thermal

expansion coefficient of GaN and AlN, which are 5.6×10^{6} K^{-1} and 4.15×10^{6} K^{-1}, respectively [21]. For III-Nitride heterostructures, layers are grown pseudomorphically, and strain is maintained at the level induced by lattice mismatch. This strain in the device structure leads to the piezoelectric effect, which induces a charge that is proportional to the amount of Al in the AlGaN. Growth of AlGaN on GaN can be achieved without producing additional strain-relaxing dislocations, but at approximately 25 percent Al, the onset of dislocation formation occurs if the AlGaN layer is thicker than 20 nm to 40 nm. Polarization effects produce electrostatic charge densities, which accumulate as a 2DEG in an abrupt heterojunction interface due to differences in spontaneous polarization between the materials and an abrupt change in strain at the interface. This polarization charge attracts free electrons (see Figure 2) which then create the 2DEG channel in which the triangular quantum well has its electrons confined. This 2DEG is a function of sheet carrier density [22] where

$$n_s = \frac{+\sigma_B}{e} - \left(\frac{\varepsilon\varepsilon_0}{de^2}\right)\left[\phi_B + E_F\left(n_s\right) - \Delta E_c\right], \tag{2}$$

using bound positive charge at interface σ_B, elementary charge e, permittivity ε, vacuum permittivity ε_0, AlGaN width d, AlGaN thickness ϕ_B, Fermi energy level E_F, and conduction band energy level E_c.

The combination of piezoelectric and spontaneous polarizations effects provides high sheet carrier density and low on-resistance. With a deposited Schottky gate metallization, an applied gate voltage can be used to directly control the sheet carrier density. The 2DEG channel is the key component of the HEMT, which is determined by the amount of Al, interface roughness, alloy scattering, and dislocations [22], all of which affect carrier mobility. Semiconductor material selection to create the 2DEG provides the ability to control the carrier density, shape and conductivity of the channel. If an ohmic source and drain metallization is used to contact the channel, this control is consequently used to modulate the conductivity of the channel between contacts, creating transistor action.

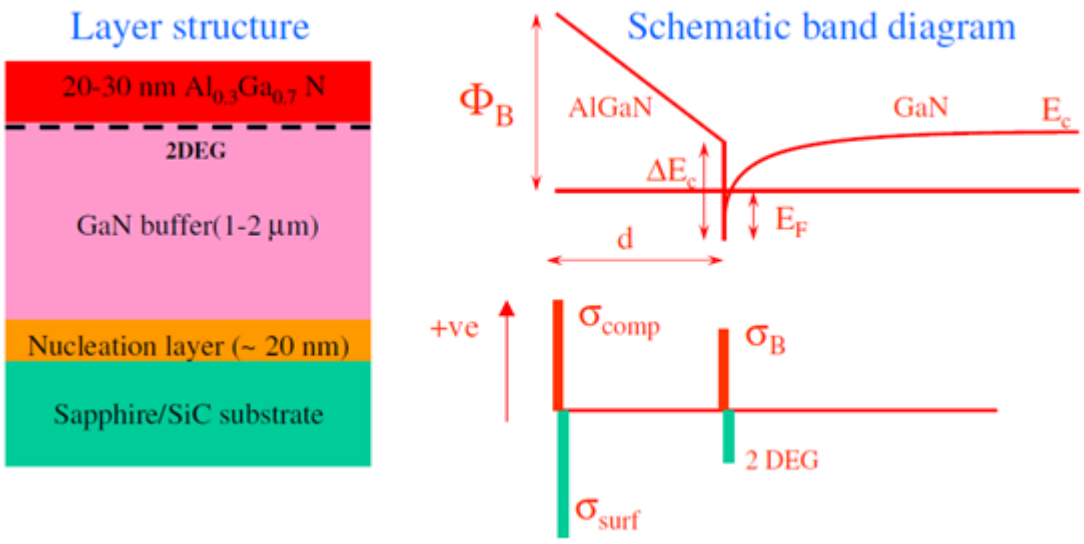

Figure 3. GaN HEMT structure with band diagram explaining formation of 2DEG, from [22].

4. Proton Radiation Effects

Previous studies of GaN/AlGaN HEMTs as discussed in [23] have found that such devices are very tolerant to proton irradiation, but the accumulated displacement-damage eventually results in device performance changes. This damage occurs when radiation in the form of particles scatters from atoms in a material's lattice structure and creates a pair of defects; an interstitial atom knocked from its lattice position and the corresponding vacancy known as a Frenkel pair (see Figure 4). Such defects interact with the carriers and increase scattering, which alters the mobility and sheet carrier density of the 2DEG within the device if those defects are located in its vicinity. There are also other mechanisms and secondary effects to these defects discussed in this thesis such as an accumulation of vacancies that can enhance atomic diffusion in the material. These defects and secondary processes ultimately lead to the degradation of electrical properties [23]. Ionization effects are neglected in this thesis research as they are not the primary source of observed permanent device performance degradation.

When dealing with displacement of atoms, the elementary theory is that a particle of energy E_i strikes lattice structure of the target material. A probability exists, given the known cross-section of the incoming particle, that an atom in the target material is struck.

This struck atom, now called a primary knock-on atom (PKA), has a known energy T and may collide with another lattice atom.

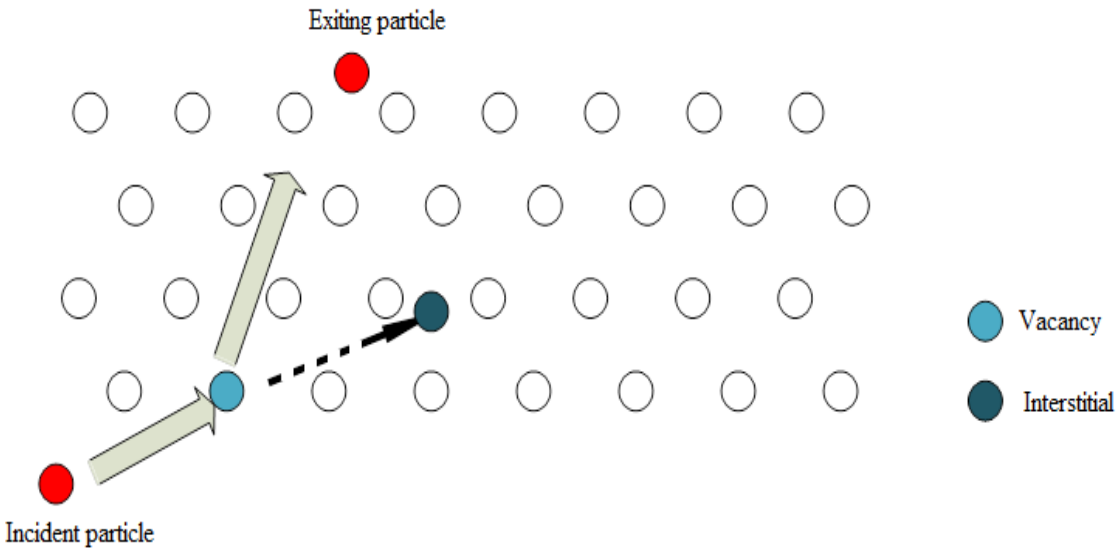

Figure 4. Displacement-damage due to radiation results in a Frenkel pair, vacancy and interstitial atom.

If this occurs, a cascading effect is seen when T is large enough to displace multiple atoms. This cascade effect also depends on the lattice density N. The probability that an atom is displaced depends on the value of T and T_d, the displacement threshold value (in eV) for a material. Kinchin and Pease (K-P) developed a model that utilizes the aforementioned parameters in order to calculate the total number of displacements, v(T) [24].

Non-ionizing energy loss (NIEL) is the total amount of energy that goes into displacements and is a valuable tool when describing displacement-damage that occurs in semiconductors [25, 26]. It takes into consideration the mean-free path between collisions λ and the energy lost T as the PKA and additional struck atoms move throughout the lattice. NIEL curves can be created for elements and compounds where the plot consists of eV density of a material versus the ion energy of the particles (protons in this thesis) that contact the material. NIEL curves can be compiled as functions of the incoming particle and target material's energy (E and T, respectively), threshold displacement

energy T_d, atomic mass M, atomic number Z, and density ρ. Nastasi developed such a function for the universal cross-section of ionic-interaction [26], which is used in

$$f(t^{1/2}) = \lambda t^{\frac{1}{2}-m}[1+(2\lambda t^{1-m})^q]^{\frac{-1}{q}} \tag{3}$$

to calculate the stopping power where t is a dimensionless parameter that relates collision to transfer energy of the target, m is mass of the target, and q is charge. The nuclear-stopping power energy can be calculated where

$$\frac{dE}{dx} = N\int_{T_d}^{T_M} T\frac{d\sigma}{dT}dT = \frac{\overline{T}}{\lambda}. \tag{4}$$

Equation (4) utilizes number of atoms per cubic centimeter in the target N, maximum transferred energy in a collision T_M, and energy-transfer-differential cross-section σ. This expression is modified using the Lindhard correction

$$L(T) = \frac{E_v(T)}{T} \tag{5}$$

where energy damage that produces displacements E_v is used to calculate NIEL values

$$NIEL = N\int_{T_d}^{T_M} T\frac{d\sigma}{dT}L(T)dT. \tag{6}$$

Once a *NIEL* value is obtained from a curve at a known proton irradiation, the concentration of vacancies

$$N_v = \frac{0.8\cdot\Phi\cdot NIEL}{2T_{d,avg}} \tag{7}$$

that are created by a fluence Φ of irradiation can be determined for each material present using the K-P equation.

B. NAVAL RESEARCH LABORATORY GALLIUM NITRIDE HEMT RETICLE

The GaN epilayer structure for the HEMT device used in this thesis research originates from Nitronex, Inc. The structure consists of a Si (111) substrate with epitaxial buffer layers of AlN, AlGaN and GaN which are deposited via metal organic chemical vapor deposition (MOCVD). A thin top layer of AlGaN with 27 percent Al was added as shown in Table 3, which lists all thicknesses and mole fractions of each material used in

ascending order from bottom to top of the structure. The various buffer layers are used to alleviate lattice mismatch with GaN, minimize threading dislocation density and maximize 2DEG control. The creation of the source and drain ohmic contacts involve definition, metallization, and annealing, while the gate metals are introduced via a photolithographic masking process. This epilayer then undergoes a plasma enhanced chemical vapor deposition (PECVD) process for the Si_3N_4 passivation layer. Contact window openings are created via inductive coupled plasma etching at 25 degrees Celsius. The metal overlay of titanium and gold are deposited via E-beam and lift-off techniques, and the final product is depicted in Figure 5. Each NRL reticle contains 36 HEMTs that have varying gate lengths of 3.0, 5.0, or 7.0 µm with a width of 100.0 µm. They have a 1.0 µm gate-to-source spacing and a 15.0 µm gate-to-drain spacing [27].

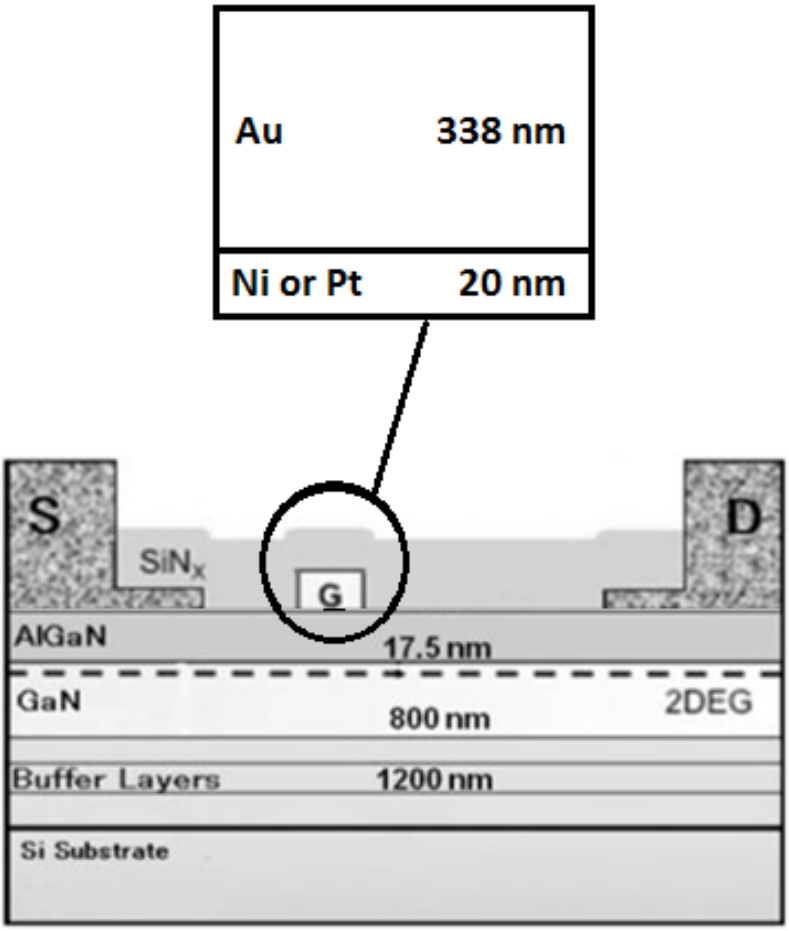

Figure 5. GaN HEMT structure, after [28].

Table 3. NRL epilayer materials and thickness ascending from bottom to top of wafer.

Material	Thickness	Atomic Percent (if applicable)
Silicon (111)	~200-500 μm	
Si_3N_4	1-2 nm	
AlN (compliance layer 1)	0.427 μm	1.0
AlGaN (compliance layer 2)	0.517 μm	0.8
AlGaN (compliance layer 3)	0.258 μm	0.5
GaN	0.8 μm	0.0
AlGaN (barrier layer)	17.5 nm	0.27

1. Unstressed Device Characteristics

Sample chips containing multiple HEMT devices were characterized at NRL as seen in Table 4. These chips have either Ni/Au or Pt/Au gating. There are no chips that have a mix of Ni and Pt gating materials. The values in Table 4 are very similar for Ni versus Pt and are measured again after irradiation.

Table 4. Device characterization for NRL GaN HEMTs, from [4].

	Ni-gate	Pt-gate
R_{SH} (Ω/□)	508	
μ (cm^2/V-s)	1430	
N_{SH} (cm^{-2})	$8.64x10^{12}$	
$I_{DS,MAX}$ (A/mm)	.195	.162
$I_{DS,MIN}$ (A/mm)	$5.86x10^{-4}$	$1.98x10^{-4}$
I_G (A)	$-2.54x10^{-5}$	$-1.03x10^{=5}$
R_{ON} (Ω-mm)	26.4	21.5
V_T (V)	-1.90	-1.73
$V_{BR,GATE}$ (V)	122	121

2. Electrically Stressed Device Parameters

As discussed in [5] by Wessel, NRL electrically stressed numerous devices located on the sample at the levels seen in Table 5. The effects of those stress levels can cause a collapse of drain current with a rate dependent upon the level of voltage stress as seen in the time-dependent measurement of drain current in Figure 6. While this occurrence is unexpected in other electrical devices as an increase in voltage over time should increase the current, it is often seen in GaN devices.

Table 5. NRL electrical stressed device identification and levels, from [5].

Pt		Stressed Levels	Stressed ID Number	FIB	TITAN
Fresh	NRL-10	NA	NA	Y	Y
Degraded	NRL-13	95V	R3GD15GF2DF2	Y	Y
Failed	NRL-12	135V	R3GD15GF2DF4	Y	Y
Ni					
Fresh	NRL-Ni-1	NA	NA	Y	Y
Degraded	NRL-Ni-3	130V	R3GD15GF2DF3	Y	Y
Failed	NRL-Ni-4	125V	R3GD15GF2DF4	Y	Y
Epi layer	NRL-Epi-1	NA	NA	Y	Y

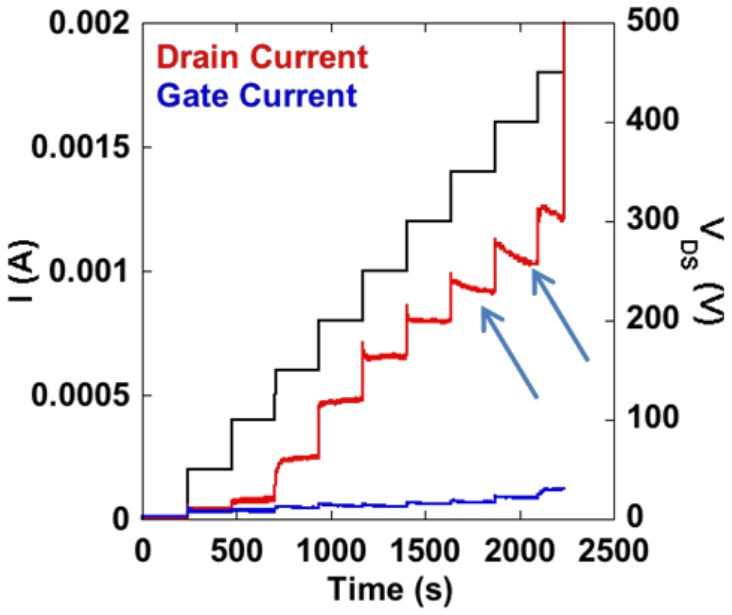

Figure 6. Step drain voltage stress testing of drain and gate current before and after irradiation where current collapse occurs, from [4].

The collapses may be associated with a combination of high fields and gate contact material utilized and likely occurs due to an increase in surface defects; however, specific defects have not been identified. Destructive physical analysis is used in this thesis to investigate the gate contact materials in order to observe defects that may occur in this location under proton irradiation.

3. Proton Irradiated Testing

The first set of HEMT devices from NRL on chip A were irradiated by 2.0 MeV protons via a tandem Van de Graaff accelerator at Auburn University at room temperature, approximately 20 degrees Celsius [27]. This sample was exposed to several fluences incrementally from 1.0×10^{12} H^+ cm^{-2} to 6.0×10^{14} H^+ cm^{-2}, where the maximum temperature during exposure did not exceed 40 degrees Celsius. The parameters (2DEG mobility, 2DEG sheet charge density, sheet resistance, on resistance, saturated transconductance, and threshold voltage) shown in Table 6 and Figure 7 were characterized electrically by NRL in between each fluence of the experiment. It is seen with this data that GaN HEMTs display a high tolerance to proton irradiation where severe degradation does not occur until a dose rate of approximately 5.0×10^{13} H^+ cm^{-2} [4]. The saturated transconductance, or ratio of change in the drain current given a variation in gate-source voltage over an interval while maintaining drain-source voltage, had the most significant loss.

Table 6. NRL proton testing parameters, from [4].

Parameter	Units	Before Radiation	Dose = 6×10^{14} cm^{-2}	Percent Change
μ_{2DEG}	$cm^2/(V\cdot s)$	1259	894	−28.9%
n_{2DEG}	10^{12} cm^{-2}	7.28	6.25	−14.1%
R_{SH}	Ω/□	683	1120	64.0%
R_{ON}	Ω-mm	32.7	57.7	76.2%
$G_{M,SAT}$	mS/mm	102.2	62	−39.3%
V_T	V	−2.01	−1.65	−18.2%

Further data obtained from NRL's experiment can be seen in Figure 8 and Figure 9, where the before and after proton irradiation effects on drain current versus gate to source voltage and drain current versus drain to source voltage are shown, respectively. It can be seen that the drain current is reduced after irradiation. The degradation seen in the I-V curves and the shift in threshold voltage can be explained by a reduction in sheet carrier density and an increase in trapping [4]. In Figure 8, a reduction in leakage current within the blue oval is shown with irradiation. This result was unexpected as defect formation by irradiation was expected to result in an increase in leakage. In Figure 9, a reduction in drain current is seen at three different drain-to-source voltages.

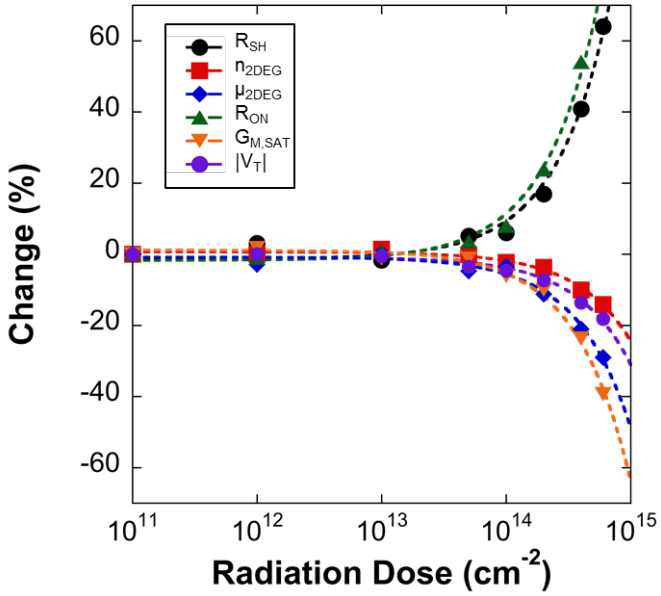

Figure 7. NRL parameter changes with increased proton irradiation dose, from [4].

In Figure 10, the dynamic on-resistance, a strong function of surface defect density, is seen to increase after irradiation. It is seen that this parameter is more sensitive to proton radiation damage than other electrical parameters. This dynamic on-resistance is more a function of the surface defects of the device, and since the reduction in on-state current is likely caused by reduced mobility and sheet carrier density, this leads to the conclusion that more surface defects are created by irradiation [27].

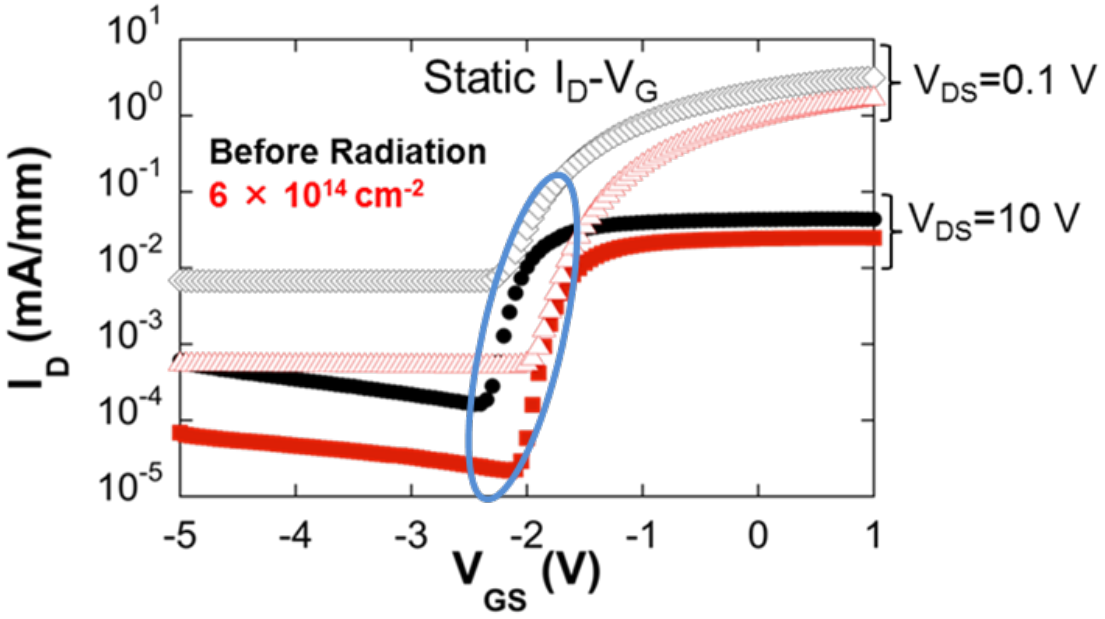

Figure 8. Proton irradiation decreases the drain current versus V_{gs} at two different drain to source voltages, after [4].

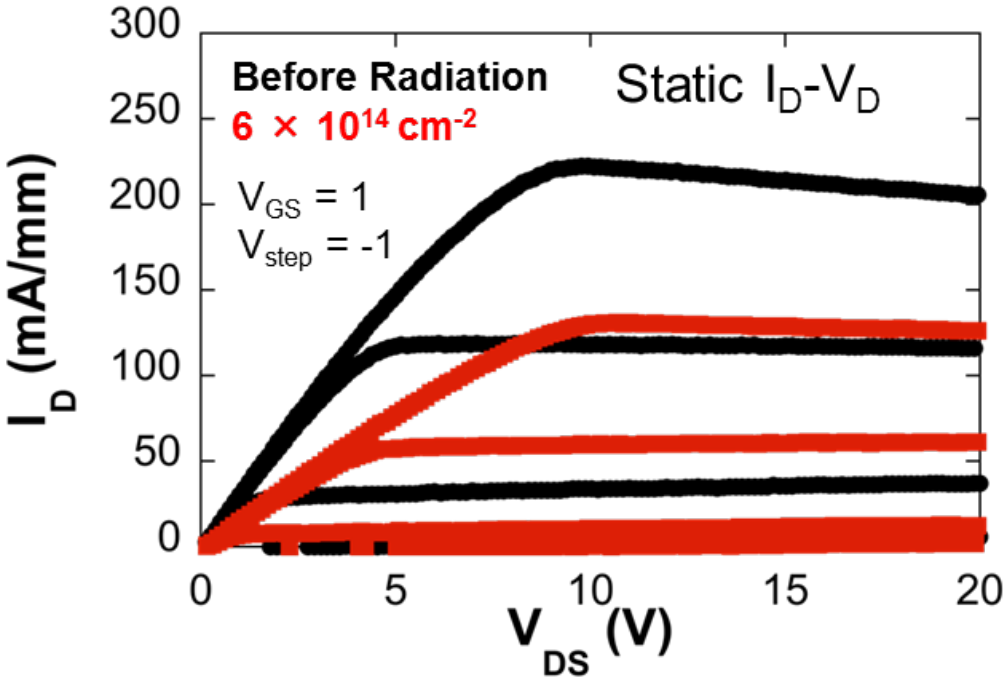

Figure 9. Proton irradiation decreases drain current versus at three different voltages of 1,0, and –1 V, from [4].

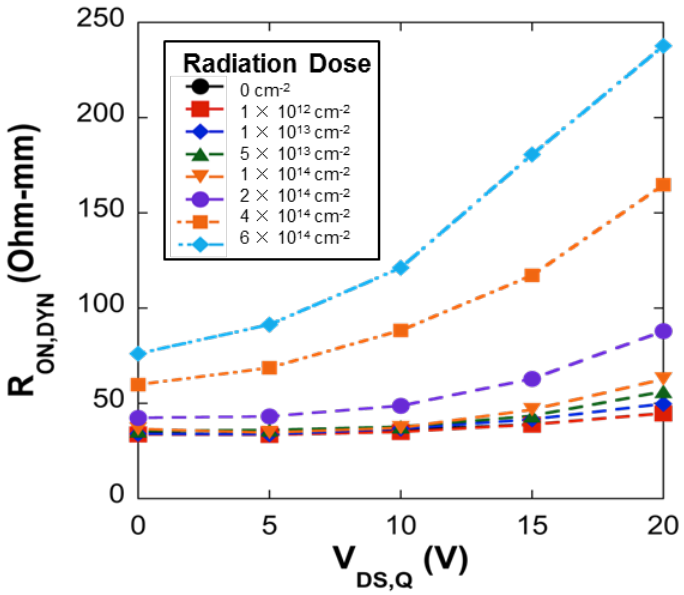

Figure 10. Increased proton irradiation increases $R_{on,dyn}$, from [4].

C. MICROSCOPY

Microscopy is the technical term associated with the viewing of an object at a resolution beyond the human eye using a microscope. For this thesis research, multiple types of electron microscopy were conducted. Electron microscopy can be used at higher magnification than optical light microscopy due to the small wavelength of electron beams (approximately 2.0 pm wavelength for 300 kV accelerated electrons) [18]. In electron microscopy a beam of accelerated electrons passes through multiple electro-magnetic lenses and apertures in order to obtain an image. The quality of those lenses is essential for the interpretability of the respective images [29].

There are many types of imaging such as: secondary electron (SE), backscatter electron (BSE), forescatter electron (FSE), cathodoluminescense (CL), and STEM [30]. In this thesis SE imaging, which is used for small volumes and contains topographic information, is used.

1. SEM

Scanning electron microscopy uses electrons instead of light in an optical microscope to obtain an image of the specimen, as portrayed in Figure 11. This is

accomplished in vacuum with a beam of electrons that travel vertically down from the gun at the top of the scope [30]. This beam travels through electromagnetic fields and lenses where the beam is focused on the specimen. Electrons hit the sample, ejecting backscattered and secondary electrons and x-rays which are converted into signals [30]. A two-dimensional image that can be viewed on screen is produced by scanning with the focused electron beam over the sample area and plotting the signal from each area as one grey intensity value [29].

SEM imaging techniques are utilized to analyze surfaces for defects and composition and the samples are relatively easy to prepare as thickness is not an issue. For this thesis research, NRL chips were mounted to the pedestal and holder and then loaded into the microscope's vacuum chamber for imaging.

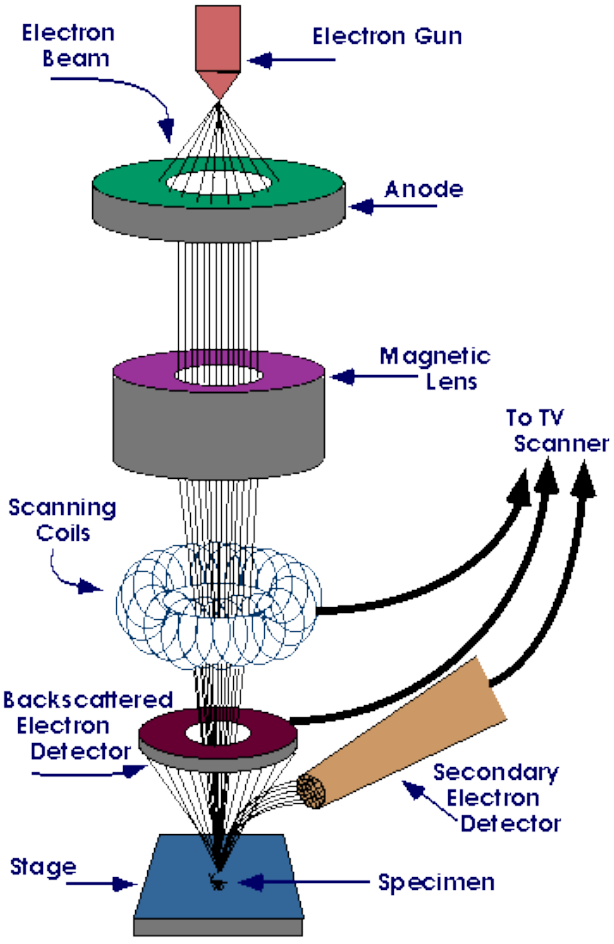

Figure 11. SEM illustration of internal components, from [31].

2. FIB

The focused ion beam works similar to the SEM, but the FIB uses a Ga source which is concentrated on select areas for removal of material for underlying analysis or for use in cutting out smaller samples as needed for other microscopy [31]. The I-beam is also used for imaging and must be utilized when operating the I-beam as a cutting tool because only this image previews exactly where the cut occurs. Since ions are heavier than electrons, the ion beam is typically utilized for milling as it achieves the desired effect in a more timely manner. The SEM and FIB are co-located in the same microscope with an offset angle of 52 or 54 degrees as represented in Figure 12. In this thesis research, we used the FIB to strip gate finger Si_3N_4 and Au material as well as for cutting material to prepare TEM samples in a standard lift-out technique.

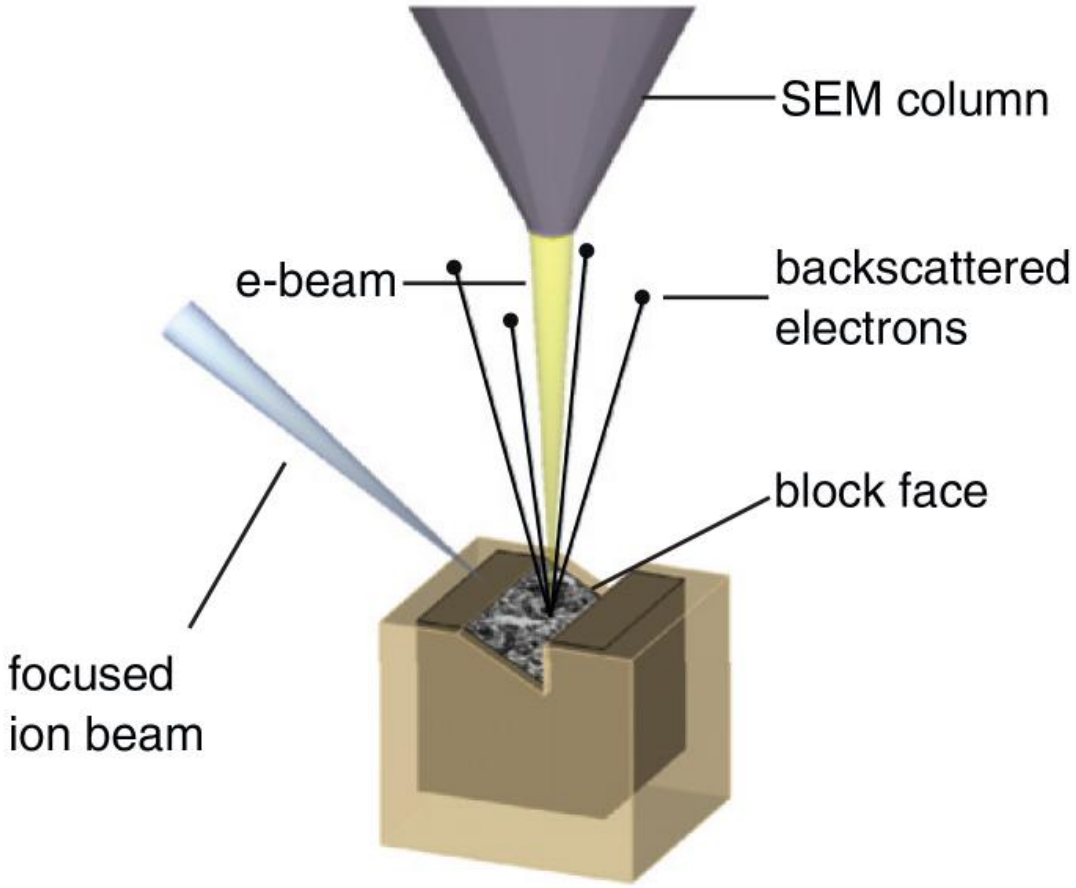

Figure 12. SEM and FIB orientation inside microscope, from [32].

3. TEM

The transmission electron microscope is utilized to analyze atomic level lattice structures, crystallization, and local composition [33]. This requires a much thinner sample than an SEM sample and can be prepared using the SEM/FIB. This microscopy is useful in the analysis of dislocations, precipitates, grain boundaries, and even point defects via a two-dimensional picture with much greater resolution than that of an SEM. The basic process of imaging with the TEM can be seen in Figure 13, where an electron beam passes through a thin (approximately 150 nm) sample, and the scattered electrons are used to form the image [33]. The process in which this image is formed depends on the type: high-resolution, conventional, or STEM. STEM imaging, which is discussed next, is utilized in this thesis research.

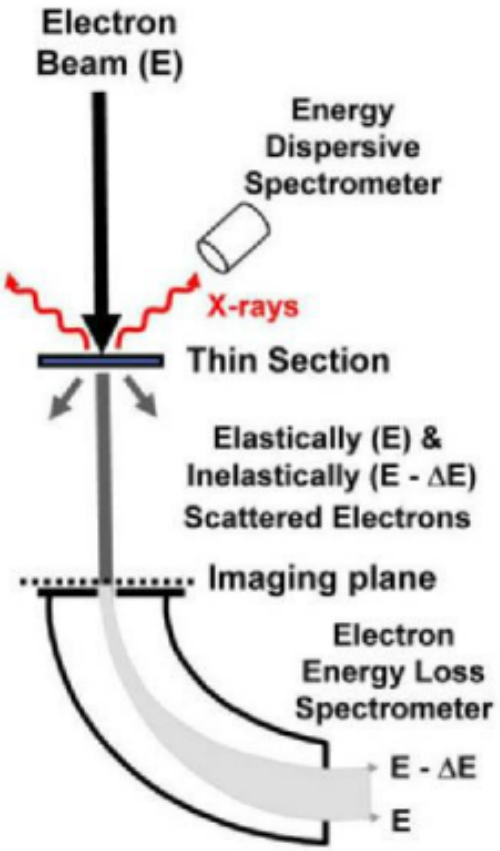

Figure 13. TEM illustration showing physical location of sample, imaging plane, EDS, and EELS, from [33].

4. STEM

Scanning transmission electron microscopy is a combination of SEM and TEM technology that offers performance enhancements at intermediate voltages and achieves image resolution improvement much like the gains seen in a standard TEM [29]. The electrons, which are elastically scattered at high angles, lose coherence and, consequently, cannot produce phase contrast images any longer. The contrast used in this type of microscopy is chemically sensitive with an approximate squared relationship to the mass of the respective element [18]. The electrons are detected in a high angle annular dark field (HAADF) detector. STEM also requires a thin sample like TEM, and the image is formed by interpretation of the intensity measured in each scanning "spot." There are no atom columns or contrast present in these "spots"; this is why crystal structures can be seen. The size of the beam "spot" largely determines the spatial resolution of the image [18].

High-resolution STEM uses a high intensity, focused electron beam for an imaging technique that is useful in analyzing features of thin electronic devices [29]. By aligning the electron lenses over the sample in a small probing area the user can obtain atomic resolution images and, with the HAADF, interfacial boundaries and defects can be seen. This technique of imaging is effective in denoting changes in crystalline structure; however, it is not typically useful for viewing amorphous structures [18, 29]. This type of microscopy is also not useful for light elements as the signal-to-noise ratio is too small to view them. They appear dark, the same as the channels next to the atom columns [18].

5. EDS

Secondary radiation induced within SEM and TEM microscopes can be used for spectroscopic purposes. When the incident electron beam is used to strike the sample, it emits secondary electrons, backscattered electrons, and x-ray signals from the surface [29]. As the impact of the primary electron beam occurs, there are many atoms that are left with holes where a secondary electron once was. When these holes are located in inner shells, these atoms are no longer stable. Outer shell electrons at a higher energy state jump to the inner shell holes in order to stabilize the atom but first must lose energy,

which takes the form of x-rays. This x-ray energy can be correlated to periodic elements by referencing their energy and wavelength. It also determines which shell lost an electron and which shell filled the hole [34].

This equipment and software allows the user to obtain periodic element mapping of the sample from the EDX spectrometer in the form of images, maps, and line scans as shown in Figure 14 and Figure 15. This imaging technique processes data and produces line scans as an elemental map image or area scans as intensity plots for the x-ray signals and is particularly useful in material composition analysis [34].

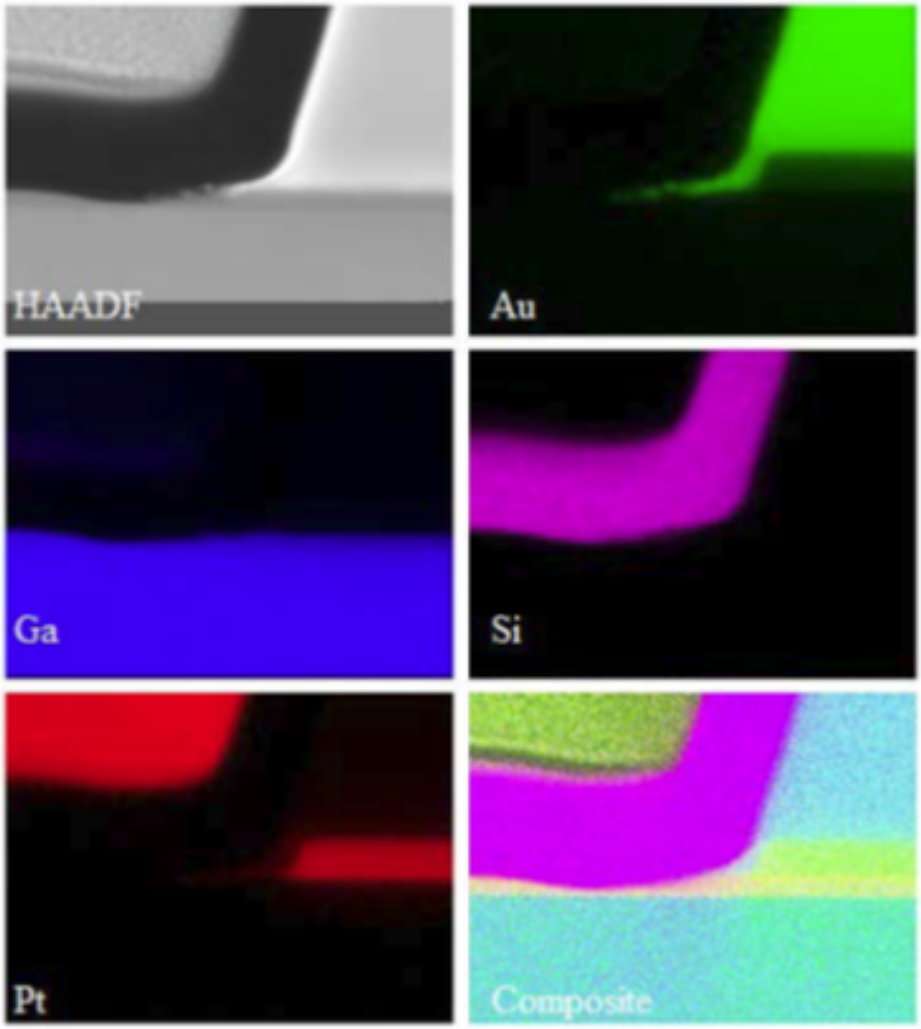

Figure 14. STEM image using EDS for elemental mapping, after [5].

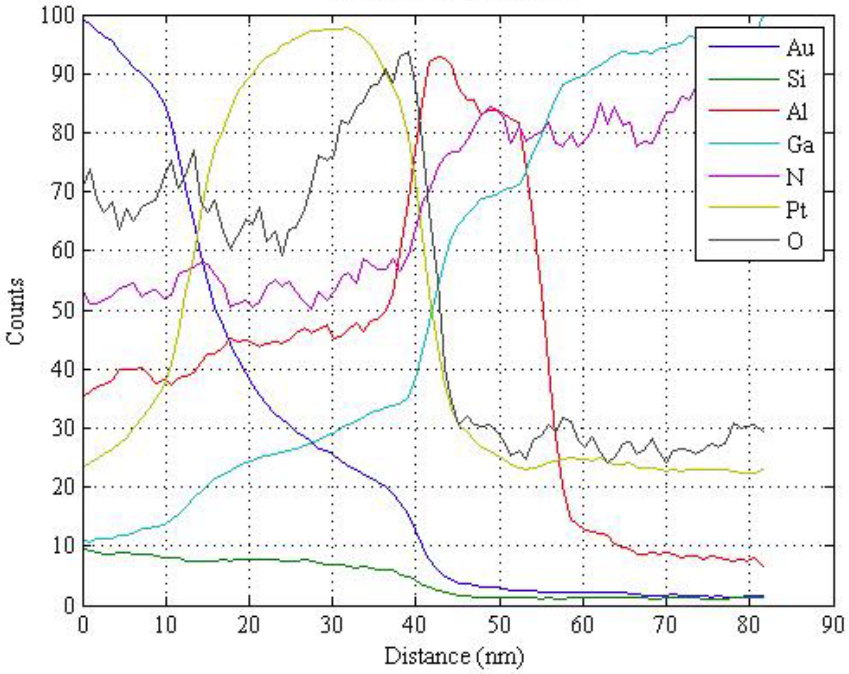

Figure 15. Example of an EDS line scan, from [5].

III. SAMPLE PREPARATION

A. LOCATIONS AND MACHINES UTILIZED

Lawrence Berkeley National Laboratory located in Berkeley, California, is the main site utilized for research material in this thesis. The National Center of Electron Microscopy is responsible for a vast majority of the training required for the conduct of this research. State-of-the-art equipment at this national user facility used for this thesis research included: the SEM, FIB, plasma cleaner, ion NanoMill, STEM, and EDS. The second location utilized for this research is at the Naval Postgraduate School (NPS), Watkins Hall, which houses an SEM, FIB, EDS, and TEM. Machine availability is much greater at NPS and aided in reducing the time spent at LBNL by conducting certain time-consuming procedures here. Research collaboration also occurred at the Naval Research Laboratory's Electronics Science and Technology Division in Washington, DC, where the devices were created, irradiated, and characterized. Lastly, a HR-STEM was utilized in Juelich, Germany, where some samples were further examined at the atomic scale resolution.

B. FOCUSED ION BEAM MILLING AND LIFT OUT

1. Initial Setup

The first step in the process was to properly mount the sample, an NRL integrated chip with multiple devices on it, to an SEM stub pedestal and holder similar to the one shown in Figure 16. To do this, the user must wear latex gloves and apply a thin 3M double-sided carbon tape to mount the chip on the pedestal. Each side edge of the tape was rolled inwards toward the chip to prevent any lateral movement of the chip once inside the microscope. Figure 17 is a picture of a mounted sample before the tape has been rolled. This is extremely important inside the vacuum sealed SEM as the sample holder is tilted to various degrees while obtaining eucentric height, the coincidence point, and while operating the FIB. Once the sample is mounted, the SEM can be vented and the sample loaded onto the tray. Once loaded, the loading drawer can be shut and the vacuum applied. At the proper vacuum level, the sample can be moved into position to begin work.

Figure 16. SEM Specimen Stub Pedestal on Holder.

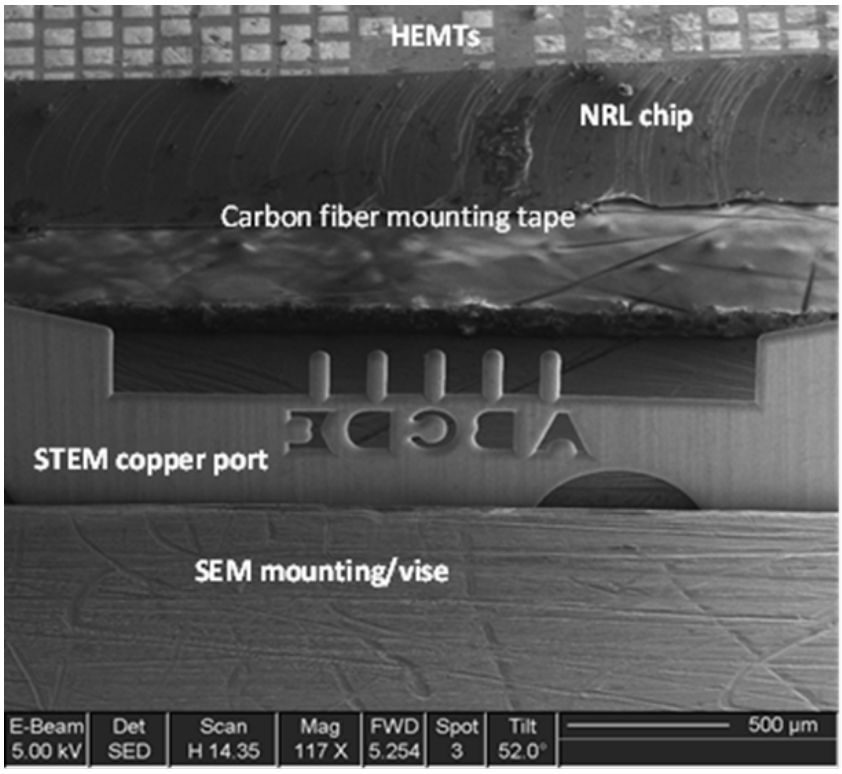

Figure 17. NRL chip mounted to SEM pedestal with carbon fiber tape along with STEM copper port.

This process was initialized by starting at a very low magnification to approximate the proper alignment for the E-beam as seen in Figure 18. The user must then drive the stage up to the proper working distance, 5.0 mm in this case, and focus at an increased magnification of approximately 5,000. From here the stage is tilted at various angles and focused while resetting the working distance as needed in order to find the eucentric height.

This height ensures that the E-beam is focused on the work area for multiple angles, up to 52 or 54 degrees, depending on the SEM's FIB setting. The next step was to find the coincidence point by monitoring a point while switching between SEM and FIB

modes and adjusting the stage height as needed. This ensures that the E-beam and I-beam are focused at the same point for scanning and milling. The user can now locate the device to analyze as shown in Figure 19.

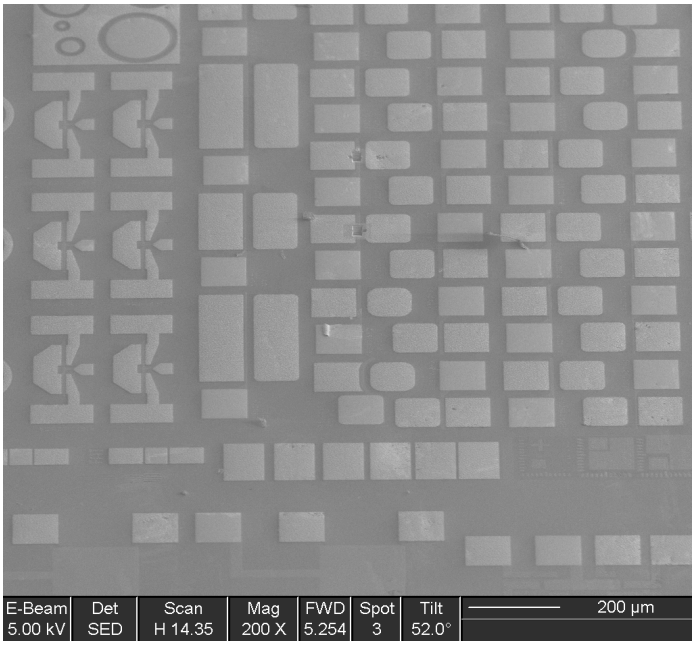

Figure 18. NRL chip SEM overview consists of various devices with HEMTs located in the first quadrant.

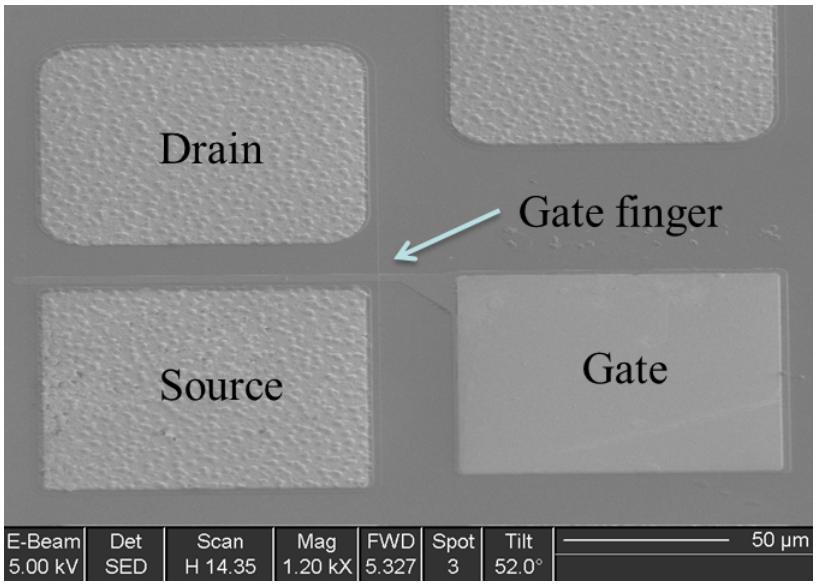

Figure 19. GaN HEMT device depicting the drain, source, and gate.

2. Sample Protection

Protecting the sample is very important during SEM and FIB operation because each scan damages the specimen with electrons or, worse yet, with Ga ions. It is important to minimize E-beam and, especially, I-beam exposure, which is accomplished by minimizing continuous scanning, using single-frame scanning, or freezing the scan when it is not required. Along with minimized exposure, the use of Pt deposition was utilized to protect certain areas to be explored later, such as TEM lamella. This is completed simply by heating the Pt source for the required time and then drawing the desired shape on the sample. Pt deposition was processed via the E-beam, where the heated Pt atoms were guided by the electron beam toward the specific sample area drawn upon the sample as seen in Figure 20. This Pt deposition protects the area-of- interest underneath while further electron scanning and ion milling are conducted to remove the lamella. The process is also useful for protecting samples and maintaining their integrity so that the user can return at a later date for further testing.

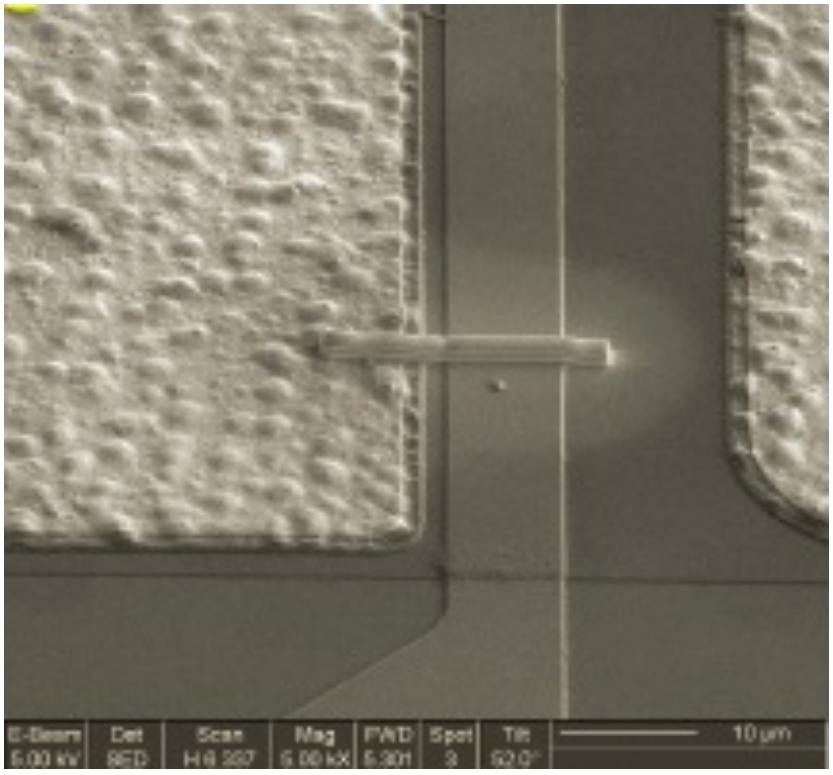

Figure 20. GaN HEMT gate finger with protective Pt deposition, from [5].

3. Ion Cutting

Focused ion beam cutting is conducted by drawing the shape required with the software tools and using the Ga ion beam. It is important to heat the ion gun approximately 15 minutes before use to obtain the appropriate stabilized current. Once heated, the settings to perform cutting must be as low as possible to minimize the exposure of the device to Ga ions. The FIB is a powerful destructive physical analysis tool which is used in this thesis research for stripping the gate finger's Si_3N_4 passivation layer and the Au gate metallization layer depicted in Figure 21. Here, the settings for the I-beam were 30 kV, 300 pA, and milled for depth of 0.1 μm on parallel mode.

The FIB is also utilized to cut deep trenches and an "L" shaped undercut, which leaves the sample attached by a small tab, in order to extract the lamella for TEM analysis as seen in Figure 22.

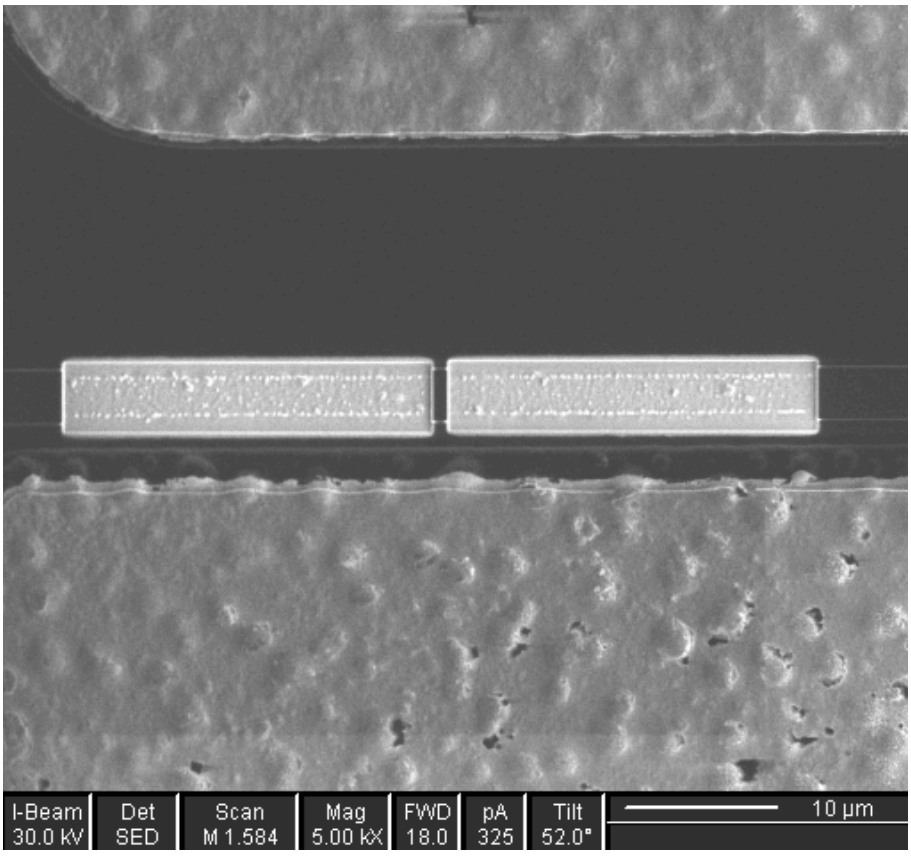

Figure 21. GaN HEMT device with gate finger stripped of Si_3N_4 and Au via FIB.

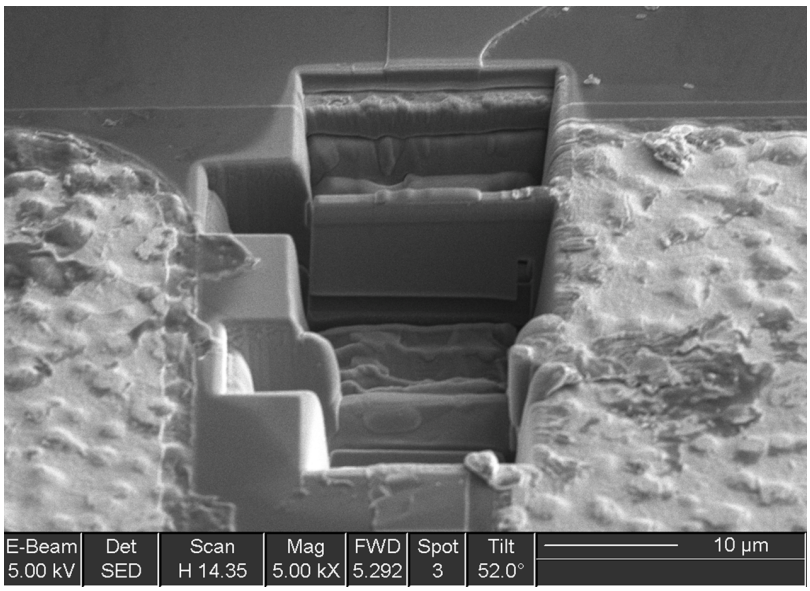

Figure 22. FIB trenches cut into gate finger with "L" undercut to remove lamella for TEM.

4. Lift Out

The removal of a TEM lamella from the device is completed through the use of an Omni Probe.

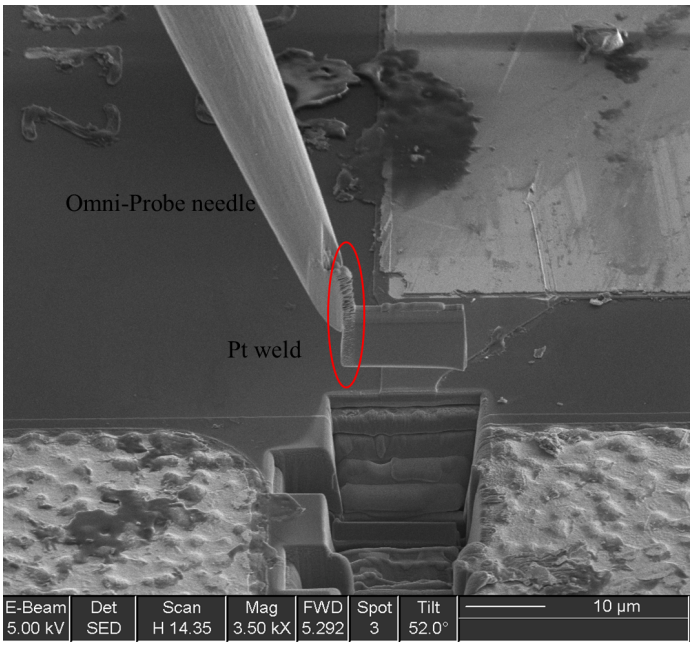

Figure 23. Lamella Pt welded to Omni Probe for lift out.

The Omni Probe needle device is attached to a gun, which inserts the probe near the working platform. Stabilization of the needle is the key to a successful lift out procedure. Once the needle has stabilized, the user drives the stage carefully toward the probe and inserts the probe into the side trench created by the FIB, just touching the lamella. The heated Pt source is used to weld the Omni Probe to the lamella. Once welded, the lamella's connection tab remaining from the undercut near the source is cut with the FIB. The lamella is now free to be extracted via Omni Probe as shown in Figure 23.

5. Mounting

Once the lamella has been extracted from the device, the stage is moved away from the Omni Probe and repositioned to weld the lamella to the TEM copper port previously shown in Figure 17. For this process, a rectangular trough is cut into the side of the copper port, where the lamella is docked. The lamella is then Pt welded onto the port and the needle weld is cut away as seen in Figure 24.

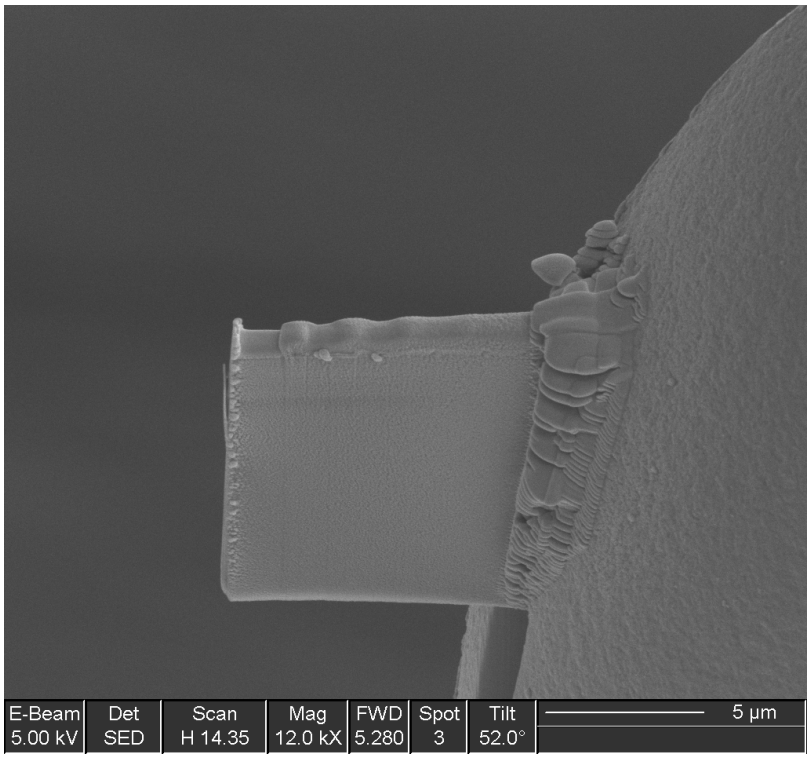

Figure 24. Lamella welded to TEM copper port.

C. NANO ION MILL

The NanoMill is utilized for fine thickness reduction in creating TEM samples and to remove the amorphous surface area in a cleaning process. This ion mill utilizes an energy setting of approximately 500 eV to 900 eV with a beam current between 100 pA to 200 pA and is much more accurate in the milling process than the FIB used to cut out the rough lamella. In this thesis, the ion NanoMill was used, in order to explore lamella in the TEM, which require thicknesses less than 200 nm for atomic resolution.

Once the lamella has been welded to the TEM copper port, the specimen can be thinned via the ion NanoMill as seen in Figure 25. This machine is relatively easy to use via the software provided and allows the user to precisely mill the sample to the required thickness for STEM analysis.

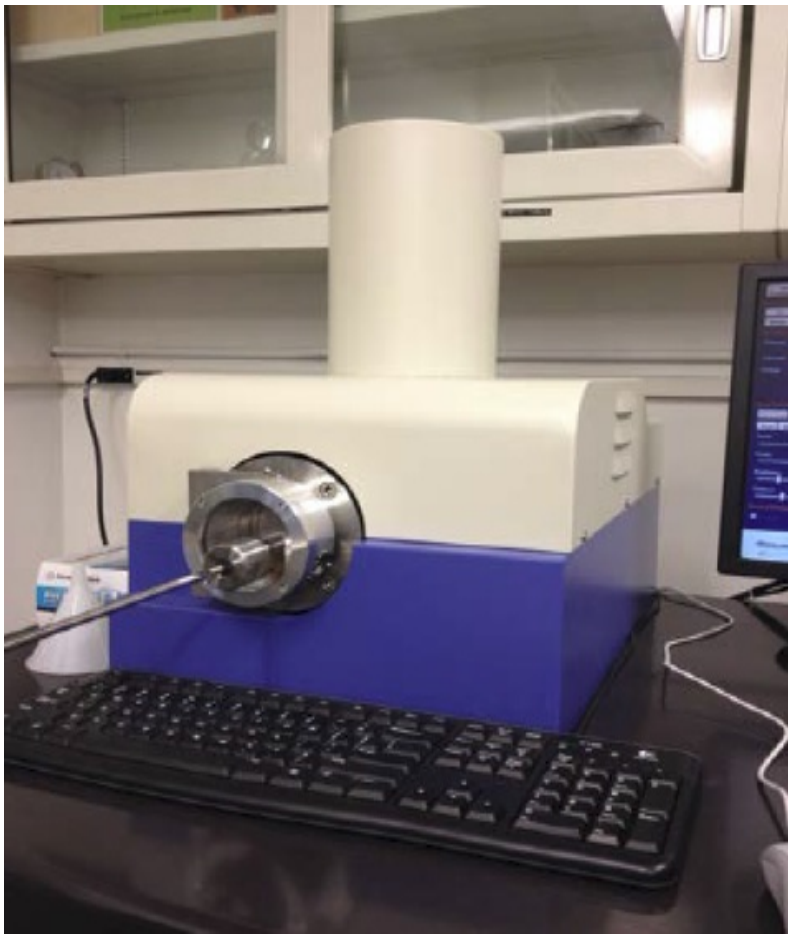

Figure 25. Ion NanoMill used for thinning lamella for STEM, from [5].

D. PLASMA CLEANER

A plasma cleaner is utilized for removing contaminants from the surface of a sample before it is analyzed in a TEM or STEM. This process uses dielectric barrier discharge plasma created from argon and oxygen and efficiently removes hydro-carbon molecules. This type of cleaning was used in this thesis research for STEM research of the gate finger lamella in order to avoid surface contamination related artifacts in the images [18].

E. SAMPLE AND COMPARISON TO PREVIOUS WORK

All TEM samples created for this thesis research were created in a similar fashion to those successful specimens created by Wessel in [5]. Once the selected areas of the gate finger had lamella removed for analysis, one device is chosen as a backup sample for future reference to receive a Pt deposition layer over the gate finger for protection. Several other devices on this NRL sample are then stripped of the gate finger's Si_3N_4 layer and Au layer via FIB in order to visually inspect the layer of Ni and the defects associated with it.

F. GATE FINGER STRIPPING

1. LBNL Strip Depth

In previous work conducted by NRL, a bias was placed on the HEMT device in order to identify areas of concern with electroluminescence (EL). A novel technique was developed at LBNL for this thesis research in order to investigate extended defects which are located near the surface, at a clearly identifiable depth, in this case located in the 20.0 nm thick Ni layer of the gate finger. The gate fingers were stripped, as illustrated in Figure 21, to examine the gate finger beneath the Au contact metal for underlying defects in the Ni or Pt layers. This process was completed by using the FIB with the sample at a eucentric and coincidental stage height to the SEM. The FIB software was used to draw a rectangular shape to be milled away at a prescribed depth, voltage, and current. A detailed honing of the depth required to remove the Si_3N_4 and Au layers while maximizing the remaining Ni layer was conducted at LBNL by stripping a gate finger in

staircase fashion of increasing depth. This sample was then removed for STEM analysis to pinpoint the depth required at 80.0 nm as shown in Figure 26. All FIB stripping conducted at LBNL provided cleanly stripped samples of uniform milling quality. In this thesis, the new technique was used to strip the entire length of the gate finger and analyze the circular void shapes in order to produce a statistical model of the defects in terms of size and distance from the centerline of the gate finger and/or from the source.

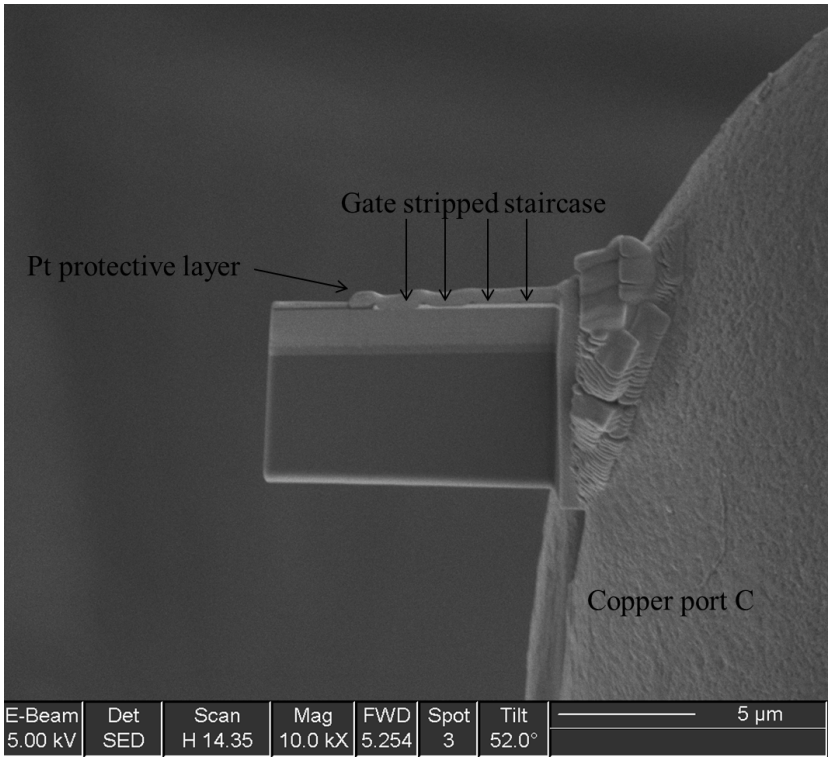

Figure 26. Lamella prepared for STEM analysis showing staircase FIB stripping.

2. NPS SEM Trials

Due to SEM availability, time-consuming operations such as the full gate finger stripping of the Si_3N_4 and Au layers on all devices to view Ni voiding were scheduled to be performed at NPS. It was important to produce the same results that the LBNL SEM yielded in terms of milling quality. In order to complete this task, the FIB was set in parallel milling mode. In this mode, the entire object to be milled was split into subsections but milled concurrently. By doing this the material being milled was not re-

deposited within the milled area, creating steps along the way which mask the actual defect structure. Contrary to this method is the serial-milling mode, which subsections the shape and mills each smaller block consecutively. This type of milling does not leave a clean surface for analysis due to re-deposition.

As the first user at NPS to attempt this type of quality milling, we discovered that the SEM/FIB at NPS cannot conduct parallel milling.

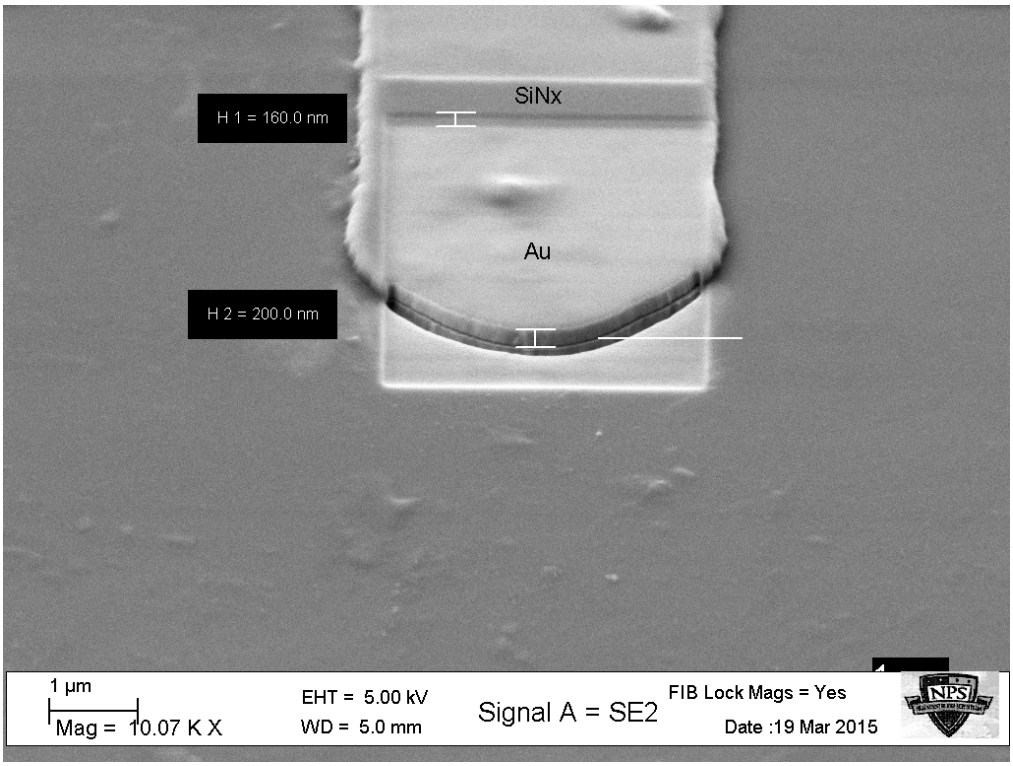

Figure 27. Tip of Ni/Au gate finger stripped to identify depth of Ni measured 360 nm.

This was confirmed by the Zeiss technical representative, who stated that the NPS machine is not equipped with the hardware and software to perform parallel milling. There were still many tasks that could be performed at NPS, and we invested time into the machine to test its capabilities. While quality parallel milling cannot be conducted for multiple gate-stripping, the machine is able to produce a "clean" cut at reduced current. Many trials were conducted as seen in Figure 27, where the depth of cut required is verified. It can be seen that at 360.0 nm, a defined layer of material is visible. By

comparing Figure 27 to Figure 28, we can see that at approximately 360.0 nm there should be the presence of Ni.

Once the depth was confirmed, milling trials ensued where we attempted to obtain quality milling in serial mode by varying the current and depth parameters. During each of these trials, we performed EDS as shown in Figure 29, where we were looking for removal of AuM (shown in dark blue) with maximum NiL (shown in red) when two rectangular shapes were milled across the gate finger. The designation of M, L, or K after an element represents the orbital shell from which that the electron came. The corresponding line plot was created within the Esprit 1.9 software where energy and wavelength data is referenced to reveal the elements that are present. The *y*-axis of this plot is the number of counts each element received, indicating its strength of presence.

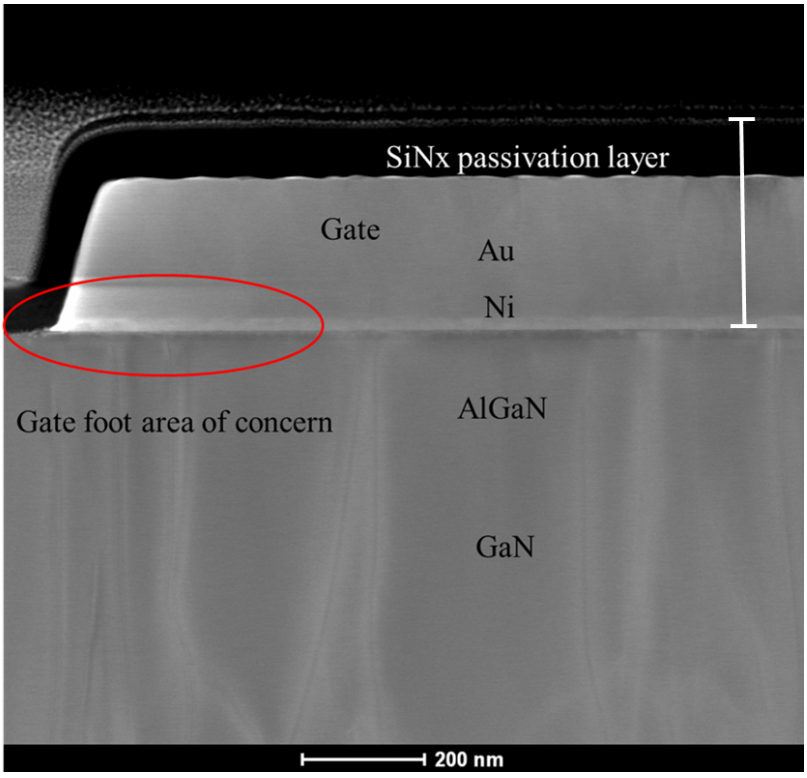

Figure 28. STEM analysis showing Ni layer at approximately 360.0 nm.

After approximately 50 hours of logged trials, we determined that a quality cut could be produced at 10.0 mA vice the 300.0 mA used at LBNL, but this proved to be too

time consuming. The trials also included testing the milling parameters for depth versus milling for time. Here, it was found that depth milling utilized the material parameter setting chosen, Si in this case, and calculated the time to cut that depth. The problem with this setting is that the device is not comprised completely of Si. As discussed in Chapter III, this device has Si_3N_4 and Au layers that must be milled to reach the Ni layer. Manually attempting to obtain the desired mill depth within the 20.0 nm thickness of this Ni layer proved to be very difficult at NPS, and it was determined that, for repeatability purposes, the full finger gate milling should be milled at LBNL.

The NPS machine is still very useful for SEM analysis, larger milling depths, creating TEM trenches and analyzing void size and location data once the gate fingers are stripped. With this machine, we also confirmed that using the Ga ion beam for cutting results in a partial Ga implantation into the surface are (see Figure 29), an important finding which impacts future FIB produced TEM samples.

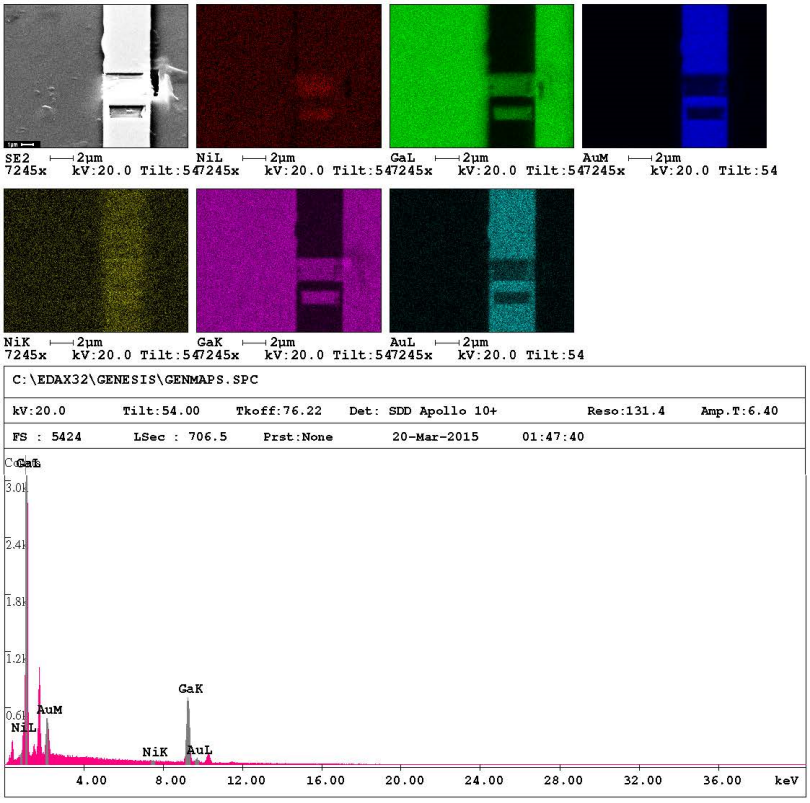

Figure 29. EDS depth trials of Au removed (blue) and Ni remaining (red).

THIS PAGE INTENTIONALLY LEFT BLANK

IV. RESULTS

A. VOID DISCOVERY

In collaboration with NRL and UCB team members, the initial work from this thesis research contributed toward a publication covering the proton radiation effects seen in GaN HEMTs [27]. In this paper, AlGaN/GaN HEMTs that were subjected to proton irradiation were shown to have developed a degradation mechanism, voiding in the Ni layer at the edges of the Ni/Au gate. The hypothesis of the mechanism underlying this void creation is that diffusion led to their formation. The result is a reduced effective gate area which influences the electrical performance of the device [27].

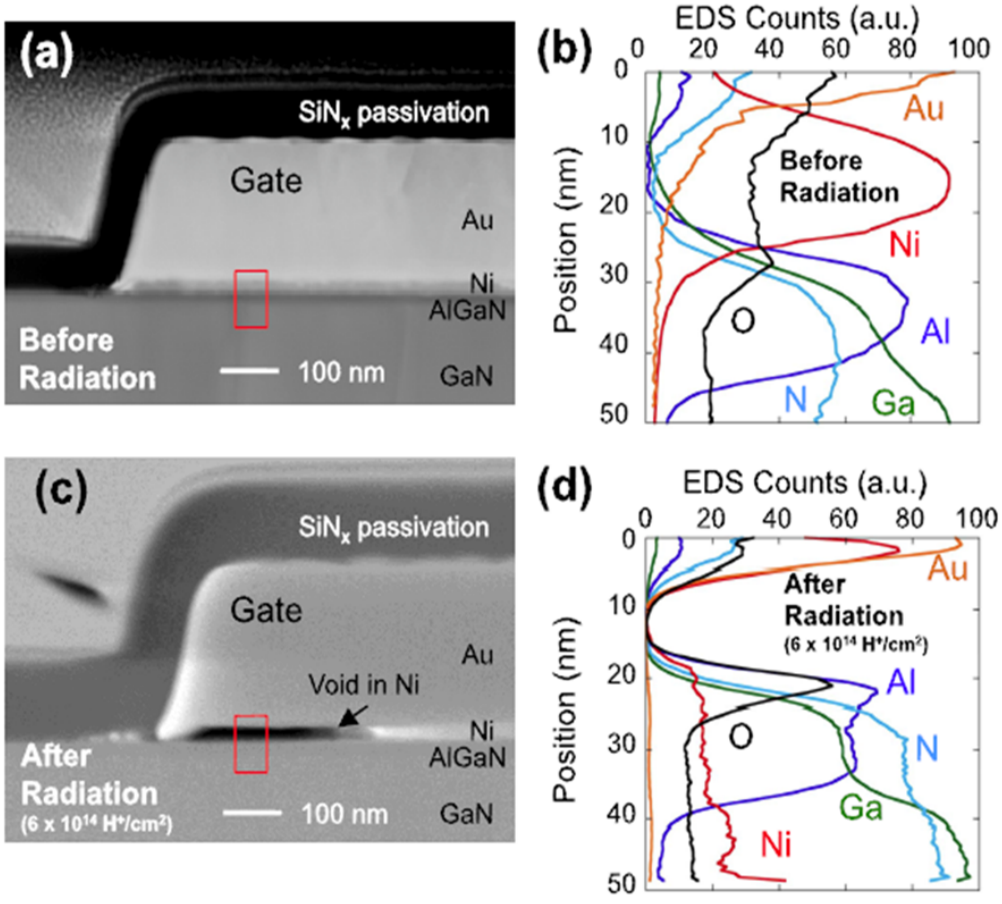

Figure 30. STEM images and EDS line scans of fresh device (a, b) compared to proton irradiated device (c, d) with Ni voiding, from [27].

STEM lamella were removed from samples before and after radiation as shown in Figure 30, where a visual Ni edge void appeared after radiation that is confirmed with the EDS line scans. EDS analysis was conducted in the gate foot area of concern in order to have an elemental map of the structure to compare before and after irradiation, also shown in Figure 30. The EDS area-of-analysis is denoted with the red rectangle seen in (a) and (c), while the *y*-axis in (b) and (d) correlate to the depth of the rectangle. There is clearly Ni voiding as the line scan peak moves from a depth of 15.0 nm to 3.0 nm. There is also a thin layer of amorphous Al oxide which is mostly crystalline before irradiation and then displays a peak of oxygen after irradiation at a depth of 20.0 nm in the analysis box. This finding created a need for further SEM/FIB gate stripping analysis in order to make statistically significant statements about these voids, their size, density, and location.

B. ANALYSIS OF THE 2DEG INTERFACE

In order to analyze the integrity of the 2DEG interface, TEM samples were prepared in Berkeley and analyzed at LBNL and the Ernst Ruska Center (ERC) in Juelich, Germany using atomic resolution STEM. Fresh and proton irradiated samples, which have a degraded AlGaN/GaN interface after irradiation, are shown in Figure 31.

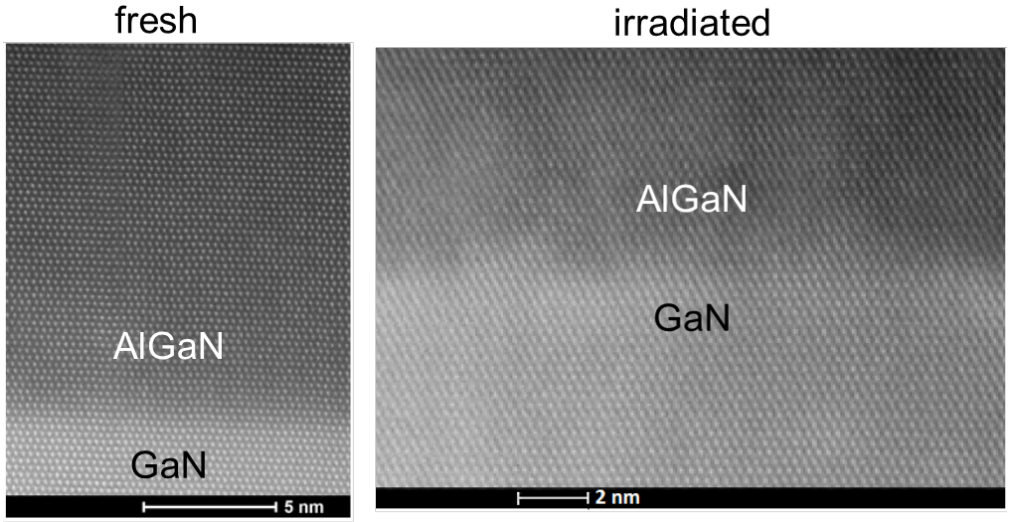

Figure 31. STEM images of AlGaN/GaN interfaces taken at ERC, Juelich, Germany, courtesy of M. Luysberg, P.Specht.

While degradation in the AlGaN/GaN interface roughness is shown in these images, this equipment does not have the contrast sensitivity to identify the elements via EDS.

EDS analysis in atomic resolution had to be conducted at the ERC in Juelich, Germany due to lack of availability at NCEM. Some of the STEM images used in this thesis were also obtained there; in such cases the source is cited in the figure captions. The top Ni/AlGaN interface is seen in Figure 32. Each "dot" seen is a projection of Ga rows. An aluminum oxide amorphous layer was formed after proton irradiation as shown in the image, which significantly changes the interface of the Ni and AlGaN and contributes to the observed changes in gate current.

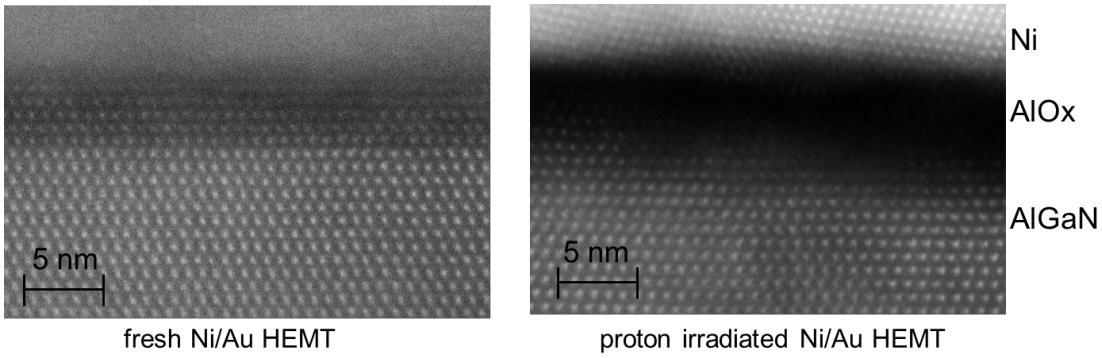

Figure 32. AlGaN/GaN interface with HRTEM from ERC, Germany, courtesy of M. Luysberg, P. Specht.

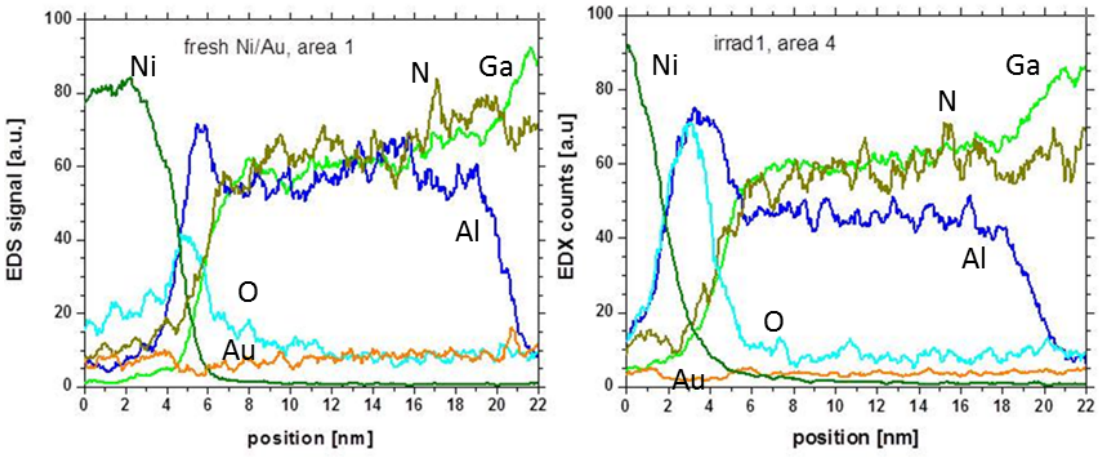

Figure 33. HR EDS line scans at 2DEG interface, data taken at ERC, Germany, courtesy of M. Luysberg, P. Specht.

An increase in the O levels in the top Ga-deprived AlGaN, as well as a general widening of the resulting Al oxide surface sheet, is shown in the EDS line scan analysis of these atomic level resolution images seen in Figure 33. An interesting side effect is the reproducible enhancement of Al (peak) in the oxidized region. At the other side of the AlGaN layer, the AlGaN/GaN interface (20.0 nm position) clearly is less steep after proton irradiation, which has major consequences for the electrical properties of the irradiated device in the form of a degradation of the 2DEG.

C. SEM INVESTIGATION OF NICKEL DEVICES

Ni/Au gated devices exhibited degradation seen in Table 6 of Chapter II and warranted further investigation focused on the Ni with the SEM/FIB. Samples of "fresh" devices and proton irradiated devices were obtained from NRL. As discussed in Chapter III, the depth required to view the Ni was determined through trials to be approximately 80.0 nm, with minor variations, dependent on the type of gate material and its degree of degradation (fresh versus irradiated).

1. Fresh Devices

A typical sample to be FIB stripped can be seen in Figure 34, where the Si_3N_4 and Au have been removed. It is seen that the Ni layer is present and without any type of void degradation. The area of Ni deposition is slightly smaller than those of the covering Au area due to the formation of an additional Au "foot" area on both sides of the gate finger, which can be referenced in Figure 30. Additional fresh samples were stripped as provided in Figure 35 (near the gate finger root of a device) which also have no presence of voiding as seen with most of the fresh samples. There is a noticeable difference between these two images in Figures 34 and 35 in terms of resolution, brightness and contrast. That is because one is taken via I-beam at a magnification of 5,000, and the other is via E-beam with a magnification of 6,500. The variations in this case are simply used a demonstration of the capabilities of the microscopy equipment used in this thesis.

There were two fresh samples in which edge voiding was discovered, as seen in Figure 36.

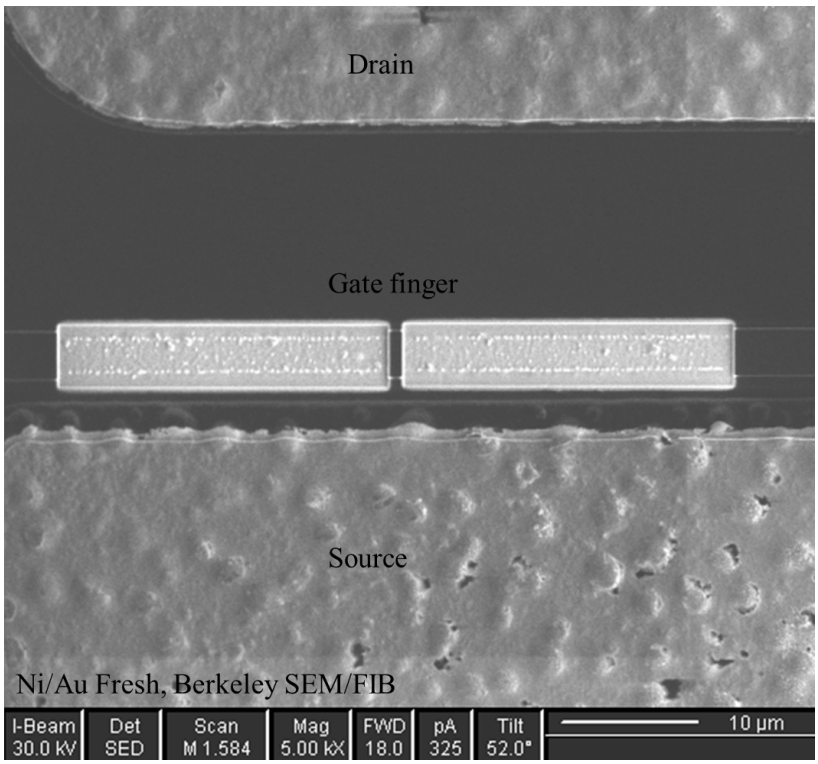

Figure 34. A Ni/Au gated GaN HEMT stripped in two locations of the gate finger reveals that Ni is present and without void degradation.

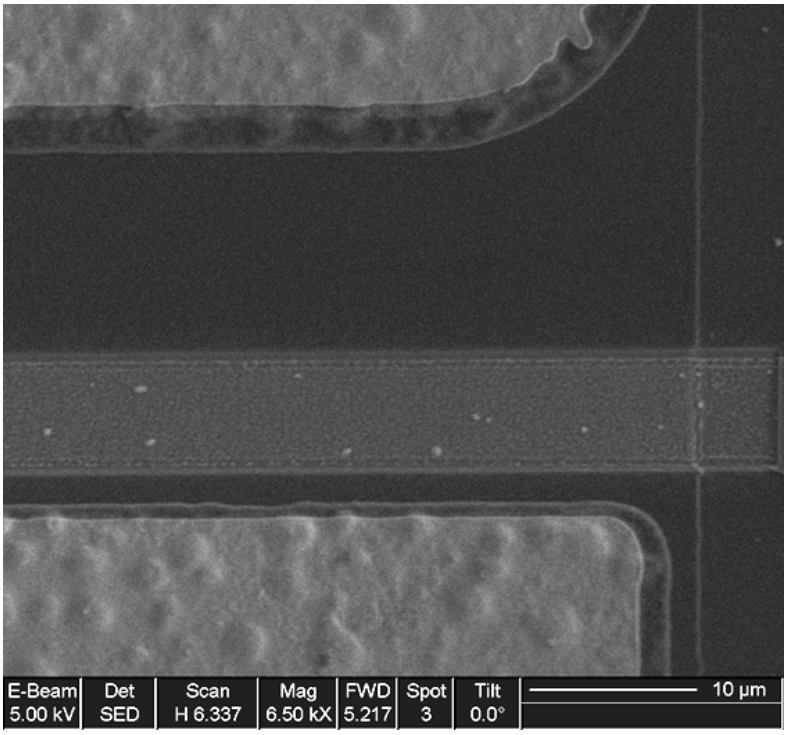

Figure 35. Fresh sample near the root of the gate finger displays no voiding.

This edge voiding only occurs on the source side of the gate finger, and there is no evidence of defects before stripping this gate finger. This fresh device edge voiding was reproducible and seen at both LBNL and NRL. Defects such as this, which occur in both the Ni and Au layer, are due to defective masking and are neglected in the analysis of proton irradiation degradation calculations.

Despite the neglect for the radiation study, it is important to correct this processing issue. One theory on the edge voiding is that the effectiveness of the PECVD or E-beam deposition and lift off processes for the ohmic contacts and gate can be hindered by the close proximity of the HEMT source to the gate finger. The angle of the manufacturing nozzle can produce this effect as well if it is not orthogonal at all times in relation to the part being produced.

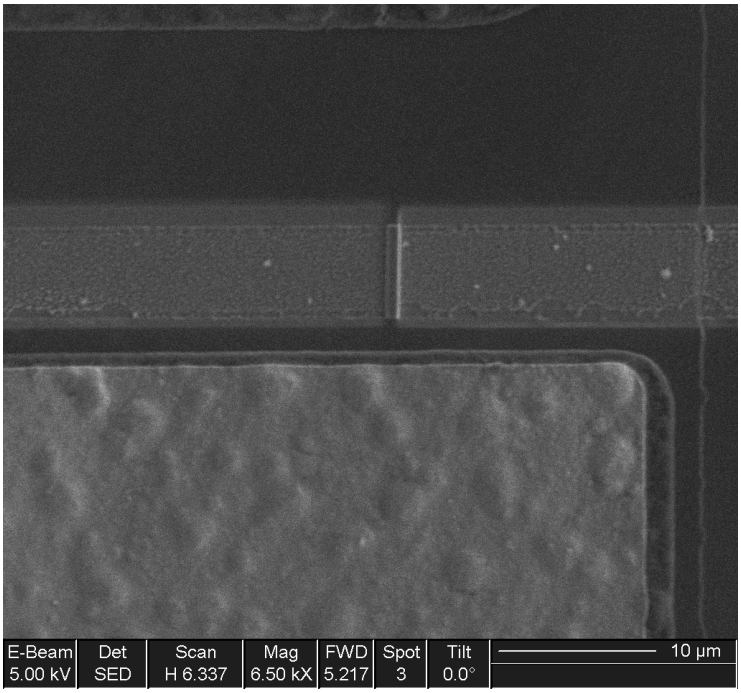

Figure 36. The first fresh Ni/Au gated device to display edge voiding.

A more likely cause is that the E-beam deposited Ni may experience diffusion issues with the PECVD process at 300 degrees Celsius for the Si_3N_4 [35]. There can also be a shadowing effect of the raised ohmic contact. Shadowing issues have been noted in vapor deposition processes before, which has led to a new device patent in June of 2015

[36]. It is expected that the shadowing-effect is more constant for each metal. After consulting with NRL, the main cause is still unclear, but experiments have been drafted to change the sequence of the manufacturing process in order to deposit the gate material after the Si_3N_4.

2. Proton Irradiated

From the 2.0 MeV proton irradiated Ni/Au sample, the STEM images showed a void, but it was important to also obtain EDS data to confirm that the voided regions were in fact voids and not an amorphous region which may also appear in dark contrast. A comparison of fresh versus irradiated STEM/EDS analysis was conducted.

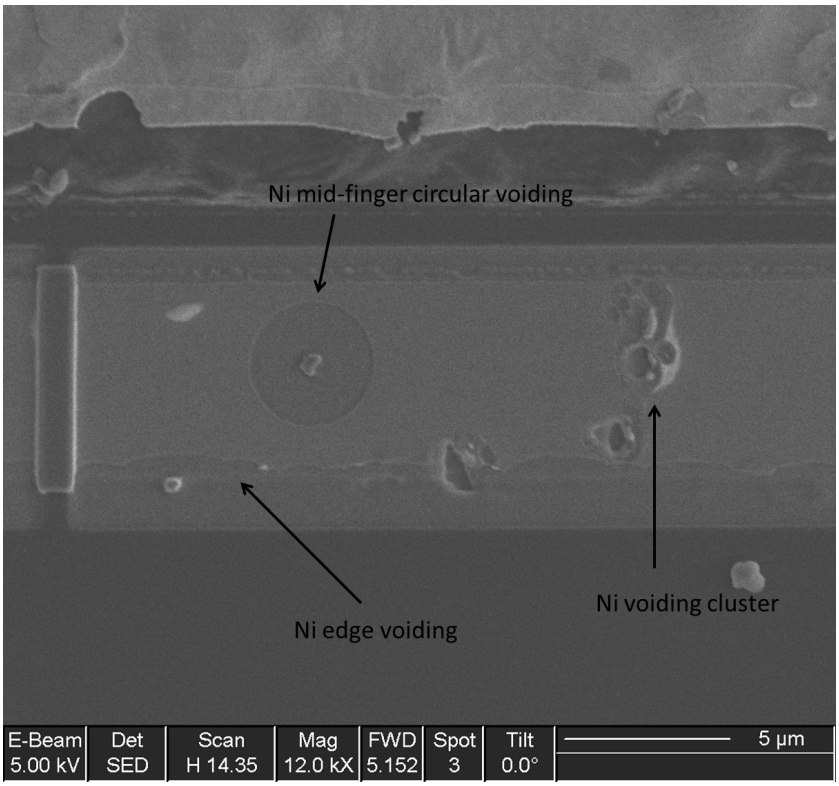

Figure 37. Types of Ni voiding found below the Si_3N_4 and Au layers.

The sample also had multiple gate finger Si_3N_4 and Au layers removed via FIB at LBNL. The stripping of the Ni/Au gated devices revealed several Ni voiding types: edge, circular, and clustering across the finger as revealed in Figure 37 and Figure 38. The edge

voids found in the irradiated samples are dominant on the drain side of the gate finger with a jagged appearance. The edge voiding, also discovered in some fresh samples, appears to be process induced; however, this defect is enhanced with proton irradiation, which leads to the theory that the voids are "fed" vacancies for diffusion from the passivation layer. Circular voids are also found on the edge occasionally, as seen in Figure 38, on the source side with a distinct radius vice rough edge.

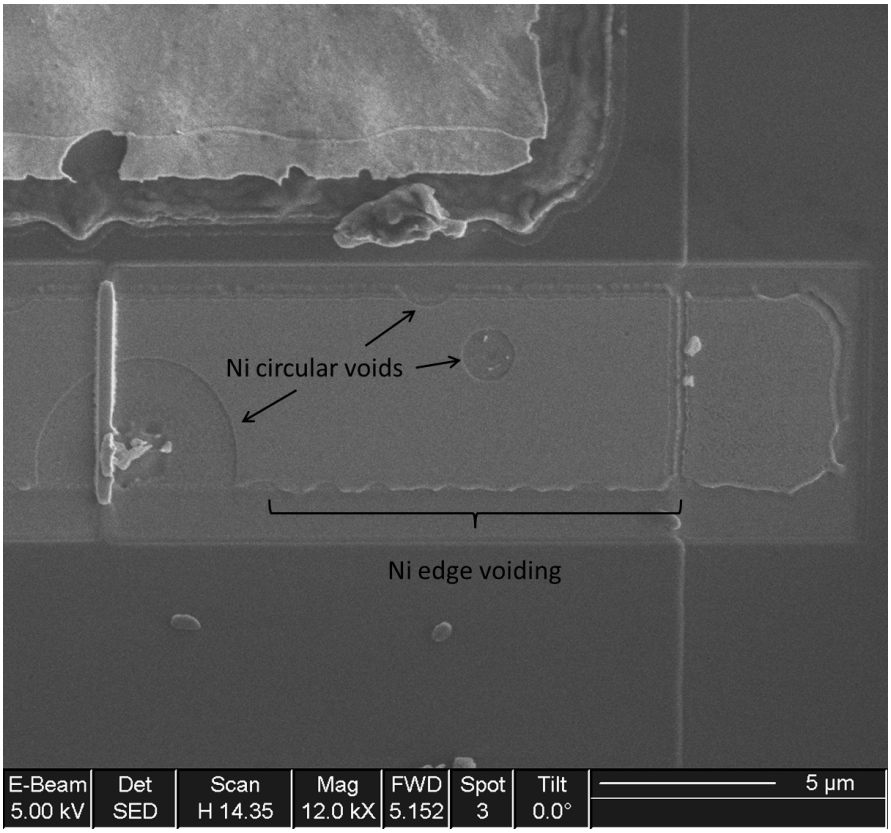

Figure 38. FIB stripped gate finger reveals edge and circular Ni voiding.

Voiding is also observed at the boundary of the material as seen in Figure 39, where the Ni is absent directly at the boundary and also clustered voids appear near the root of the gate. This boundary created during construction has only the buffer layers nearest to the gate, and the finger has the additional AlGaN/GaN layers required for functionality. The boundary voiding is seen in an extreme form in Figure 40 where 10.0 microns on either side of the boundary is void of Ni. These mesa isolation edge boundary

defects likely occur due to an approximate 100.0 nm height difference. Defects that do not exhibit a radial pattern are neglected for proton irradiation degradation calculations. Again, the importance of process defects and their correction remains. This damage can be caused by the PECVD process, and NRL has noted some experimental changes to conduct.

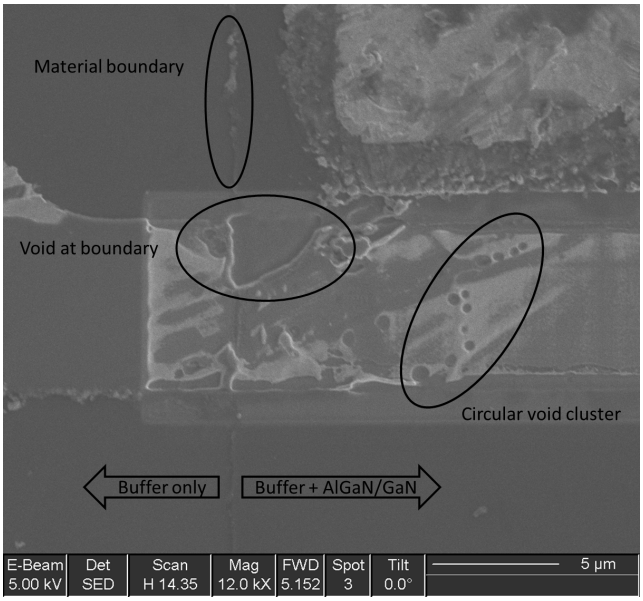

Figure 39. HEMT gate finger root is FIB stripped revealing Ni void issue at the boundary where AlGaN/GaN does not cover left side.

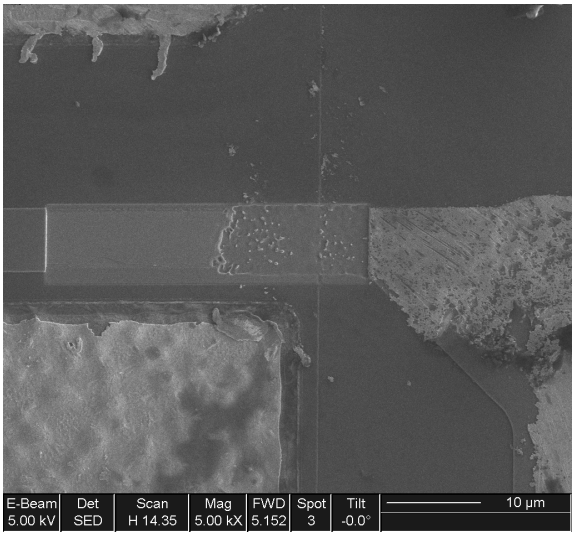

Figure 40. FIB stripping reveals a Ni void at the boundary of Si_3N_4 layering.

D. PLATINUM DEVICES

NRL also produced, measured, and proton irradiated Pt/Au gated devices for gate material comparison. These devices and all tests conducted on them are identical to the Ni/Au gated devices. The only difference is the 20.0 nm Pt electrolyte underneath the Au in place of Ni.

1. Characteristics

The Pt/Au gated devices were characterized at NRL, where the data collected is presented in Table 7. The mobility and sheet carrier density both decreased after proton irradiation, while the sheet resistance increased. These findings are similar to the Ni/Au samples but to a lesser extent, making the Pt/Au samples the better device structure for this radiation environment.

Table 7. Pt/Au gated NRL device parameters.

Parameter	Units	Before Radiation	Dose $6.0\times10^{14}cm^{-2}$	Percent Change
μ_{2DEG}	$cm^2/(V*s)$	1525	1187	−22.16
n_{2DEG}	$10^{12}cm^{-2}$	6.26×10^{12}	5.50×10^{12}	−12.14
R_{SH}	$\Omega/\square$	629	956	51.99

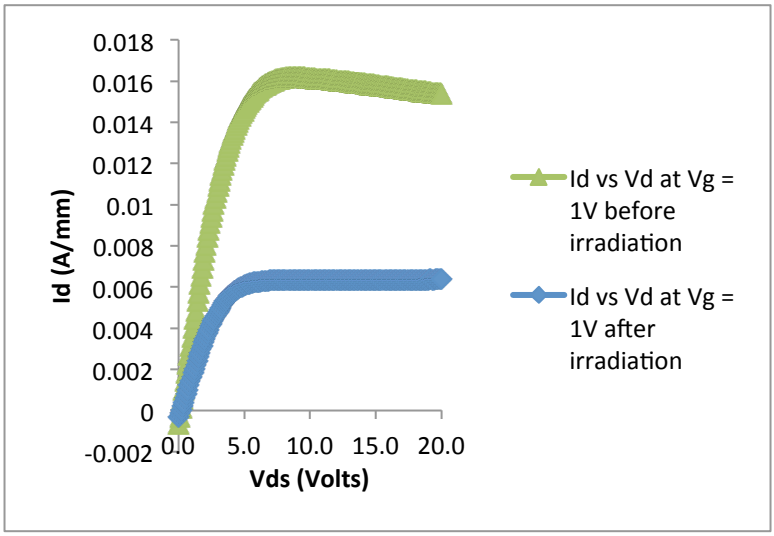

Figure 41. Pt/Au gated HEMT before and after proton irradiation decreases drain current versus drain voltage.

The Pt samples performed seven percent better than the Ni in terms of mobility and two percent better for carrier density while demonstrating a 12 percent better sheet resistance than the Ni. This is an expected result as the material properties such as thermal expansion and diffusion of Pt and Au are more similar than those of Ni and Au. A simple reference to the periodic table confirms that Pt and Au are neighboring elements.

The Pt/Au samples were also measured for I-V curves, as seen in Figure 41 and Figure 42, where the drain current is compared to the drain voltage and gate voltage, respectively. Each plot indicates a decrease in drain current after proton irradiation much like the Ni/Au samples.

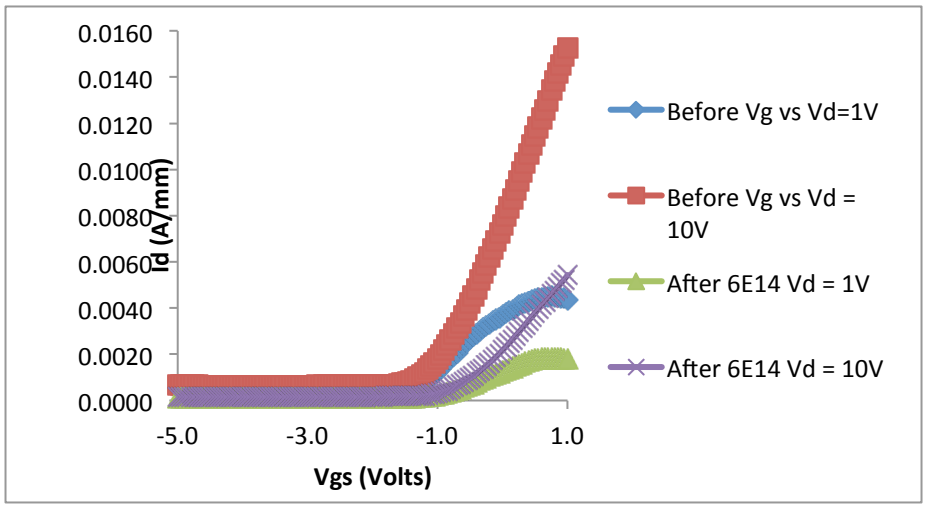

Figure 42. Pt/Au gated HEMT before and after proton irradiation decreases drain current versus gate voltage.

2. Fresh Devices

The Pt/Au devices were FIB stripped in the same fashion as the previous Ni/Au samples as seen in Figure 43 and Figure 44 where there is no presence of Pt voiding even near the root of the gate. This is an interesting finding because these devices are processed in the same manner as the Ni/Au devices, yet there is no edge voiding due to the process. This means that the temperature of the PECVD process does not affect the Pt as it does the Ni.

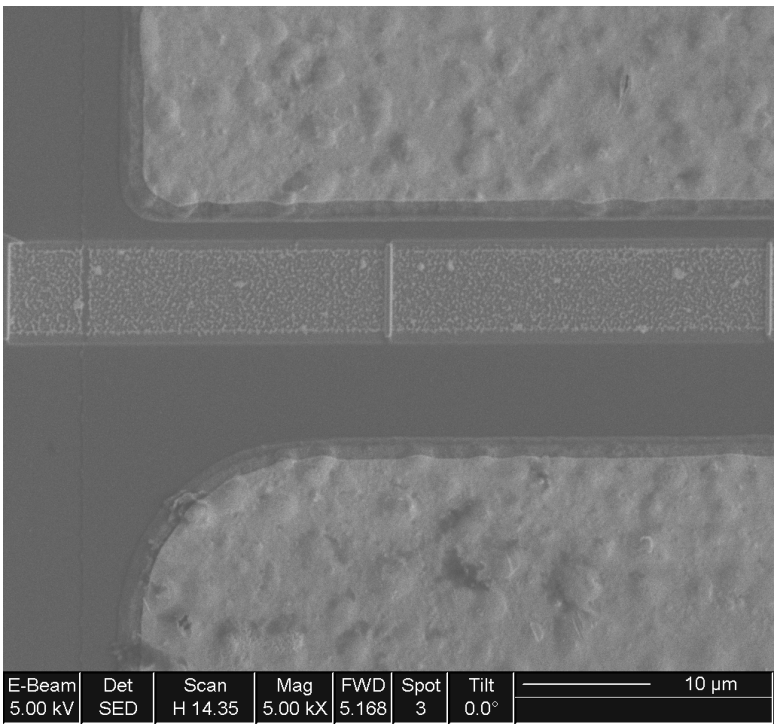

Figure 43. E-beam image of fresh Pt/Au HEMT displays no voiding.

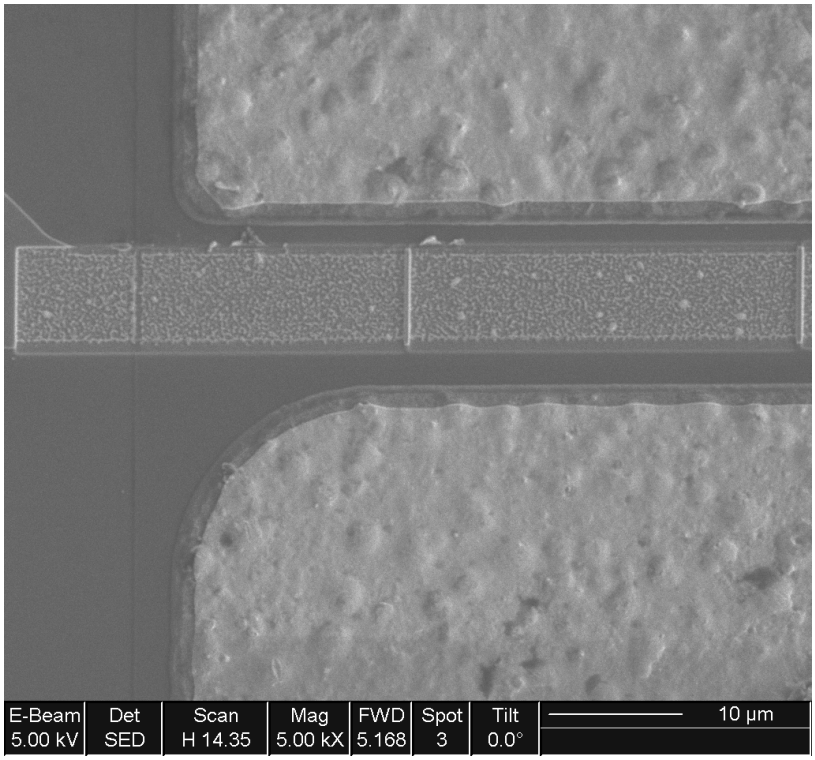

Figure 44. Pt/Au gated device with closer drain-to-gate finger layout is FIB stripped to reveal no voiding near the root.

3. Irradiated Devices

The irradiated Pt/Au gated HEMTs were stripped similarly to the Ni/Au samples and also displayed voiding, this time in the Pt as shown in Figure 45 where five mid-finger circular voids can be seen, which are more concentrated near the gate root, much like the Ni samples.

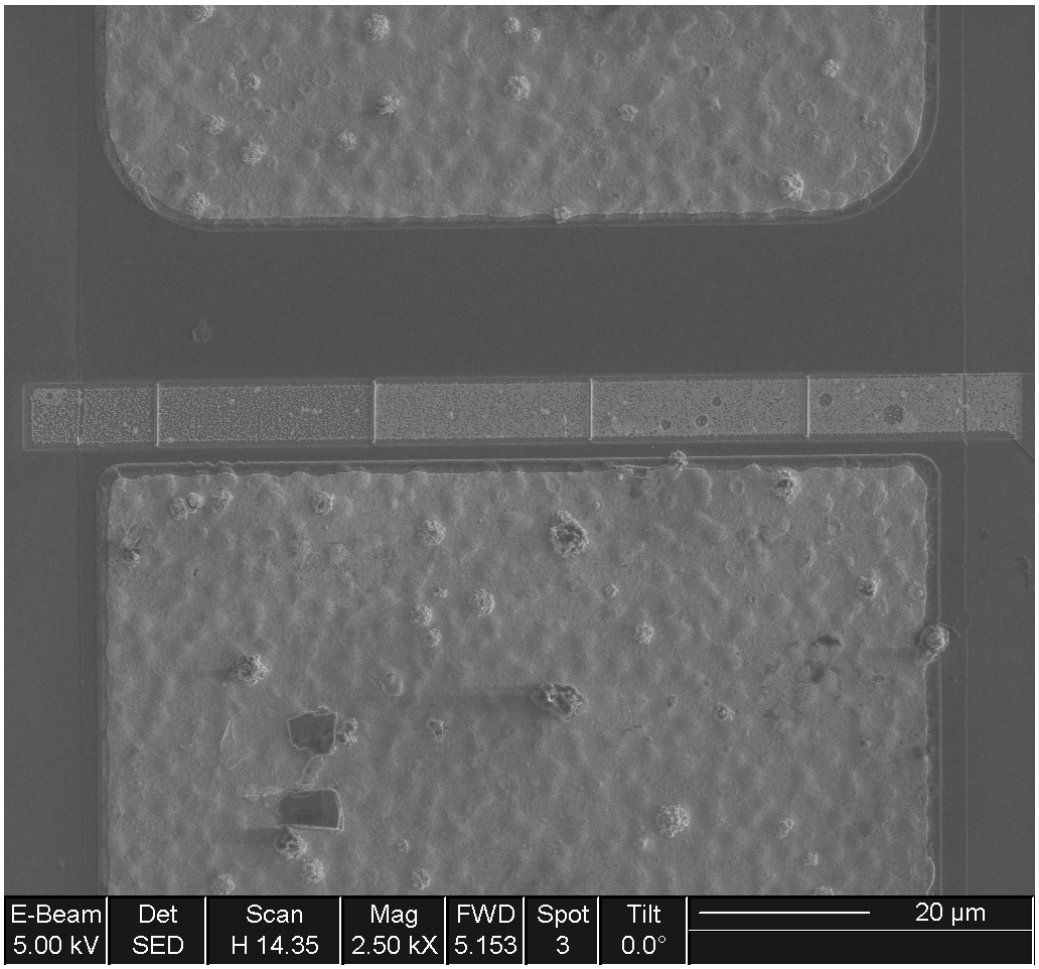

Figure 45. FIB stripped Pt/Au gated sample.

As mentioned in Chapter III, the I-beam is also used for imaging to ensure that the FIB strips material in the desired location as seen in Figure 46, where the previous figure is magnified. FIB stripping continued for nine Pt/Au gated samples, and some interesting Pt voiding was discovered as shown in Figure 47, in which more than a dozen small circular mid-voids appear to be in a line.

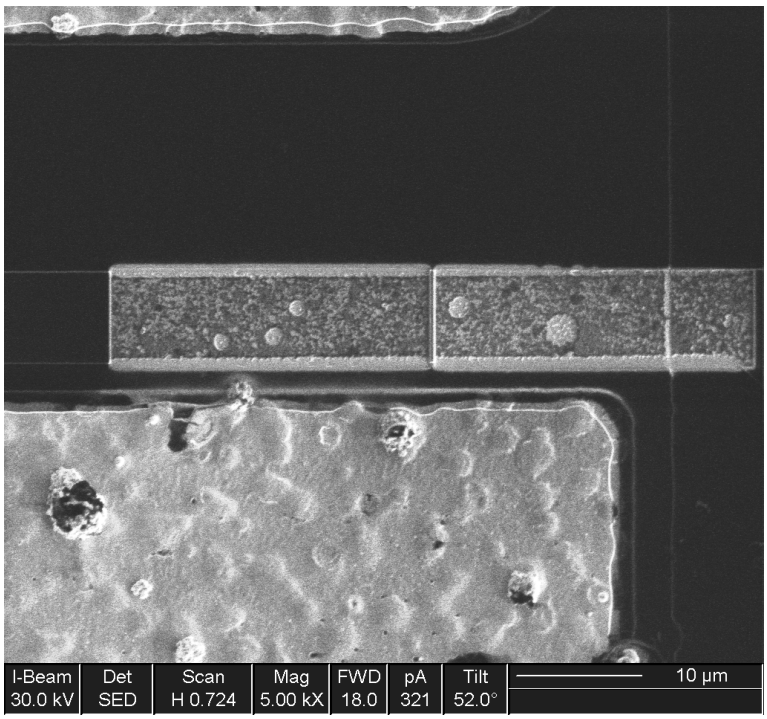

Figure 46. I-beam image of FIB stripped Pt/Au gated HEMT reveals large circular mid-finger voids.

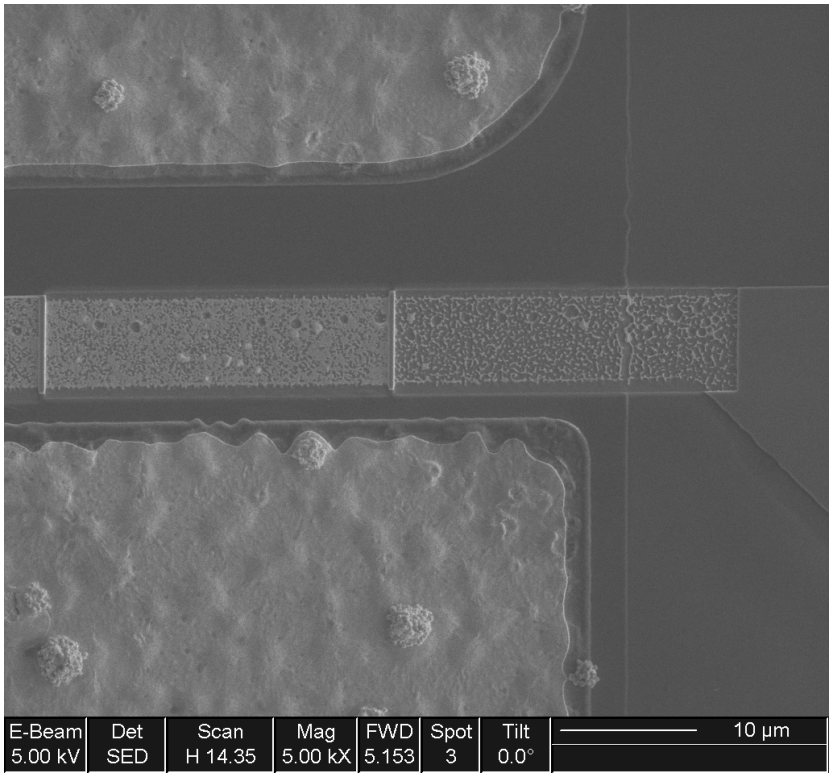

Figure 47. FIB stripped Pt/Au gated HEMT displays a line of circular voids.

Most of the gate fingers that are FIB stripped for analysis are 7.0 microns in length; however, other gate length samples are found on this sample as seen in Figure 48, where a 3.0 micron gate finger displays many mid-finger voids. The voids are larger and more concentrated near the root of the gate finger. It is uncertain if this effect is a consequence of the difference in gate length or simply a random occurrence.

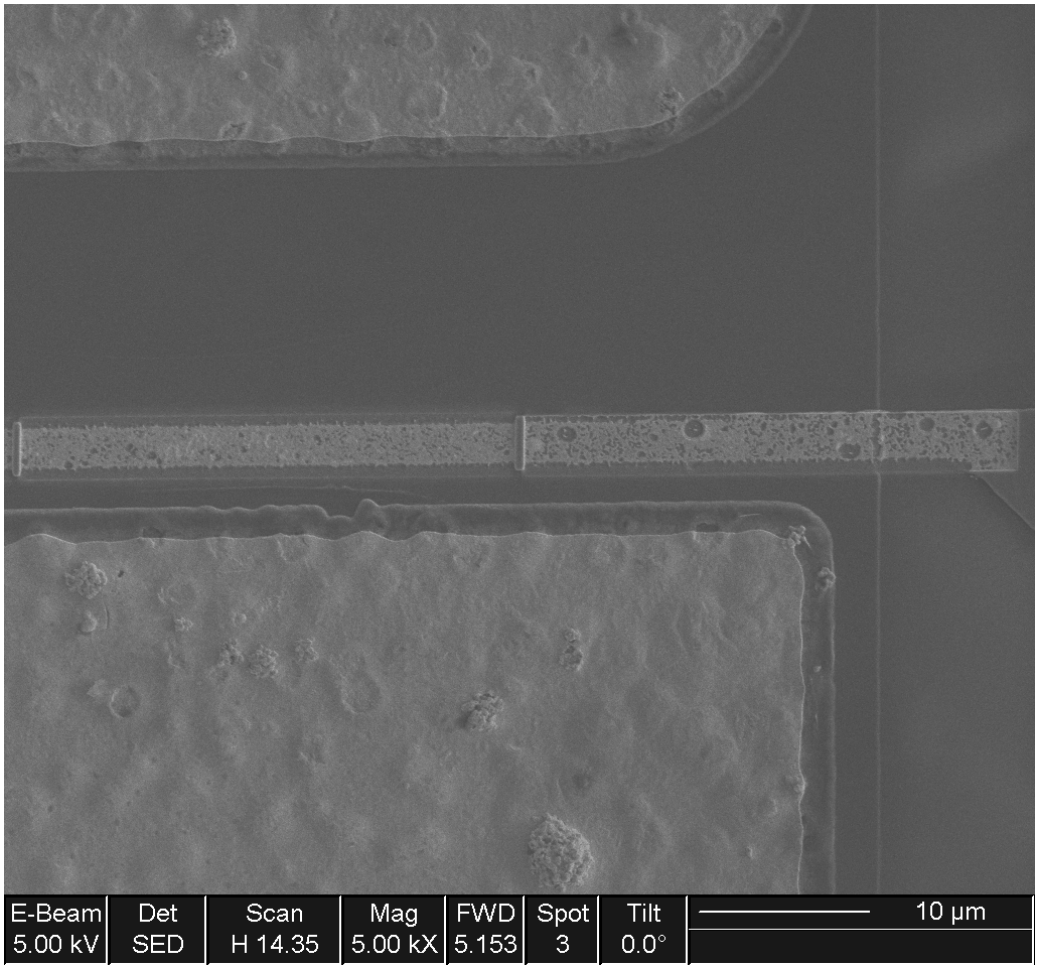

Figure 48. FIB stripped Pt/Au gated HEMT with 3.0 nm gate finger length reveals mid-finger circular voids.

A different type of defect (compared to Ni) was found in one Pt sample where the same FIB stripping depth revealed an additional region of Au, as seen in Figure 49. This is unlike any other defect discovered and was potentially caused by the manufacturing process where the Au gate material is deposited via E-beam and lift off. Again, such

manufacturing are excluded from proton irradiation degradation calculations and statements.

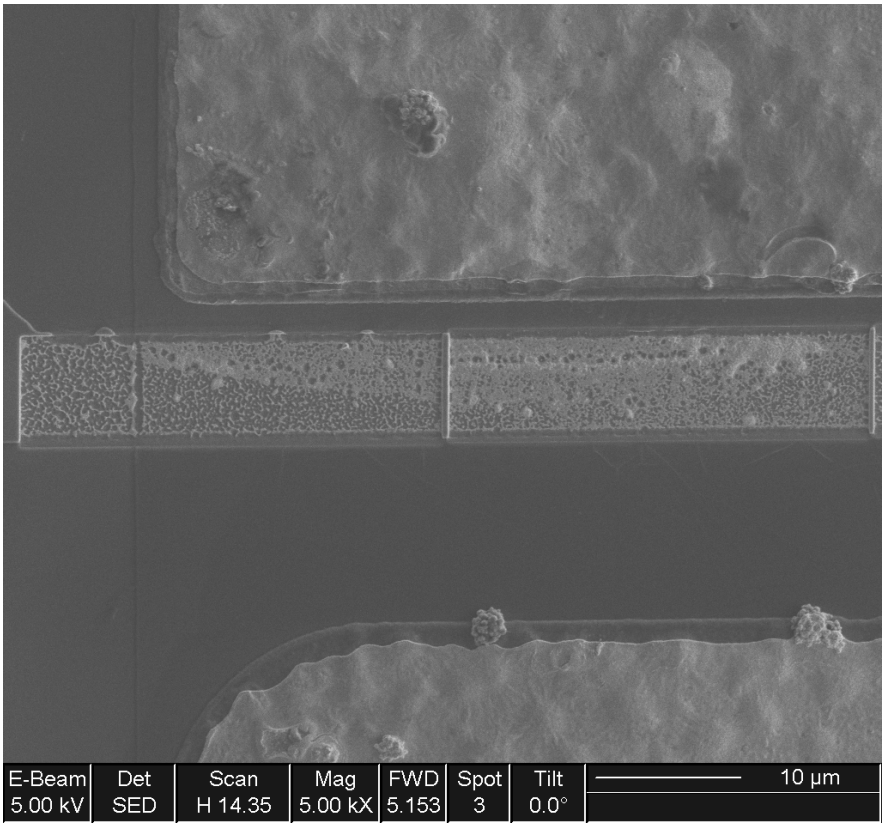

Figure 49. Pt/Au gated HEMT has unusual, residual Au.

E. VARYING RADIATION FLUENCE DEVICES

A second set of NRL samples with the same device structure were proton irradiated at 2.0 MeV for various fluences similarly to the first set of samples, but this time a sample was removed after each fluence of radiation. With these samples, the goal was to strip the gate fingers and compare the size of the voids with those of the 6.0×10^{14} H^+ cm^{-2} sample. The first sample selected for comparison was 1.0×10^{14} H^+ cm^{-2} due to the C-V plot reference, which has a decrease at this level. Unfortunately, when attempting to load this sample for FIB stripping, the sample built up an electric charge in the Ion mode as seen in Figure 50. On an area away from the HEMTs, we see that after ten seconds in I-mode, the lack of visibility prevents working on the samples. Figure 51

is an E-mode image to confirm that no ion damage occurred while in I-mode and that it was only a charge build-up.

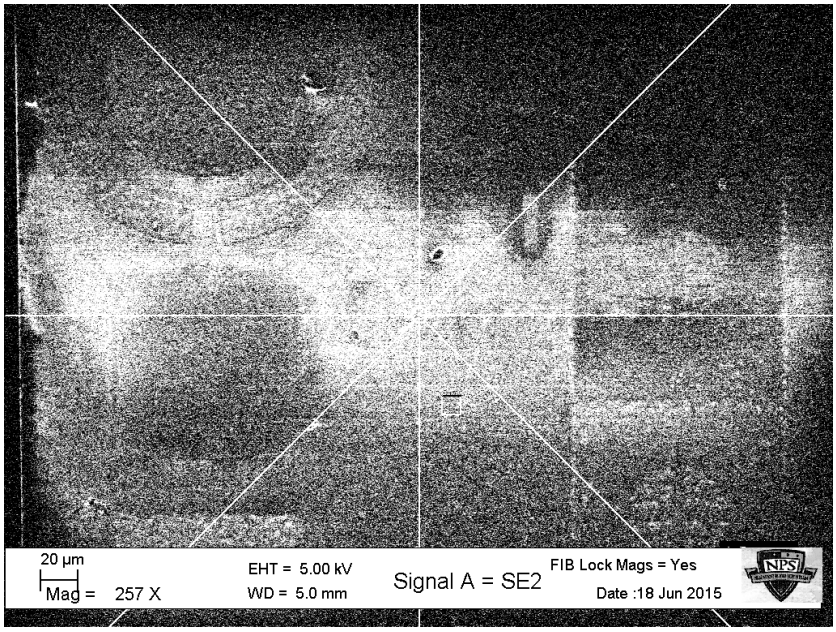

Figure 50. Ten seconds into I-mode, the charge builds up and prevents accurately using FIB due to visibility.

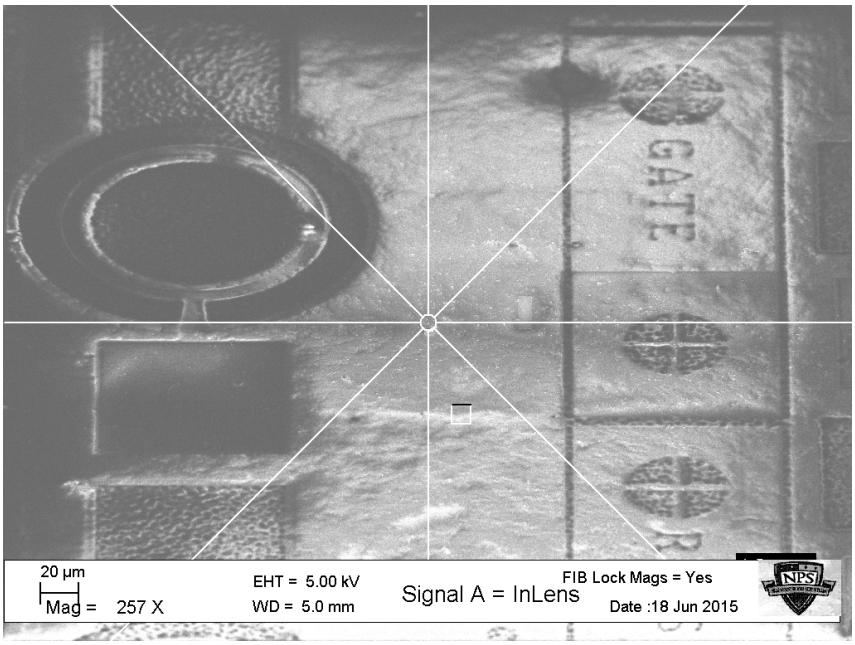

Figure 51. E-mode view of sample after I-mode charge build up confirms that this was a charge build-up and that no ion damage occurred.

After the charge build up occurred, the sample was removed from the SEM and air dusted to remove contaminants. Additionally, corner painting of colloidal silver paint was tried to attempt grounding the charge to the pedestal. This experiment failed, as did various variations of sample grounding using Pt deposition.

During the FIB stripping trials, we noted that these samples contained a different surface layer thickness which, after contacting NRL, was identified as residual photoresist remaining after photolithography processing. Plasma cleaning does not remove this layer, but cleaning the surface with acetone followed by a methanol cleanly removed the photoresist. Once this hurdle was overcome, the samples were FIB stripped as usual.

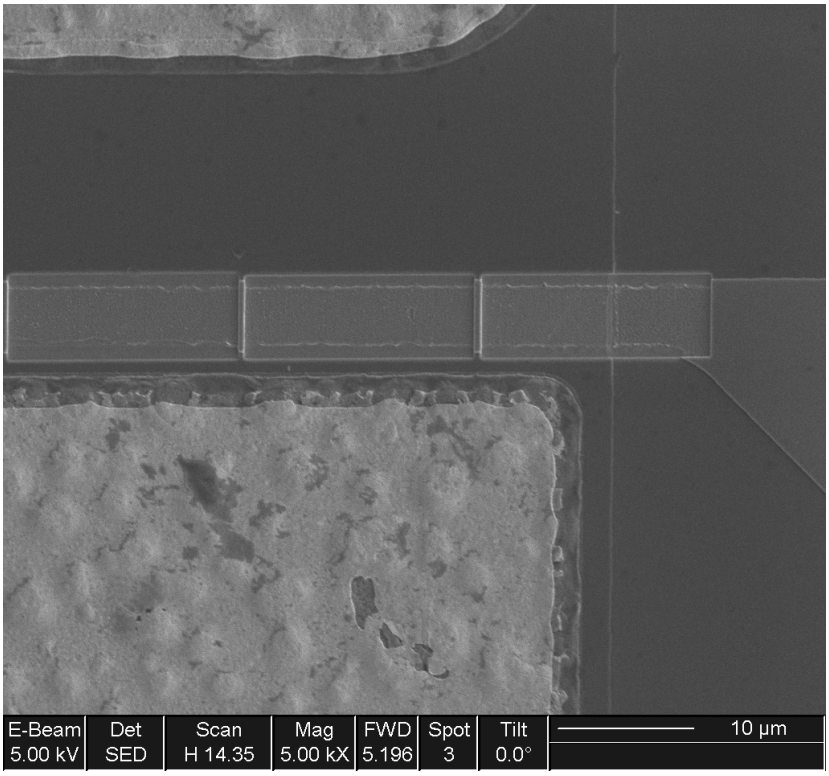

Figure 52. Lower fluence of edge and one small mid-finger void starting.

The lowest radiation fluence sample available for stripping occurs at 1×10^{12} H^{+} cm^{-2}. In reference to Figure 7 that previously displayed the degradation of parameters with increased fluence, there should not be much degradation at this level of proton

irradiation. This is confirmed by FIB stripping three different devices for this level of fluence as seen in Figure 52, where some edge voiding is present along with one small mid-finger void. All other sections of these three devices only displayed minor edge voiding. Unfortunately, the delay in overcoming the photoresist issue prevented obtaining a larger sample size as well as stripping of the other fluence samples for a more complete analysis.

F. COMPARISON AND VOID RELEVANCE

Four comparisons are made in this section to characterize the respective effects on the voids that were discovered and shown in the various figures throughout the previous three sections. An assessment of fresh versus proton irradiated devices, an evaluation of the different gate materials, the effect of gate length, and, finally, a comparison of radiation fluence are all discussed.

1. Fresh versus Irradiated Ni/Au

A comparison of fresh and proton irradiated GaN HEMT gate fingers was published from this research as seen in Figure 53, where edge Ni voiding occurred.

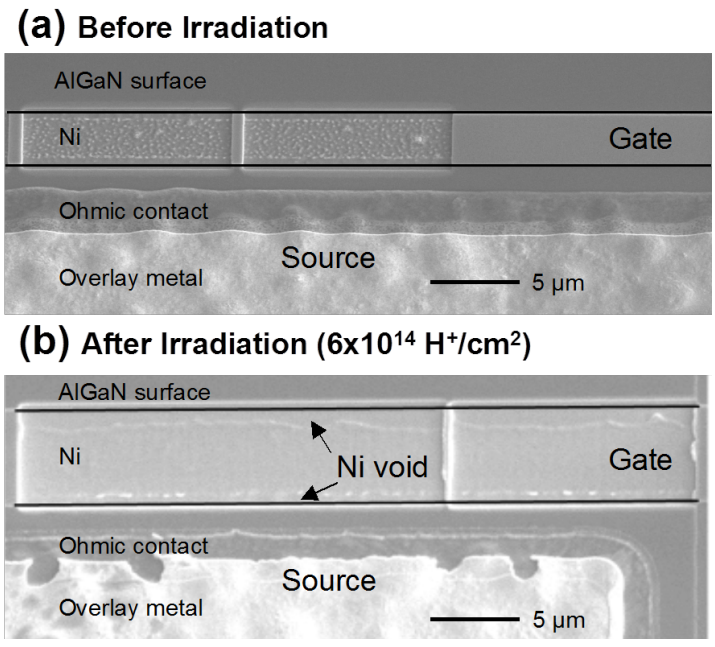

Figure 53. Fresh versus irradiated gate of electrode with Ni void, from [27].

In Figure 53, the top gate finger is three micron while the bottom gate is seven micron.

Voiding in the gate metal contributes toward the overall degradation of device performance by reducing the effective gate area. Using an image processing software called ImageJ, we can calculate the area reduction where the Ni voiding occurs. The software has been used in other applications such as calculating the effective photosynthesis process ability of a leaf. In such an application, a converted black and white image of the dead parts of the leaf or holes have a different contrast than the live parts of the leaf which can still produce oxygen. The user applies ImageJ or similar software to calculate the area reduction of the leaf. This thought process was applied to the Ni voiding seen in the gate finger. Illustrated in Figure 54, the SEM image was converted to 8-bit-black-and-white and then outlined to depict the useful gate area, which was used to calculate area reduction for this sample. For this particular sample, a reduction of 26 percent was calculated for the gate area.

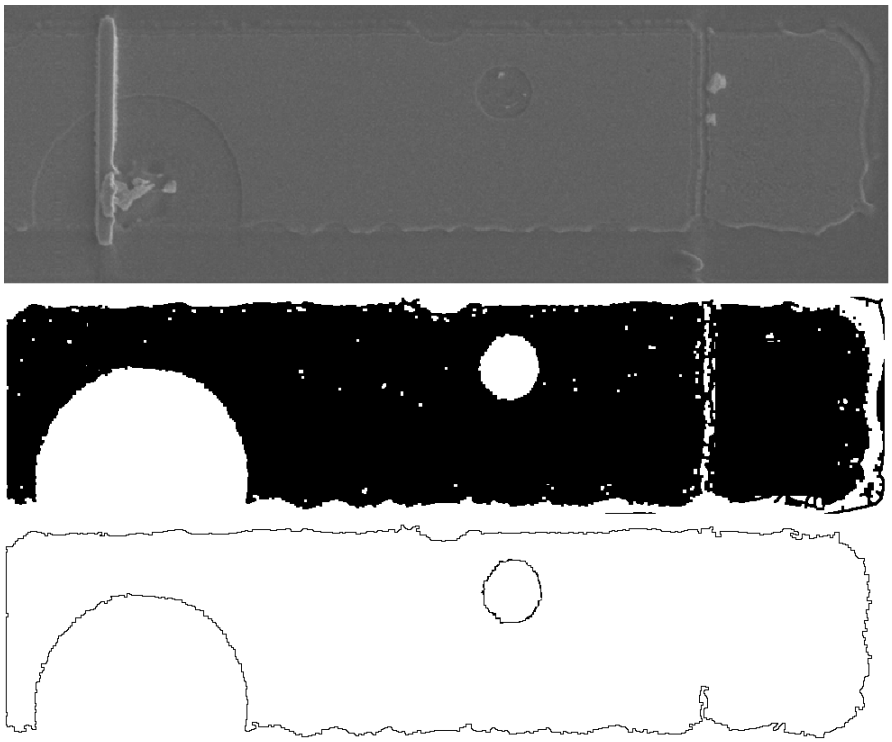

Figure 54. ImageJ software utilized to convert an SEM image to 8-bit-black-and-white and then calculate area of voiding.

The importance of the reduction in gate area is seen when calculating the capacitance, which was studied in detail specifically for GaN/AlGaN HEMT modeling purposes in [37] by Xin-Hua. In this research, after assuming no impurity charge in the substrate, the capacitance per unit area [37]

$$C_s = \frac{dQ_s}{dV_g} = q\frac{dn_s}{dV_g} \tag{8}$$

between the gate and the source is determined, where Q_s is the surface charge between the metal and semiconductor, V_g is gate voltage, q is an elementary charge, and sheet charge density is n_s. There is also a relationship between C_s, n_s, and the thickness of the AlN layer, where a thinner AlGaN layer results in a higher sheet carrier density. A reduction in the surface area leads to a reduction in n_s and a reduction in capacitance as seen by the measurements taken by NRL in Table 6. The reduction in gate area and sheet charge density that cause a reduction in capacitance is seen in Figure 55, provided by NRL [4].

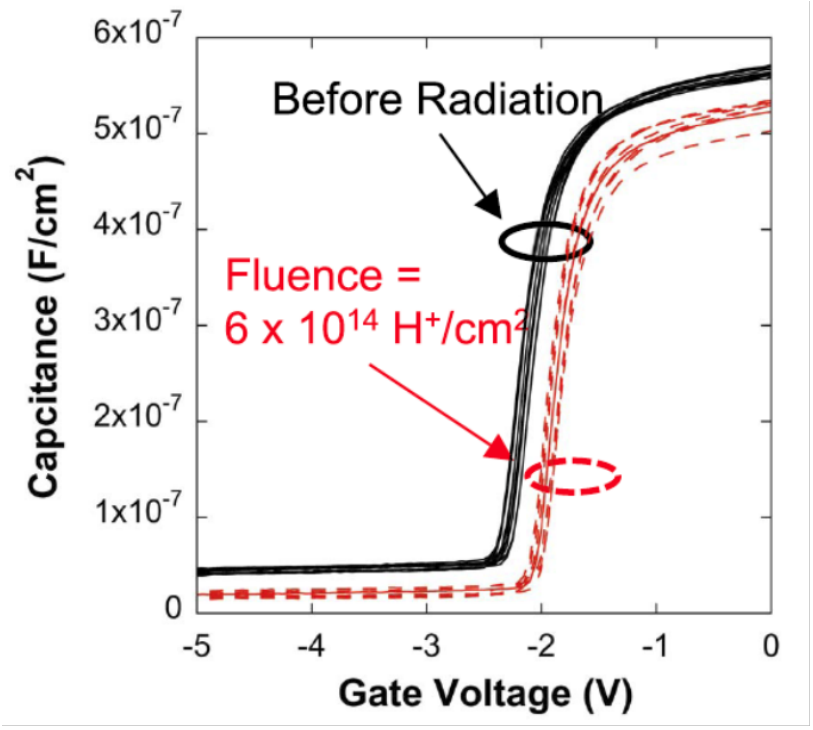

Figure 55. C-V characteristics of multiple NRL Ni/Au Schottky gated HEMTs before and after irradiation, from [4].

The raw C-V data of all HEMTs measured by NRL was obtained in an effort to calculate and correlate each device capacitance before and after irradiation with its measured gate area reduction. Unfortunately, it was discovered that the C-V data before irradiation was not conducted for the devices that were irradiated, but instead the before irradiation data was conducted on another chip sample of the same construction. Due to this, the raw data was used to plot average before and after C-V of 20 devices as seen in Figure 56.

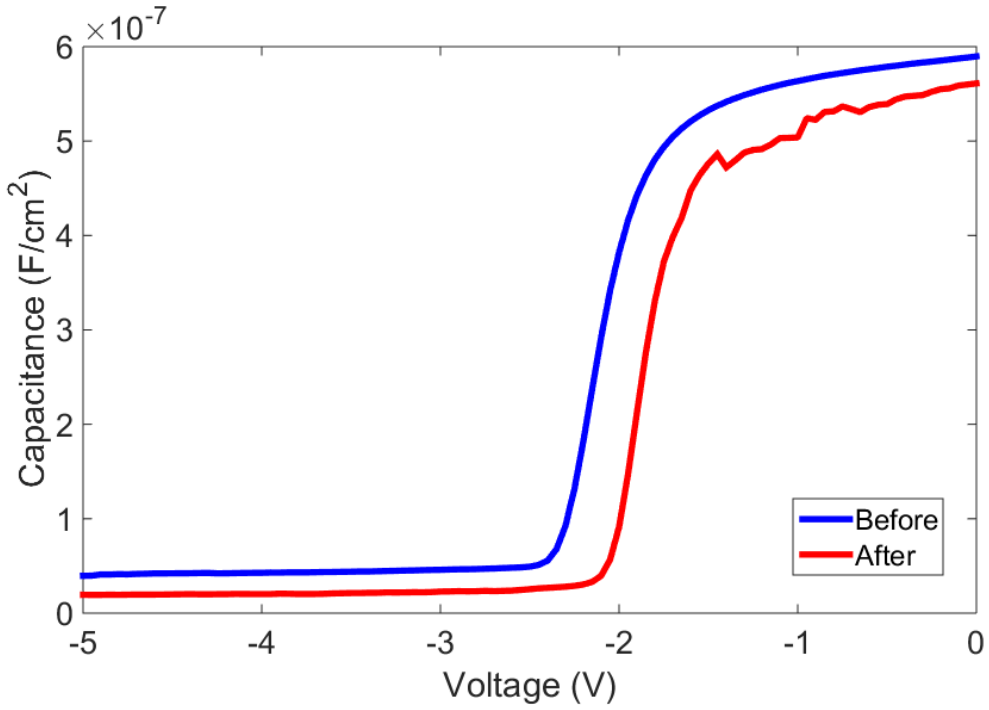

Figure 56. C-V characteristics for the average of 20 GaN HEMT devices before and after proton irradiation.

In Figure 56, we can see that the GaN HEMT is reverse biased with a transient state window from approximately -2.3 V to -1.7 V. At -1.5 V, the devices exhibit a steady-state "on" condition. At the steady-state condition, there is approximately a 10 percent reduction in capacitance after proton irradiation.

The ImageJ gate area reduction calculations for 24 portions of nine different Ni/Au devices yielded an average overall gate finger area reduction of 12.4 percent. This

value was calculated using the average area reduction for individual regions along each 100.0-μm wide gate finger. Each section is 20.0 μm in width for a total of one root, three middle portions, and one tip. The gate fingers used in this average were all 7.0 microns in length; therefore, the total area was 700.0 μm^2. The averages of the individual section area reductions were: 30.9 μm^2 for the root, 14.9 μm^2 for each middle portion, and 11.2 μm^2 for the tip. Summing the five sections and dividing by the total area determines the overall gate finger area reduction. This indicates that voiding is most prominent in the gate root or the first 20.0 μm where a boundary of Si_3N_4 exists; however, the largest Ni void discovered was near the tip. The sample imaged in Figure 57 showed in the largest single Ni/Au circular void analyzed, for a reduction of 18.3 μm^2 even with a portion of its circular shape extending off of the gate finger, which was not included in the value.

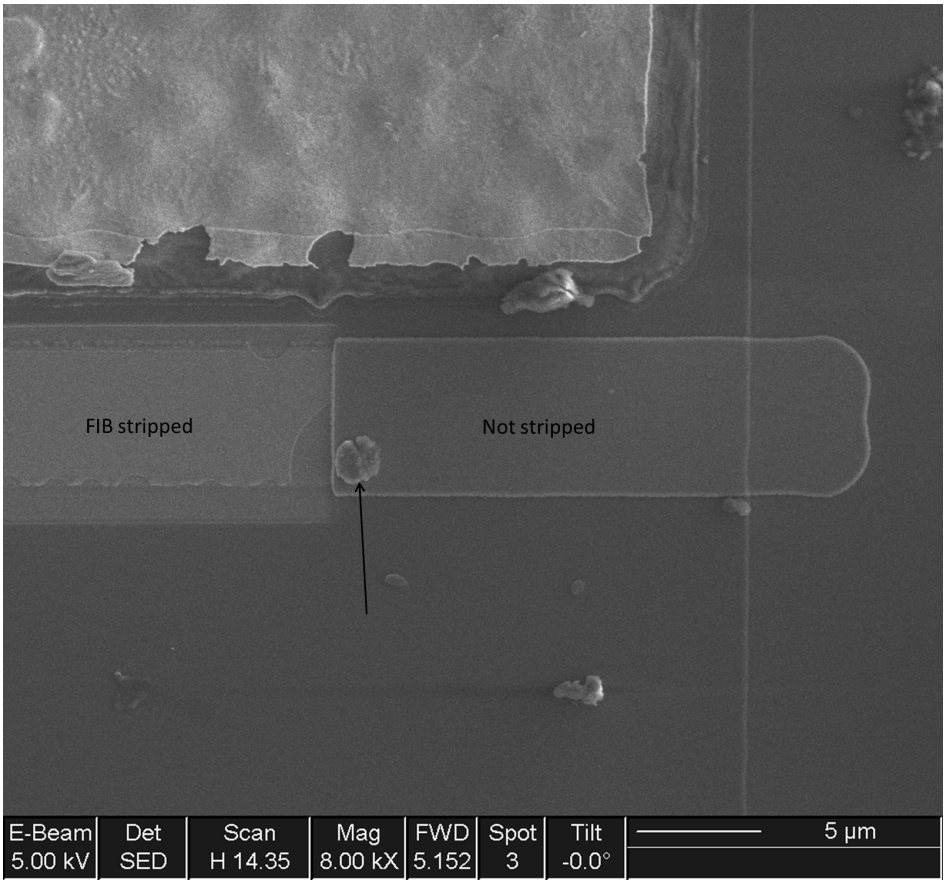

Figure 57. Additional surface material seen before stripping turns out to be the center of the largest Ni void.

Some voids such as the ones discussed above were noted as areas-of-interest due to the additional material located on the surface before any FIB stripping as seen in Figure 57. Since no circular voiding was found before irradiation and this material is at the center of a void, it is possible that the material is a combination of Ni and Au which erupted through the passivation layer. This identification before using the FIB is only visible on very large voids and requires further analysis via STEM to identify the composition of the erupted material.

2. Ni versus Pt Comparison and Gate Length Assessment

In comparison, the Pt/Au device sample size had two different gate lengths, 3.0 μm and 7.0 μm, which contained four and three devices, respectively. These samples were analyzed at a lower magnification (5,000) in the ImageJ processing, which led to fewer images required in order to obtain the entire gate width of 100.0 μm. This required two stripped portions for the gate and two for the tip. The average area reduction for the 3.0-μm gate-length devices is 7.2 μm^2 for both regions. The reduction for the 7.0-μm gate-length devices is 10.1 μm^2 and 5.4 μm^2 for the root and tip, respectively. A comparison of gate material voiding is shown in Table 8, where Ni devices have six times the amount of percent gate area reduction due to voiding as compared to a Pt device with the same 7.0-μm gate length. Both materials display increased voiding closer to the gate with this gate length. In comparing the gate lengths of the Pt devices, the location of the voids is equally seen near the root and tip, but the total percent reduction is doubled in the 3.0-micron micron device.

Table 8. Void area comparison.

Device material / gate length	Root area reduction (μm^2)	Middle area reduction (μm^2)	Tip area reduction (μm^2)	Total average area reduction (%)	Largest void area (μm^2)
Ni w/ 7μm	30.9	14.9	11.2	12.4	18.3
Pt w/ 3μm	7.2	combo	7.2	4.8	1.1
Pt w/ 7μm	10.1	combo	5.4	2.2	6

The largest voids discovered for each type of sample quantify that Ni devices can have voids three times the size of the Pt devices, and while the 3.0 micron gate length samples have smaller voids, they have more voids. The Pt samples also have a less rigid gate finger edge on both sides and displayed very little edge voiding, whereas the Ni samples clearly had edge voiding, which contributed toward the increased area reduction.

3. Radiation-fluence Effects

Determining the full effects of fluence on the HEMT devices required the FIB stripping of all remaining fluence samples; however, the one small mid-finger void that was identified had an area of $0.48\,\mu m^2$. This value can be used in conjunction with the other area calculations at higher fluence in order to present a model that theorizes the void creation. One theory is that threading dislocations of a constant radius throughout the irradiation process collect and transport vacancies to the interface to create these voids. This theory leads to the assumption that the void size increases in size linearly with an increase in radiation fluence. Due to a lack of data at various fluences, a preliminary graph was created, marking two collected points, as seen in Figure 58, where void volume versus proton radiation dose is shown.

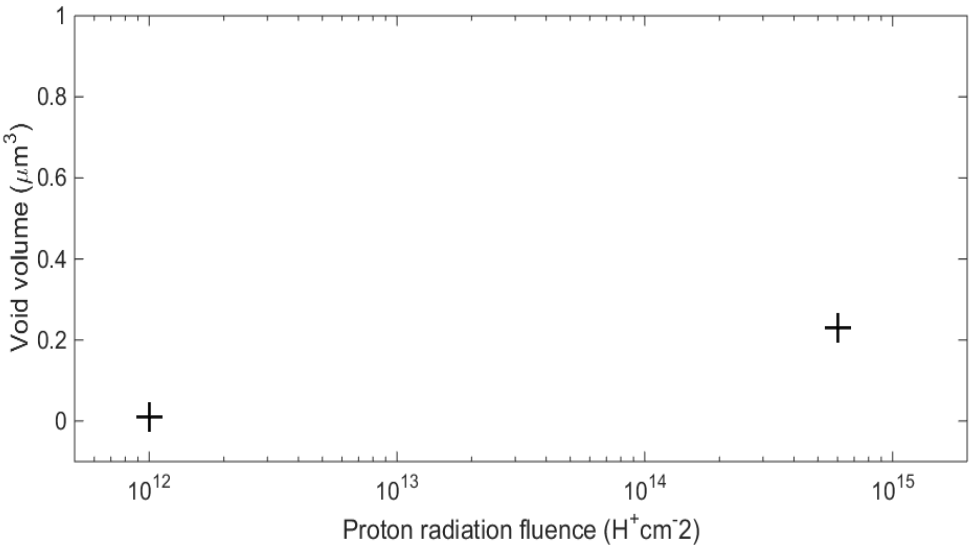

Figure 58. Proton radiation fluence versus void volume.

G. DISLOCATION ANALYSIS

Dislocations are found throughout these heteroepitaxial-grown devices as stated in Chapter II. While the dislocations that occur within the Si / AlN interface are known to be pure edge dislocations (misfit dislocations), the type of connecting threading dislocations found in the epilayers are unknown. Some of these dislocations make it to the interface of the gate and are thought to be detrimental to the performance of the device.

In order to better understand the dislocations within this device, a method called weak-beam dark-field (WBDF) imaging is utilized in the TEM. This method determines the type of dislocation (screw, edge, mixed) present in each region of a TEM sample by obtaining the Burgers vector through imaging at various tilt angles with two beams while adjusting the excitation error. The first step after loading the TEM sample is to test the two-beam contrast with and without aperture in order to obtain an image where contrast from dislocations is present but contrast from strain is removed as seen in Figure 59. The left image displays both contrast of dislocations and strain, while the right image has the dislocation contrast removed from multiple dislocations with pure edge character. At the edge of the sample, contrast re-appears due to sample bending.

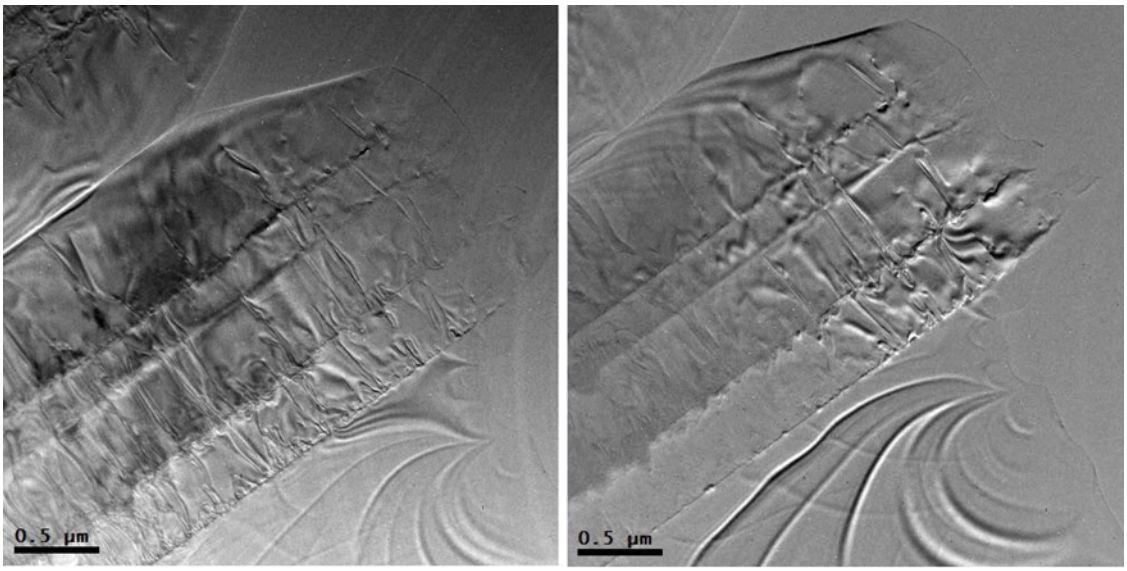

Figure 59. Conventional TEM performed at different tilt angles (excitation), courtesy of P. Specht.

To prepare for a weak beam analysis, first a test was undertaken in the CM300 microscope at NCEM using a cross-sectionally prepared epilayer structure (not a fully processed device). This microscope is equipped for high resolution and did not have the apertures required to completely remove the contrast from dislocations which fulfill the tilt angle g $\underline{x}$ $\underline{b}$ criteria [40]. As seen in Figure 60 on the right, the contrast from the threading dislocations of the various layers disappears even without using a small aperture when the sample is oriented in perfect g/3g excitation, with g = [0002]. Only at the edge of the sample are the dislocations still visible due to sample bending (right, top area in right image of Figure 60). In the left image, the sample was oriented with a dominant g = [0002] excitation and most dislocations are still visible. The CM300 is currently being equipped with a small aperture, and full weak-beam analysis will commence when the microscope is operational again.

Even with the tilting, and lacking the needed small aperture, a remarkable contrast difference is seen in comparative images. Most pronounced, this can be seen in Figure 60 which has the above described g/3g contrast on the left and a perpendicular excitation (g = [1100]) on the right. The dark line on the left side of the figure depicts the strain within the Si_3N_4 strain-compliant layer between the Si substrate and the first AlN buffer layer. Remarkably, some residual dislocations are still visible in the GaN layer, which seem to originate at the last buffer layer interface (noted with arrows). Should those dislocations be visible again in a complete weak-beam analysis of the full device structures, a change in the last buffer layer deposition to eliminate those dislocations is suggested as the next step in device improvement. Those dislocations may be the detrimental culprits. On the right, full dislocation contrast is seen where only pure screw dislocations would be invisible. This portion of the research initiated the identification process of the dislocations that cause issues for the HEMTs and requires much more time for analysis. This method of characterizing dislocation types by region and the knowledge obtained enhances the modeling and future simulations of these defects which ultimately leads to corrective actions in manufacturing to minimize said dislocations.

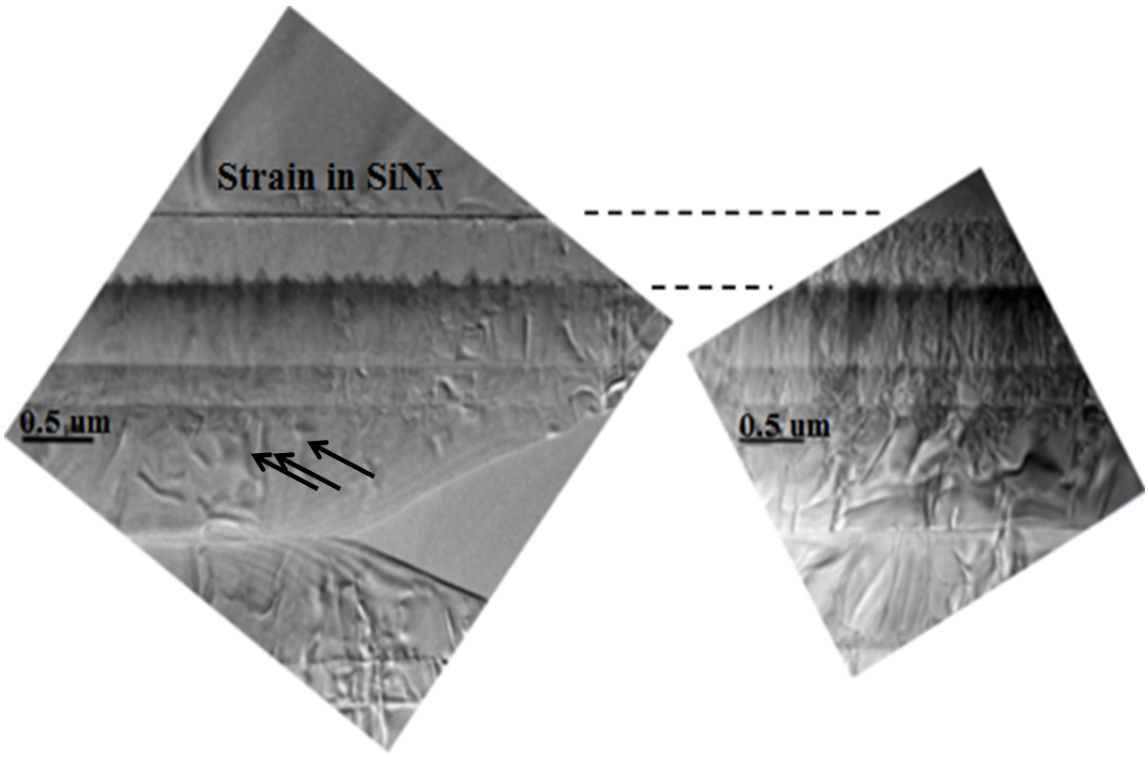

Figure 60. Conventional TEM image of same location at two different tilt angles: left - [0002] excitation / right - [1100] excitation, courtesy of P. Specht.

H. VACANCY AND DIFFUSION MODEL

1. Theory

One theory is that the proton irradiation-induced displacement interactions in the epilayer introduce point defects in the form of vacancies that can be transported via threading dislocations that are already present to cause volume defects such as material voiding at the electrode surface. For an initial estimate, the theory assumes the Frenkel pairs that are introduced by displacement do not recombine. This assumption can then be limited by the speed of transportation for the vacancy to reach the defect region. Furthermore, an upper bound is placed on the volume in which vacancies are pulled. Based on previous work by Was [38], the volume of material containing vacancies that can interact with a threading dislocation, which is used to determine the rate of vacancies pulled in by the threading dislocation, are calculated in this thesis.

2. Model Assumptions

Several assumptions were made in order to simplify this initial model. First, the time in which the material arrives at a steady-state condition after irradiation is insignificant. Second, the recombination of displacement-introduced Frenkel pairs is negligible. All vacancies within a derived volume transport to the defect site for annihilation. Third, the rate at which vacancies are created due to proton irradiation is uniform throughout each material type. Fourth, the diffusion rate coefficient is constant. Fifth, threading dislocations are assumed to be perfect vertical cylinders. Sixth, electric fields do not excite the uncharged vacancies. Seventh, strain fields surrounding the threading dislocation are neglected.

3. Threading-Dislocation Radius of Vacancy Interaction

From assumption five, the threading dislocation's cylindrical volume that pulls in vacancies has a radius R. Relating this radius with a known, uniform dislocation density ρ_d, we see that the volumes of two adjacent dislocations cannot overlap. This limits R to a maximum of [38]

$$\pi R_{\max}^2 \rho_d = 1. \tag{9}$$

Using Equation (9) and a dislocation density of 7.0×10^8 cm^{-2}, we get $R_{\max}$ equal to 0.2132 μm. Assumption six stated that diffusion is the only means of vacancy transport; therefore, the current density of a vacancy is [38]

$$\vec{J}_v = -D_v \vec{\nabla} N_v \tag{10}$$

which is calculated using Fick's law [38], where N_v is the number of vacancies and D_v is the vacancy diffusion coefficient. The concentration of vacancies over time is governed by the continuity equation for vacancies [38]

$$\frac{\partial N_v}{\partial t} = -\nabla \cdot \vec{J}_v + G_0. \tag{11}$$

Substituting (10) into (11) gives

$$\frac{\partial N_v}{\partial t} = \nabla \cdot (\mathrm{D}_v \vec{\nabla} N_v) + G_0 \tag{12}$$

where G_0 is vacancy generation [38]. Equation (12) can be reduced, given the assumptions of steady-state conditions and uniform vacancy diffusion, to

$$D_v \nabla^2 N_v + G_0. \tag{13}$$

Since the volume of interest is cylindrical, that is the coordinate system required. The generation is uniform, and the concentration of vacancies is symmetric [38]. As a result, Equation (13) simplifies to

$$D_v \frac{1}{r} \frac{\partial}{\partial r} \left(r \frac{\partial N_v}{\partial r} \right) + G_0 \tag{14}$$

where r is radial position from the dislocation. Assumption two stated that only vacancies within the cylindrical volume interact; therefore, flux at the edge of the cylinder is zero, resulting in the boundary condition [38]

$$\left. \frac{\partial N_v}{\partial r} \right|_{r=R} = 0 \tag{15}$$

and the vacancies due to displacement at this point are assumed to be [38]

$$N_{vd} = N_v(R_d) \tag{16}$$

where the concentration as it varies radially from the center of the dislocation is [38]

$$N_v(r) = N_{vd} + \frac{G_0 R^2}{2D_v} \left(\ln\left(\frac{r}{R_d} \right) - \frac{1}{2} \left(\frac{r^2 - R_d^2}{R^2} \right) \right). \tag{17}$$

Now the radius limited by diffusion can be calculated using Equation (7) to obtain the K-P value by using a NIEL value of Si and equating it to Equation (17). Known Si values are used for this proof as an example. By using a reasonable value of 5×10^{10} $\mathrm{cm^{-2}\ s^{-1}}$ for the generation rate, 1×10^{-18} $\mathrm{cm^{-2}\ s^{-1}}$ for the diffusion coefficient [38] and a dislocation radius of 0.5 nm, Equation (7) returns a value $R = 10.0\ \mu\mathrm{m}$. Since this is much greater than the maximum radius calculated for GaN on Al_2O_3 [38], we conclude that the vacancy-pull radius of the threading dislocation is not limited by diffusion. The radius of importance can be calculated via dislocation density.

4. Geometric Volume Comparison

Ideally, the TEM is used for analysis to determine actual dislocation density, but this needs to be completed in the future. Since the threading dislocation radius and volume are not limited by diffusion, the next item to compare was the volume of the void in Ni to the volume of the threading dislocation for an estimate of the radius. In order to start, the NIEL curves of each material are needed in order to determine the amount of vacancies created by proton irradiation in each layer of material within the HEMT device. Equations (3) to (7) were utilized in a MATLAB script (see Appendix) that was developed in collaboration with Matthew Porter in order to calculate and plot the NIEL curves for each material as seen in Figure 61, where the NIEL curve for Ni is displayed. This script was confirmed by comparing the previous NIEL curves shown by Messenger using Si values.

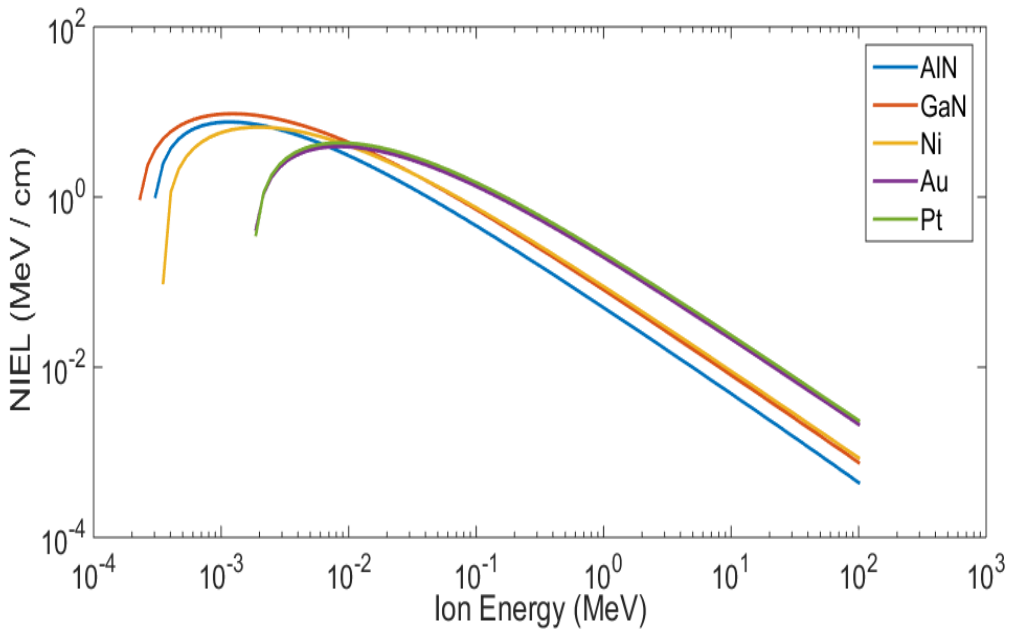

Figure 61. Proton NIEL curves for HEMT materials.

Bragg's rule was utilized when calculating the NIEL curves of compounds in terms of their atomic numbers and masses in a similar weighting fashion to Vegard's law [39]. The concentration of vacancies was found using the Kinchin-Pease formula, Equation

(8). This concentration of vacancies and the known volume of an individual void were used to calculate the radius of vacancy pull of the threading dislocation as depicted in the schematic in Figure 62, assuming that the entire volume fits inside. The radius of this "highway" was compared to STEM images for verification that the result was within reason [25, 26].

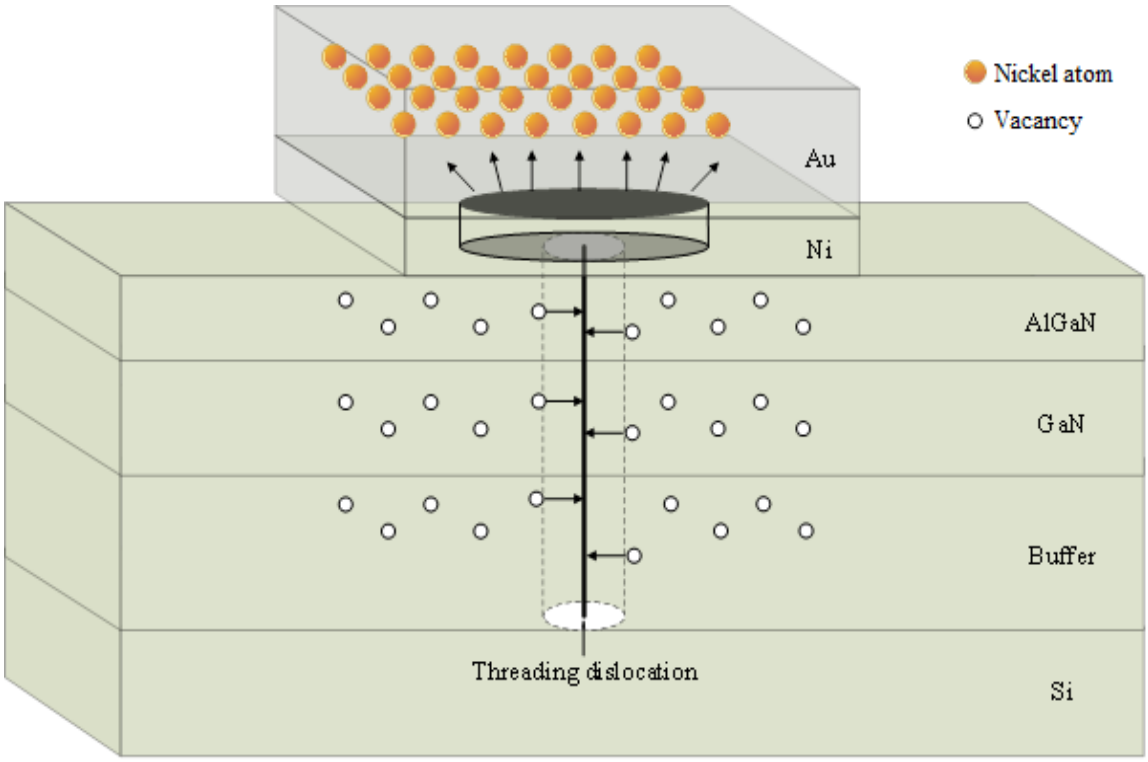

Figure 62. Schematic of a threading dislocation attracting vacancies forming a highway for Ni atom diffusion uniformly into Au layer causing void.

Initial results of these calculations are seen in Table 9, where GaN and AlN were both calculated as a 50/50 compound. The difference in Ni versus Au NIEL values at 2.0 MeV leads to an order of magnitude difference in the number of displacements. This supports the phenomenon that was seen in the Ni diffusion into the Au. Using the largest Ni void area to obtain the void volume, we equated this number to the volume of the threading dislocation in order to solve for the radius. The preliminary calculations return a value of 0.24 μm, which is for the entire length of dislocation, 2017.5 nm from the device structure diagram.

It is important to note that this is not the radius of the threading dislocation itself but is the radius of the effective vacancy pull of the dislocation. Since we have numerous materials, a better approximation is to weight the radius of each material region by using their respective vacancy-current density, which is dependent upon diffusion constants. Overall, this model does make some assumptions and is a good preliminary model of the void creations that can be used to predict void volumes versus radiation dose. An interesting comparison can be seen between the vacancy concentration of Ni, Pt, and Au. The Ni has a much larger difference in vacancies with the Au than the Pt versus Au, which results in less diffusion and voiding.

I. MATERIAL CALCULATIONS FOR DIFFUSION MODEL IMPROVING THE EPILAYER

The epilayer of a sample refers to the contact between a crystalline layer of material applied to the Si substrate. In the case of the first batch of NRL devices, the epilayer was deposited with two different gate metals, Ni/Au and Pt/Au, with all buffer layers being the same. A new and improved epilayer was utilized at NRL to create the sample seen in Figure 63, which includes team recommendations for a device with minimized defects.

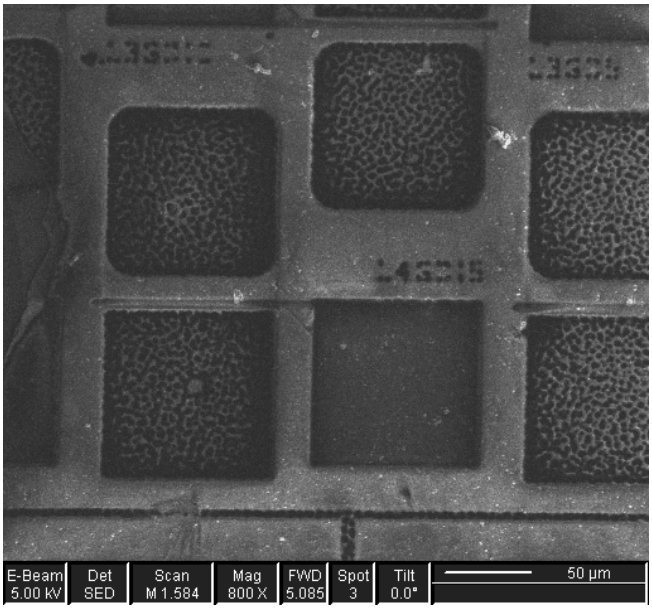

Figure 63. NRL's new epilayer sample.

The main difference in this sample is that a 3.5 nm layer of Si_3N_4 was inserted between the gate and AlGaN barrier layer. These samples also have an increased Si_3N_4 surface layer, and the gate was altered from the previous samples, which is now visually different than the source and drain regions. The next step was to strip the new devices for analysis. Preliminary STEM and EDS tests currently being conducted at LBNL demonstrate that edge voiding in fresh devices is not prevented with this new epilayer construction. A larger sample size is required for further analysis, and arrangements for process modifications are in work.

J. SUMMARY OF DEFECTS IDENTIFIED, CAUSES, SOLUTIONS

Many types of defects were found within the various types of HEMT devices analyzed in this thesis. Their potential causes and recommended solutions are listed in Table 10 for quick reference. Currently, the 3.5 nm Si_3N_4 layer underneath the gate electrode is being investigated.

Table 9. Summary of Defects

Defect	Theoretical Cause	Recommended Solution	Material/Region Affected
Edge (before)	Manufacturing (diffusion, sequence)	Si_3N_4 PECVD before gate deposition process	Ni
Edge (after)	Diffusion	Unknown	Ni and Pt
Buffer boundary	Manufacturing	Post gate annealing	Ni
Clustering (length)	Diffusion or manufacturing	Unknown	Ni
String (width)	Manufacturing, material defect	Monitor for reoccurrence	Pt
Circular	Diffusion	Epilayer with thin Si_3N_4 under electrode	Ni and Pt

V. CONCLUSIONS AND FUTURE WORK

A. CONCLUSIONS

The main objective of this thesis was to identify, characterize, and understand the origin of a particular defect found in GaN HEMTs. The research found Ni and Pt voids in the gate finger underneath the Si_3N_4 and Au layers after proton irradiation, which resulted in a decrease in effective gate area for capacitance. For this purpose, a novel FIB-based stripping technique was developed which allows investigating the Ni and Pt gate layers after removing the top passivation and Au layers. It was proposed that the defects emerge due to sites with large numbers of vacancies, which leads to the Kirkendall effect where Ni or Pt (to a lesser extent) interdiffuses with Au to produce a void. This process requires a sufficiently large number of vacancies present and Ni or Pt diffusing significantly faster than Au.

The type of voiding occurred in multiple forms: edge voiding, which was present on all proton irradiated samples, and circular voiding and clustering across the finger length, which occurred in approximately 30 percent of the samples. The voiding also predominantly occurred near the root of the gate. While the decrease in gate area affects the gate current, it is not the only cause of degradation, as seen in Anderson's work where trapping issues in the structure were suggested to affect the I-V performance [41]. There was also a degradation found in the AlGaN/GaN interface after proton irradiation, where an aluminum oxide amorphous layer formed. This significantly changes the interface of the Ni and AlGaN and contributes to the observed changes in gate current.

The secondary objective was to propose potential remedies in order to minimize, and in the best case eliminate, the defects in order to increase the reliability of these devices. A thin layer of Si_3N_4 underneath the gate was suggested to allow electron tunneling through the Si_3N_4, yet prevent vacancy or metal transport via dislocations. Another recommendation is to alloy the Au with its respective gate electrode material in order to reduce the vacancies available. NRL took the first recommendation into consideration and manufactured new devices that were also proton irradiated. The first

sample has shown no edge voiding in STEM analysis, which is promising. A detailed analysis is in progress. NRL also plans on implementing the alloyed gate device in future experiments.

An additional goal that arose during the conduct of this thesis research was to model the voiding caused by proton irradiation. An initial model was developed that relates the volume of the void to the effective surrounding volume of vacancy interaction for a singular-threading dislocation. Knowledge of this volume was used to calculate the rate of vacancy intake by a dislocation. NIEL curves were also calculated for the materials utilized in the GaN HEMT device, which resulted in a graph of proton-radiation fluence versus void volume that could be used to verify our theories of diffusion and voiding in future work. The results are also useful in comparing other types of radiation, such as neutron or heavy ion radiation, by using their known NIEL values to predict defects.

B. FUTURE WORK

Use the data obtained on the old epilayer NRL samples for both Ni/Au and Pt/Au gated HEMTs, to determine which type of dislocations are detrimental to the device in promoting the Kirkendall effect. This information can be given to the epilayer growth company to avoid this type of dislocation.

The new NRL samples have the additional Si_3N_4 layer underneath the gate, which completely insulates the sample and causes ionization effects. A new procedure should be developed for these samples that could then also be applied to other insulating samples. This technique promises to provide a new level of "easy reverse engineering" of devices performed directly in the FIB.

Since the new samples were pulled after each radiation fluence, it would be useful to compare the size of the voids with increasing proton irradiation in order to better understand and describe the Kirkendall effect which is causing the voids. These new void calculations can be compared to the prediction model so that it can be revised.

Due to the fact that C-V measurements only characterize interfaces, it is necessary to implement deep-level transient spectroscopy (DLTS) in order to accurately give an electrical characterization of trap states, parameters, and concentrations within the devices. This characterization, which already exists and applies to deep-level defects, is useful for expansion upon the model used in this thesis in order to more accurately correlate degradation of electrical performance to its defect source.

Lastly, it is be useful to obtain void formation data in voltage-stressed material to characterize the electric-field effect on the voids. Very few, still unpublished comments from other international research groups suggest that such voids can be formed after pronounced operation of such HEMTs. To date, no systematic investigation exists in this research area. A comparison of effects seen due to an increase in temperature in-situ TEM experiments versus the increase in proton would be beneficial to further the understanding of void formation in gates of GaN HEMTs. All of the above experiments should result in an additional process adjustment to improve future HEMT performance.

THIS PAGE INTENTIONALLY LEFT BLANK

APPENDIX. MATLAB CODE

```
%%Test of NIEL function to plot Au NIEL curve on Si
%%M.A. Porter & M.G. Wade

%AlN_NIEL
Na = 6.02e23;

Td = 50e-3; %%Threshold displacement energies in KeV

Z1 = 1; %%Atomic number of H ion
%Z2 = 31; %%Atomic number of target
Z2 = (.5*13 + .5*7)
%Ztar = [28,79,78,31,7,13];
%[Ni, Au, Pt, Ga, N, Al]

M1 = 1.007; %%Molar mass of H ion
%M2 = 69.732; %%Molar mass of target
M2 = (.5*26.982 + .5*14.007)
%Mtar = [58.693,196.97,195.08,69.732,14.007,26.982];

rhotar = 3.26; %%Density of target
%rhotar = [5.9,19.3,21.5,5.91,1.25,2.7];

Ntar = (rhotar*Na)/M2
%use for element
%Ntar = (Na)/M2
%use for compound
E0 = logspace(-1,5,1e2);
%outputcollate = [];
output = [];
%
%for j=1:length(Ztar)
 % Z2 = Ztar(j);
 % M2 = Mtar(j);
 % rhotar2 = rhotar(j);
 % output = [];
 for i=1:length(E0)
 testval = NIEL('Nastasi',E0(i),Z1,Z2,M1,M2,Ntar,Td)
 output = [output testval];
 end
 %outputcollate = [outputcollate; output];
%end
%
loglog(E0./1e3,output./1e3) %%Plot NIEL curve as MeV/cm vs MeV
axis([1e-4 1e3 1e-5 1e3]);
ylabel('NIEL (MeV*cm^2/g)');
xlabel('Ion Energy (MeV)')
hold on
```

```
%GaN_NIEL

Na = 6.02e23;

Td = 19.4e-3; %%Threshold displacement energies in KeV

Z1 = 1; %%Atomic number of H ion
%Z2 = 31; %%Atomic number of target
Z2 = (.5*31 + .5*7) %GaN
%Ztar = [28,79,78,31,7,13];
%[Ni, Au, Pt, Ga, N, Al]

M1 = 1.007; %%Molar mass of H ion
%M2 = 69.732; %%Molar mass of target
M2 = (.5*69.732 + .5*14.007)
%Mtar = [58.693,196.97,195.08,69.732,14.007,26.982];

rhotar = 5.91; %%Density of target
%rhotar = [5.9,19.3,21.5,5.91,1.25,2.7];

Ntar = (rhotar*Na)/M2

E0 = logspace(-1,5,1e2);

output = [];

 for i=1:length(E0)
 testval = NIEL('Nastasi',E0(i),Z1,Z2,M1,M2,Ntar,Td)
 output = [output testval];
 end

loglog(E0./1e3,output./1e3) %%Plot NIEL curve as MeV/cm vs MeV
axis([1e-4 1e3 1e-5 1e3]);
ylabel('NIEL (MeV*cm^2/g)');
xlabel('Ion Energy (MeV)')
hold on

%Ni_NIEL

Na = 6.02e23;

Td = 23e-3; %%Threshold displacement energies in KeV

Z1 = 1; %%Atomic number of H ion
Z2 = 28; %%Atomic number of target

M1 = 1.007; %%Molar mass of H ion
M2 = 58.693; %%Molar mass of target

rhotar = 5.9; %%Density of target

Ntar = (rhotar*Na)/M2
```

```
E0 = logspace(-1,5,1e2);

output = [];

 for i=1:length(E0)
 testval = NIEL('Nastasi',E0(i),Z1,Z2,M1,M2,Ntar,Td)
 output = [output testval];
 end

loglog(E0./1e3,output./1e3) %%Plot NIEL curve as MeV/cm vs MeV
axis([1e-4 1e3 1e-5 1e3]);
ylabel('NIEL (MeV*cm^2/g)');
xlabel('Ion Energy (MeV)')
hold on

%Au_NIEL

Na = 6.02e23;

Td = 35e-3; %%Threshold displacement energies in KeV

Z1 = 1; %%Atomic number of H ion
Z2 = 79; %%Atomic number of target

M1 = 1.007; %%Molar mass of H ion
M2 = 196.97; %%Molar mass of target

rhotar = 19.3; %%Density of target

Ntar = (rhotar*Na)/M2

E0 = logspace(-1,5,1e2);

output = [];

 for i=1:length(E0)
 testval = NIEL('Nastasi',E0(i),Z1,Z2,M1,M2,Ntar,Td)
 output = [output testval];
 end

loglog(E0./1e3,output./1e3) %%Plot NIEL curve as MeV/cm vs MeV
axis([1e-4 1e3 1e-5 1e3]);
ylabel('NIEL (MeV*cm^2/g)');
xlabel('Ion Energy (MeV)')
hold on

%Pt_NIEL

Na = 6.02e23;

Td = 36e-3; %%Threshold displacement energies in KeV
```

```
Z1 = 1; %%Atomic number of H ion
Z2 = 78; %%Atomic number of target

M1 = 1.007; %%Molar mass of H ion
M2 = 195.08; %%Molar mass of target

rhotar = 21.5; %%Density of target

Ntar = (rhotar*Na)/M2

E0 = logspace(-1,5,1e2);

output = [];

 for i=1:length(E0)
 testval = NIEL('Nastasi',E0(i),Z1,Z2,M1,M2,Ntar,Td)
 output = [output testval];
 end

loglog(E0./1e3,output./1e3) %%Plot NIEL curve as MeV/cm vs MeV
axis([1e-4 1e3 1e-5 1e3]);
ylabel('NIEL (MeV*cm^2/g)');
xlabel('Ion Energy (MeV)')


function E = NIEL(funcsel,E0,Z1,Z2,M1,M2,N,Td)
%E = NIEL NIEL calculation function
%Calculates NIEL in keVcm^2/g utilizing either Natasi
%Input variables:
% funcsel - Selects 'Nastasi' approx. Other vals throws error.
% E0 - ion incident energy in keV
% Z1 - ion atomic number
% Z2 - target atomic number
% M1 - ion atomic mass
% M2 - target nuclear mass
% N - target number of atoms per cm^3 of material
% Ts - displacement threshold energy
 a0 = 0.5292e-8;

 nint = 1e7;

 Tmax = (4*M1*M2*E0)/(M1+M2)^2;
 eps = (32.53.*M2.*E0)./(Z1.*Z2.*(M1+M2).*(Z1.^0.23+Z2.^0.23));
 %eps = eps./1000
 au = (0.8854.*a0)./(Z1.^0.23+Z2.^0.23);

 k = -pi*au.^2/2;

 T = linspace(Td,Tmax,nint);
 tlitt = (T.*eps.^2)./Tmax;

 trootmax = eps
```

```
 trootmin = eps*sqrt(Td./Tmax)

 trootint = (trootmax-trootmin)./nint

 if(funcsel == 'Nastasi')
 f = nastasi(tlitt);
 L = lindhard(T,Z2,M2);
 inte = sum(f.*L.*trootint);
 E = -1*(k*N*Tmax.*inte)./(eps.^2);

 else
 disp('Please enter valid function name!');
 return;
 end
end


function f=nastasi(t)
%%Nastasi approx function calculation
 lambda = 5.012;
 m=0.203;
 q=0.413;

 pre = lambda.*t.^(0.5-m);
 brack = 1 + (2*lambda.*t.^(1-m)).^q;

 f = pre.*brack.^(-1/q);
end


function L = lindhard(T,Z2,M2)
%%Lindhard function calculation
 kd = (0.1334.*Z2.^(2/3))./sqrt(M2);
 epsd = 0.01014.*T.*(Z2).^(-7/3);

 g = epsd + 0.40244.*(epsd).^(3/4) + 3.4008.*(epsd).^(1/6);

 L = 1./(1+kd.*g);
end
```

THIS PAGE INTENTIONALLY LEFT BLANK

LIST OF REFERENCES

[1] S. Lee, R. Vetury, J. Brown, S. Gibb, W. Cai, S. Jinming D. Green, and J. Shealy, "Reliability assessment of AlGaN/GaN HEMT technology on SiC for 48V applications," in *46th Annual International Reliability Physics Symposium,* Phoenix, AZ, 2008, pp. 446–449.

[2] C. Xie and A. Pavio, "Development of GaN HEMT based high-power high efficiency distributed power amplifier for military applications," in *Proc. IEEE Military Communications Conference,* Orlando, FL , 2007, pp. 1–4.

[3] K. Kikuchi, M. Nishihara, H. Yamamoto, T. Yamamoto, S. Mizuno, F. Yamaki, and S. Sano, "An 8.5–10.0 GHz 310 W GaN HEMT for radar applications," in *Proc. IEEE International Microwave Symposium*, Tampa Bay, FL, 2014, pp. 1–4.

[4] T. J. Anderson and A. Koehler, "Reliability of GaN HEMTs: electrical and radiation induced failure mechanisms," in *Meeting of the Electrochemical Society Conf.*, San Francisco, CA, 2013, pp. 221–225.

[5] A. Wessel, "Imaging gallium nitride high electron mobility transistors to identify point defects," M.S. thesis, Dept. Elect. Eng., Naval Postgraduate School, Monterey, CA, 2014.

[6] P. Whiting, N. Rudawski, M. Holzworth, S. Pearton, K. Jones, L. Liu, T. Kang, and F. Ren, "Under-gate defect formation in Ni-gate AlGaN/GaN high electron mobility transistors," Microelectronics Reliability, vol. 52, no. 11, pp. 2542–2546, Nov. 2012.

[7] Z. Zhang, P. Kumar, E. Zhang, D. Fleetwood, R. Schrimpf, P. Saunier, C. Lee, S. Ringel, and A. Arehart, "Proton irradiation-induced traps causing threshold voltage instabilities and RF degradation in AlGaN/GaN HEMTs" in *Proc. IEEE International Reliability Physics Symposium,* Monterey, CA, 2015.

[8] S. Vitanov, "Simulation of high electron mobility transistors," Ph.D. dissertation, Dept. Elect. Eng., Univ. of Vienna, Austria, 2010. [Online]. Available FTP: http://www.iue.tuwien.ac.at/phd/vitanov/node65.html

[9] S. Adachi, *Properties of Semiconductor Alloys: Group-IV, III-V and II-VI Semiconductors*. [Online]. Available FTP: http://www.wiley.com/WileyCDA/WileyTitle/productCd-0470743697.html

[10] E. Yu, X. Dang, P. Asbeck, S. Lau, and G. Sullivan., "Spontaneous and piezoelectric polarization effects in III–V nitride heterostructures" in *Journal Vacuum Science & Technology*, vol. 17, no. 4, pp. 1742–1749, July, 1999.

[11] L. Vegard, “The constitution of the mixed crystals and the room filling the atoms,” *Journal of Physics*, vol. 5, no. 1, pp. 17–25, Dec. 1921.

[12] P. Javorkaa, A. Alama, M. Marsoa, M. Woltera, A. Foxa, M. Heukena and P. Kordoša, “Material and device issues of AlGaN/GaN HEMTs on silicon substrates,” in *MRS Proceedings,* 2002, p. L9. 1.

[13] R. S. Pengelly, S. M. Wood, J. W. Milligan, S. T. Sheppard, and W. L. Pribble, “A review of GaN on SiC high electron-mobility power transistors and MMICs,” *Microwave Theory and Techniques, IEEE Transactions on,* vol. 60, pp. 1764–1783, 2012.

[14] U. Mishra and J. Singh, *Semiconductor Device Physics and Design,* Dordrecht, Netherlands: Springer Science & Business Media, 2007.

[15] R. Lieten, S. Degroote, “Deposition of Group iii-nitrides on Ge,” U.S. Patent WO2008011979A1, Jan. 31, 2008.

[16] S. Mathis, A. Romanov, L. Chen, G. Beltz, W. Pompe, and J. Speck, “Modeling of threading dislocation reduction in growing GaN layers,” *Journal of Crystal Growth,* vol. 231, no.3, pp. 371–390, Oct. 2001.

[17] T. Liu, “Transmission electron microscopy studies of GaN/γ-LiAlO heterostructures,” PhD. in Physics, Dept. Math. And Nat. Sci., Humboldt University of Berlin, Germany, 1974.

[18] P. Specht, Independent Lecture Series, Topic: “Electron Microscopy of GaN HEMTs,” Lawrence Berkeley National Laboratory, Berkeley, California, July 2014–July 2015.

[19] C. Schuh. Physical Metallurgy. Class Lecture, Topic: “Burgers’ vector,” MIT Opencourseware, 2009. [Online]. Available FTP: http://ocw.mit.edu/courses/materials-science-and-engineering/3-40j-physical-metallurgy-fall-2009/lecture-notes/MIT3_40JF09_lec03.pdf

[20] O. Ambacher, J. Smart, J. Shealy, N. Weimann, K. Chu, M. Murphy, W. Schaff, L. Eastman, R. Dimitrov, L. Wittmer, M. Stutzmann, W. Rieger, and J. Hilsenbeck, “Two-dimensional electron gases induced by spontaneous and piezoelectric polarization charges in N- and Ga-face AlGaN/GaN heterostructures,” *Journal of Applied Physics*, vol. 85, no. 6, pp. 3222–3233, Mar. 1999.

[21] V. Siklitsky. (2015). *Semiconductors on NSM*. [Online]. Available FTP: http://www.ioffe.ru/SVA/NSM/Semicond/index.html

[22] G. Simin. ELCT 871: Advances in semiconductor devices. Class Lecture, Topic: "High Electron Mobility Transistors (HEMTs)." University of South Carolina, 2006. [Online]. Available FTP: http://www.ee.sc.edu/personal/faculty/simin/ELCT871/18%20AlGAN-GaN%20HEMTs.pdf

[23] X. Hu, A. Karmarkar, B. Jun, D. M. Fleetwood, R. Schrimpf, R. Geil, R. Weller, B. White, M. Bataiev, L. Brillson, and U. Mishra, "Proton-irradiation effects on AlGaN/AlN/GaN high electron mobility transistors," *Nuclear Science, IEEE Transactions on,* vol. 50, no. 6, pp. 1791–1796, Dec. 2003.

[24] J. Ziegler and J. Biersack, *The Stopping and Range of Ions in Matter*. New York: Springer, 1985.

[25] S. Messenger , E. Burke, M. Xapsos, G. Summers, R. Walters, I. Jun, and T. Jordan, "NIEL for heavy ions: an analytical approach," *Trans. Nuclear Science, IEEE,* vol. 50, no.6, pp. 1919–1923, Dec. 2003.

[26] M. Nastasi, J. Mayer, J. Hirvonen, *Ion-Solid Interactions: fundamentals and Applications*. New York: Cambridge Univ. Press, 1996.

[27] A. Koehler, P. Specht, T. Anderson, B. Weaver, J. Greenlee, M. Tadjer, M. Porter, M. Wade, O. Dubon, K. Hobart, T. Weatherford, and F. Kub, "Proton Radiation-Induced Void Formation in Ni/Au-Gated AlGaN/GaN HEMTs," *Electron Device Letters*, *IEEE*, vol. 35, no. 12, pp. 1194–1196, Dec. 2014.

[28] P. Specht, "Finding point defect in nitride-based device structures using TEM imaging techniques" in CS MANTECH Conference, Denver, Colorado, May 19th–22nd, 2014.

[29] D. Williams and C. Carter, *The Transmission Electron Microscope,* 2nd ed. New York: Springer, 1996.

[30] P. Trimby. (n.d.). *Imaging and analysis techniques in materials science*. [Online]. Available FTP: http://materialsknowledge.org/docs/pat1.pdf

[31] J. Schweitzer. (n.d.) *Scanning electron microscope*. [Online]. Available FTP: https://www.purdue.edu/ehps/rem/rs/sem.htm

[32] K. Briggman and D. Bock, "Volume electron microscopy for neuronal circuit reconstruction." *Current Opinion in Neurobiology*, vol. 22, no. 1, pp. 154–161, Feb. 2012.

[33] R. J. Ross, "45. Transmission electron microscopy for failure analysis of semiconductor devices," in *Microelectronics Failure Analysis Desk Reference (6th Edition)* ASM International, 2011.

[34] R. J. Ross, “48. Energy dispersive X-ray analysis,” in *Microelectronics Failure Analysis Desk Reference (6th Edition)* ASM International, 2011.

[35] J. Sarkar, *Sputtering Materials for VLSI and Thin Film Devices*. Waltham, Massachusetts: William Andrew, 2010.

[36] K. Butcher, “Migration and plasma enhanced chemical vapor deposition,” U.S. Patent US9045824, 2015.

[37] W. Xin-Hua, Z. Miao, L. Xin-Yu, P. Yan, Z. Ying-Kui and W. Ke, “The physical process analysis of the capacitance—voltage characteristics of AlGaN/AlN/GaN high electron mobility transistors,” Chinese Physics B, vol. 19, pp. 097302-1 – 097302-7, 2010.

[38] G. Was, *Fundamentals of Radiation Materials Science: Metals and Alloys*, Springer-Verlag, Berlin-Heidelberg, 2007.

[39] W. H. Bragg and W. L. Bragg. “The reflection of X-rays by crystals,” in *Proceedings of the Royal Society of London. Series A, Containing Papers of a Mathematical and Physical Character,* April 1913, vol. 88, no. 605, pp. 428–438.

[40] J. Kioseoglou, G. Dimitrakopulos, Ph. Komninou, H. Polatoglou, and Th. Karakostas, *Partial dislocations in wurtzite GaN*. [Online]. Available: http://www.psi-k.org/newsletters/News_64/Highlight_64.pdf

[41] T. Anderson, A. Koehler, J. Greenlee, B. Weaver, M. Mastro, J. Hite, C. Eddy, F. Kub, and K. Hobart, “Substrate-dependent effects on the response of AlGaN/GaN HEMTs to 2-MeV proton irradiation,” *Electron Device Letters, IEEE*, vol. 35, no. 8, pp. 826–828, Aug. 2014.

INITIAL DISTRIBUTION LIST

1. Defense Technical Information Center
   Ft. Belvoir, Virginia

2. Dudley Knox Library
   Naval Postgraduate School
   Monterey, California